Imperial College London

Advances in Chiral Lasers and Transformation Theory

Author:

René David Martin Topf

Supervisor:

Prof. Martin W. McCall

Imperial College London

Department of Physics

Thesis submitted in partial fulfilment of the requirements for the degree of Doctor of Philosophy and Diploma of Imperial College London.

9th April 2017

Abstract

The first part of the presented thesis begins by developing the lasing mode theory of a structurally chiral laser and highlighting the possibilities for a structurally chiral laser to lase both left and right circularly polarised light, as well as within the photonic bandgap. The discoveries are utilised in order to develop the lasing mode theory of a chiral distributed Bragg reflector laser, which consists of structurally chiral mirrors and a uniform lasing cavity, as well as of a hybrid chiral laser, which consists of structurally chiral mirrors with a contrahanded structurally chiral lasing cavity. Applications towards more efficient 3D projectors as well as 3D displays are discussed.

The second part of the thesis develops the theory of transformation optics from first principles using differential geometry. The rigorously constructed structure is manipulated in order to examine the effects of a transformation on the refractive index. The analysis reveals the existence of a refractive index ellipsoid, which encodes the complete transformation and can be used to intuitively grasp the effects of any given transformation on light rays travelling inside the transformation optics device. The refractive index ellipse is calculated for the well known cylindrical cloak as well as for a new type of twist deformation, providing insights into the inner workings of these devices.

Dedication

In light of recent events I am fiercely reminded that there are four people in my life that have taken care of me, selflessly and with a level of devotion that leaves me feeling blessed. Their support came so fully and naturally that I took it for granted, as another wonder in my life. I am deeply grateful for their love, guidance and support. It has shaped me into the man I am today and will continue to guide me throughout my life.

Saba Shimon I remember from my childhood as a force of happiness and joy that made it a pleasure to come visit Israel. Apa was such a good man, who's decency, morality and compassion I strive to emulate and who's absence is still strongly felt. Ama Ati passed away days ago. We shared a special bond and her unwavering love made me the optimist I am today. Finally, Safta Raya:

תודה לך על כל העזרה וכל מה שנתת לי במהלך השנים. את שומרת ודואגת לנו, אוהב אותך.

Acknowledgments

The characters herein, whenever listed consecutively, are presented in the order in which they appeared in the author's life in order to avoid confusion and anger vis-à-vis positioning with regards to other friends.

Who to thank? Well... As always, first there's Vali, who has supported me throughout the PhD and has helped me through everything that life threw my way. Without you I would be a lot more alone. Romi and Dani, not so much for helping with the PhD, but for being the most wonderful sisters I could hope for and loving me the way I am, craziness and all. And for naturally turning home into a place I want to come back to again and again. Mom, for showing me how to be conscious, conscientious and caring and helping me learn from and accept my experiences, be they happy or sad. Dad, for a job? ... Also, but for fearlessly living a life according to his morals. Open and honest and always trying as hard as he can to do what he thinks is right. It allows me to compare and contrast his view on life to mine and forces me to find out who I am and try to live by it. The rest of my family, in Israel and in Germany for their love, which is always there and always strong. And Janina in particular for her year in London and Reading with me, one of the best of my life.

We've covered family, so we switch to... Yuval, Niv, Maxi, Christian, Felix, Eric. Still family, but one I got to choose! Horrible choices the lot, but what can you do? To misquote Bilbo from The Fellowship of the Ring, mostly because these are my acknowledgements and no one can stop me: I know all of you better than any sane man should like, and I like more than half of you better than you deserve! Wherever life takes us, we remain together.

Now to my closest friends in London, in two parts. First, the ones who helped me with the PhD are Noemi, Ian, Freddy, Sam, Moritz, Jack, Javier. The things we've been through and the places we've seen... And the endless lunches, coffees, drinks in and around Uni, which broke the monotony of banging my head against the wall until an idea fell out.

Next, the others, who made my life so enjoyable and have always had my back (but crucially did not support my PhD and are therefore listed after the ones who did. This is a thesis after all!). Alexa, Paolo, Ahmed, Meg, Tessa, Aisling, Siba, without you it would have been a dreary experience, not one worth having. Some of you have been with me since my sister met you, others have been more recent additions, but all of you are in my heart and will be visited and forced to visit me. I assume this is clear.

Finally, I would like to thank Martin. You took me in as a young mathematician and let me convince you I could learn the required physics to pass a viva. Let us hope I was right. Thank you for your support over the past years. I really enjoyed our work together, our work styles fit each other excellently. You let me run with my ideas and gently guided them. Then, when I got stuck you spent a frankly insultingly short amount of time solving whatever problems I arrived with or providing "brilliant insights" (your words) that opened new directions to explore and added whole sections to already written manuscripts. In exchange, I tried to help where help was needed, working on whatever problems you were working on and sometimes even coming back having "cracked the problem, very good" (again, your words). I had a fun time of it, keep me updated with the future of chiral lasers as well as transformation theory. I am very interested to see where you take the research next!

Contents

List of Figures

Chapter 1

Overview of the Thesis

1.1 Structure of Thesis

The thesis presented here for consideration consists of an introductory section contained in Chapter 1 and two semi-autonomous parts. Part I presents advances made towards understanding the lasing mode structure of three types of chiral lasers, the structurally chiral laser, the chiral distributed Bragg reflector laser and the hybrid chiral laser. Part II showcases advances made in transformation optics, where the theory behind the refractive index ellipsoid is developed, a construction that uniquely defines any transformation optics device. The refractive index ellipsoid is then developed for two transformation optics devices in order to demonstrate its use.

This rather unusual structure suggests itself due to the organic nature in which the research conducted during the past years has developed. Initially, the research focus was set towards the development of transformation optics in line with Professor McCall's research. However, the author worked alongside McCall in most of his research branches.

In transformation optics the work concentrated on a number of smaller research projects, most of which served to help understand exactly how transformation optics works and try to develop ways in which to apply the abstract methodology to other fields of research. Once a strong foundation in the fundamentals of transformation optics was established

research on the refractive index ellipsoid and its applications began in earnest. The results of the research into the fundamentals of transformation optics as well as the refractive index ellipsoid are presented in Part II.

The most promising branch not connected to transformation optics began with a simple statement made in McCall's 2009 paper on structurally chiral media [2], where a variable D is highlighted as a potential lasing condition for a structurally chiral laser and McCall promises to pursue it in further research. This research fell to the author and developed into Part I of the thesis.

The research objectives developed naturally and often alongside each other. There were constant connections made between the two research paths, so that during the PhD a single research objective was followed. Some of the crossover points include Möbius transformations, the Oseen method and the twisted medium developed using the refractive index ellipsoid discussed in Part II. In fact, the twisted medium was developed precisely because of the group's interest in finding a structurally chiral medium using transformation optics. The split in the thesis is therefore artificial, induced for clarity's sake with the hope that any reader will enjoy both sections independently and see the connections between the sections where they occur.

1.2 Overview of Structurally Chiral Lasers

The most common type of structurally chiral lasers are cholesteric liquid crystal lasers, which were patented by Goldberg and Shnur in 1973 [5], theoretically analysed by Kukhtarev in 1978 [6] and built by Il'chishin et al. in 1980 [7]. Chiral refers to a geometric property of the active medium of the laser, which can not be superimposed onto a mirror image of itself. Chiral molecules and objects are abundant and chirality often has a significant effect. One notorious example is Thalidomide, a drug which was prescribed against morning sickness. Tragically, the active ingredient was chiral and while one handedness was safe, the opposite handedness led to deformities in the children being born, with 2,000 deaths and 10,000 serious birth defects attributed to the drug [8]. In chiral lasers the chirality

ensures that right circular polarisation is effected differently by the structure than left circular polarisation. The chirality in cholesteric liquid crystals occurs because cholesteric liquid crystals consist of individual liquid crystal molecules aligned in layers, with each layer rotated with respect to the previous layers. In this way a rotation is introduced into the macroscopic structure and the liquid crystal structure becomes chiral. Kukhtarev's work was preceded by Kogelnik and Shank's 1972 publication, which presented a scalar coupled wave theory analysis of distributed feedback lasers.

Structurally chiral lasers use the distributed feedback of cholesteric liquid crystals to generate a photonic bandgap and then use the diverging density of photon states at the band-edge to induce long photon-dwell times and lase. The distributed feedback is polarisation specific, so that a right-handed cholesteric liquid crystal structure distributively reflects right circular polarisation without affecting left circular polarisation.

In 1994 Dowling et al. realised that due to the diverging density of photon states previously discovered, cholesteric liquid crystal lasers a few micrometers in length could be induced to lase at low gain thresholds [9]. Low threshold lasing using the band-edge mode was first demonstrated by Kopp et al. in 1998 [10].

Since then cholesteric liquid crystal lasers have become an active area of research. Lasing in different liquid crystal phases has been demonstrated [11] and in a number of different materials, including polymers [12] and glass [13]. Dynamic laser tuning has been demonstrated using a number of different methods including tuning throughout the visible spectrum and into the ultraviolet [14].

In addition to band-edge lasers considerable research has gone into defect-lasing, where a defect in the periodic structure is introduced, which creates a lasing mode inside the photonic bandgap. Defect-mode lasers can have lower gain thresholds and narrower spectral bandwidths. Defect modes through the insertion of an isotropic layer between the cholesteric liquid crystals were first studied by Yang et al. in 1999 [15] and twist defects by Kopp and Genack in 2002 [16]. Defect-mode lasers were first experimentally realised by Schmidtke et al. in 2003 [17].

In the recent past there have been two particularly active groups, one led by Coles in

Oxford University, who has since retired and another led by Muševič in the Jožef Stefan Institute. Coles' group published a paper on polychromatic laser arrays in 2008 with the aim of paving the way for laser projection displays [18]. They built a 10x10 lenslet array that can be optically excited by a single wavelength and lases red, green and blue laser pixels. More recently in 2011, Coles' group showed that it is possible to paint red, green and blue liquid crystal layers onto any number of substrates, including flexible plastic films, paper and glass and have demonstrated multi-phase holograms produced with this method [19]. Muševič's group demonstrated how liquid crystal laser droplets self assemble into omnidirectionally emitting microlasers in 2010 [20]. In 2013 they showed self-assembling liquid crystal microtubes that can be used to guide whispering gallery lasing modes and suggest the intriguing possibility of soft photonic circuits [21]. These two spotlights help demonstrate that the field of cholesteric liquid crystal lasers is a vibrant and innovative one. The hope is that the research presented in Part I will help move the field forwards towards new inventions and real-world applications.

In Part I we analyse a cholesteric distributed Bragg reflector laser and a hybrid chiral laser alongside the structurally chiral laser. Both lasers represent subcategories of structurally chiral lasers and are most easily realised using cholesteric liquid crystals. Stockley et al. built a cholesteric distributed Bragg reflector laser in 1999 [22] and Song et al. built a hybrid chiral laser in 2006 [23]. The theory for a passive, scalar, distributed Bragg reflector was analysed by Legoubin in 1995 [24]. As far as we are aware there is no theoretical analysis of the cholesteric distributed Bragg reflector laser or of the hybrid chiral laser or indeed of the structurally chiral laser.

Perhaps the most pressing objective in experimental cholesteric liquid crystal research is replacing the current pulse pumping by continuous electrical pumping in order to allow cholesteric liquid crystal lasers to become commercially viable. Once achieved, cholesteric liquid crystals would be small, tunable and cheap and their applications could be numerous. Immediately apparent are uses in medical applications and spectroscopy, where such lasers could replace more bulky set-ups consisting of numerous lasers simply due to their tunability [25].

Perhaps the most exciting and potentially lucrative use would be in display technologies.

Cholesteric liquid crystals are already used in a plethora of display devices, from cellphone displays to large TV displays. In Chapter 7 some potential uses of cholesteric liquid crystal lasers based on newly discovered possibilities uncovered by the presented research will be discussed. The hope exists that in the next decade cholesteric liquid crystal lasers will become a common element in display technologies and numerous other optical devices found in research, industry and in the home.

1.3 Overview of Transformation Optics

Transformation optics is a field that has seen extensive research, particularly over the last two decades. The ideas of TO were first alluded to in 1967, when Veselago discussed the theoretical properties of materials with negative permittivity ε and permeability μ [26]. Initially, his work was not deemed important, as Landau and Lifshitz wrote that "there is certainly no meaning in using the magnetic susceptibility from optical frequencies onwards and in discussion of such phenomena we must put $\mu = 1$" in their textbook series Course of Theoretical Physics [27].

Interest exploded after Pendry's publication in 2000 titled "Negative Refraction Makes a Perfect Lens" [28], in which he develops on Veselago's ideas to present the theory behind a perfect lens. The publication spawned some controversy and a number of published comments [29, 30]. Pendry's publication also propelled the fields of transformation optics and metamaterials into the foreground. Research into both fields has been growing and great advances are being made.

In 2006 Pendry, Shurig and Smith, as well as Leonhardt, independently published seminal works on invisibility cloaks in the same issue of Science magazine. "Optical Conformal Mapping" by Leonhardt used ray optics in the geometric limit [31] while "Controlling Electromagnetic Fields" by Pendry et al. used electromagnetic wave theory to present electromagnetic cloaking devices [32]. In these papers transformation optics was used as a tool to design a particular type of optical device: The invisibility cloak.

TO has since evolved and is being used to develop a host of theoretical devices, many of

which have been experimentally verified with the help of metamaterials. The first example of an experimental invisibility cloak was created by Shurig et al. They use the reduced parameter scheme to develop a 2D cloak, which works for transverse electric polarisation in the microwave regime [33].

Since then a number of different invisibility cloaks were proposed. A carpet cloak, which can be placed over an object in order to hide it, was theorised and simulated by Jensen and Pendry [34] and subsequently built in the microwave regime by Liu et al. [35] and in the visible regime by Gabrielli et al. [36]. Acoustic cloaking has also been researched, with an omnidirectional acoustic cloak being designed and built by Zigoneanu et al. in 2014 [37]. The development of a seismic cloak by Brûlé et al. demonstrates that transformation optics research has already managed to find immediate, real world applications [38]. They show that transformation optics can be used to cloak entire buildings from earthquakes and have collaborated with the Ménard company in France to demonstrate that a seismic cloak works.

More theoretical excursions relying on covariant notation and differential geometry include Leonhardt and Tyc's development of a broadband cloak on a theoretical, branched manifold consisting of a plane and a sphere [39] and the space-time invisibility cloak by McCall et al., which hides events rather than object and is, in essence, a history editor [40]. While Leonhardt and Tyc's concept must remain theoretical as the space they suggested is not physical, McCall et al. have suggested a possible application for their spacetime cloak and subsequent work by Fridman et al. has successfully built a spacetime cloak [41].

Transformation optics, in conjunction with the flexibility provided by metamaterials, has been used for a number of exciting applications. Leonhardt's group are currently using transformation optics in order to conduct research into Hawking radiation by creating optical black and white holes inside an optical fibre. Greenleaf et al. have used transformation optics to construct electromagnetic wormholes, which could be used to produce virtual magnetic monopoles [42]. Mitchell-Thomas et al. developed an analytic technique to perfectly hide objects under a surface, cloaking any bumps caused by the object [43].

Here we list just some of the uses of transformation optics. Numerous other theoretical

and experimental devices exist, ranging from practical applications to wildly imaginative theoretical expositions. These show that the field has sparked the imagination of physicists and the public at large.

In Part II we present our contribution to this exciting field, which develops the refractive index ellipsoid as an object that completely encodes any transformation [4]. It can be used for an intriguing view into the inner workings of any transformation optics device, thereby adding to the growing field of transformation optics in what we hope is a meaningful way.

1.4 Original Research

The presented original research is divided into two separate parts, as discussed in Section 1.1. In Part I the results presented in Chapter 5 represent published independent research, supervised by McCall [1]. Section 5.4 presents recently conducted, as yet unpublished research, which is being prepared for publication. Chapter 6 presents results obtained through joint research with Masters student Wendy Lim, under the supervision of McCall and submitted for publication. Finally, Chapter 7 and Section 5.6 represent an independent exploration into the experimental uses of structurally chiral lasers.

Chapter 3 is a review of structurally chiral media, which expands upon the work previously presented in my Masters thesis [44] and follows the lecture notes and publications by McCall and Lakhtakia [2, 45–58].

Chapter 4 reviews scalar distributed feedback lasers, expanding upon work presented in McCall's lectures [59] and following the seminal publication on the topic by Kogelnik and Shank [3]. Section 4.3 presents the lasing condition for a non-index-matched scalar distributed feedback laser, which was discovered and published during the PhD [1].

In Part II Chapter 13 presents published research on the refractive index of electromagnetically reciprocal media, jointly conducted with Kinsler and McCall [4]. Chapters 10, 11 and 12 review the theory of electromagnetism expressed in differential geometry and construct the theory of transformation optics, combining work by Post [60], Hehl and

Obukhov [61], Landau and Lifshitz [62], Baez [63], Garrity [64] and Thompson [65]. The calculation of the second pair of Maxwell's equations using the principle of least action as well as the calculation of $\tilde{\Gamma}$, both using differential form notation, represent original work.

1.5 Publication and Conference List

An asterisk denotes the presenter of the poster or talk.

Publications

- **Topf, R.D.M.** and McCall, M.W. (2014) 'Modes of structurally chiral lasers', Physical Review A, 90(5). doi: 10.1103/physreva.90.053824.
- McCall, M.W., Kinsler, P. and **Topf, R.D.M.** (2016) 'The refractive index of reciprocal electromagnetic media', Journal of Optics, 18(4), p. 044017. doi: 10.1088/2040-8978/18/4/044017.
- Lim, W.W.Y., McCall, M.W. and **Topf, R.D.M.** (2016) 'Modes of Hybrid Chiral Laser', (*submitted for publication*).

Talks

- **Topf, R.D.M.*** and McCall, M.W. (September 2014) 'Modes of Structurally Chiral Micro-Lasers', Photon14. (London, UK)
- **Topf, R.D.M.***, Lim, W. and McCall, M.W. (January 2016) 'The Hybrid Chiral Laser', Weizmann Institute of Science Seminar. (Rehovot, Israel) *(invited)*
- **Topf, R.D.M.***, Lim, W. and McCall, M.W. (February 2016) 'Modes of Liquid Crystal Lasers', Energy, Materials and Nanotechnology Conference on Liquid Crystals. (Orlando, USA) *(invited)*
- **Topf, R.D.M.***, Lim, W. and McCall, M.W. (April 2016) 'Structurally Chiral Lasers', Imperial College London Seminar. (London, UK)

- **Topf, R.D.M.*** and McCall, M.W. (May 2016) 'Potential uses of Liquid Crystal Lasers', Oxford University Seminar. (Oxford, UK) *(invited)*
- **Topf, R.D.M.***, Lim, W. and McCall, M.W. (September 2016) 'Exotic Chiral Laser Modes', Photon16. (Leeds, UK)
- Guest Lecturer at Imperial College London (April 2014, April 2015, April 2016). Yearly lecture on "Distributed Feedback Lasers and Chiral Lasers" for the Photonic Structures course.

Posters

- **Topf, R.D.M.**, Kinsler, P.* and McCall, M.W. (August 2014) 'Lasing in Chiral Metamaterials', Metamaterials. (Copenhagen, Denmark)
- **Topf, R.D.M.***, McCall, M.W. and Kinsler, P. (January 2015) 'Electromagnetics of Media with $\varepsilon = \mu$', Nanometa. (Seefeld, Austria)
- **Topf, R.D.M.***, McCall, M.W. and Kinsler, P. (January 2015) 'Refractive Index of Electromagnetically Reciprocal Media', Spatial Transformations: From Fundamentals to Applications. (Milton Keynes, UK) (*invited*)

Collaborations

I was on secondment for four months to Professor Ulf Leonhardt at the Weizmann Institute of Science in Israel. During the secondment research into transformation optics was conducted, with a specific focus on the generation of black and white holes in an optical fibre. I also attended a lecture series on General Relativity presented by Leonhardt during the secondment.

In the past year the research into structurally chiral lasers has presented a number of interesting experimental projects. In order to pursue these Professor Stephen Morris at Oxford University was contacted, who conducts experimental research into structurally chiral lasers. Numerous meetings and discussions have taken place, with a joint research project planned for 2017.

Outreach

- Demonstrated at the Schrödinger Lecture reception to invited guests as well as the general public. (November 2014, London, UK)
- Presented at the Imperial Fringe Festival to high school students, promoting interest in further academic studies and the sciences. (February 2015, London, UK)
- Jointly created and presented "The Wonderful World of Polarisation" outreach exhibition at the Imperial College Festival weekend. (April 2015, London, UK)
- Presented "The Wonderful World of Polarisation" at the London Science Museum Lates event. (May 2015, London, UK)
- Presented at the Centre for Academic English at Imperial College London to new students in order to improve their academic English. (August 2016, London, UK)

Part I

Structurally Chiral Lasers

Chapter 2

Introduction to Part I

In Part I of the thesis the theory behind structurally chiral media is presented and used to develop the lasing modes for a number of different structurally chiral lasers. A structurally chiral medium is any medium which consists of a birefringent dielectric with a spatially periodic rotation of the transverse principal axes, as depicted in Figure 2.1. A schematic diagram is presented, as there are numerous materials that classify as structurally chiral media.

There are numerous examples of structurally chiral media in industry and nature. Structurally chiral thin films are birefringent thin films that are deposited one on top of the other, each rotated by a small amount with respect to the previous layer. Chiral nematic liquid crystals are most often organic molecules which self organise in such a way that they exhibit chirality. The exoskeleton of certain beetles is made up of chitin, which forms in chiral layers of thread-like molecules in a protein matrix and also exhibits chirality [66]. Each of these are examples of structurally chiral media, as they have a spatially rotating birefringence. They all affect electromagnetic waves in a similar fashion and the unique properties of these materials and others like them shall be demonstrated in the following chapters.

The calculations in Chapter 3 will demonstrate for right-handed structures such as the one depicted in Figure 2.1 that right circular polarisation (right circular polarisation) is distributively reflected in the same manner to the distributed reflection experienced in a Bragg

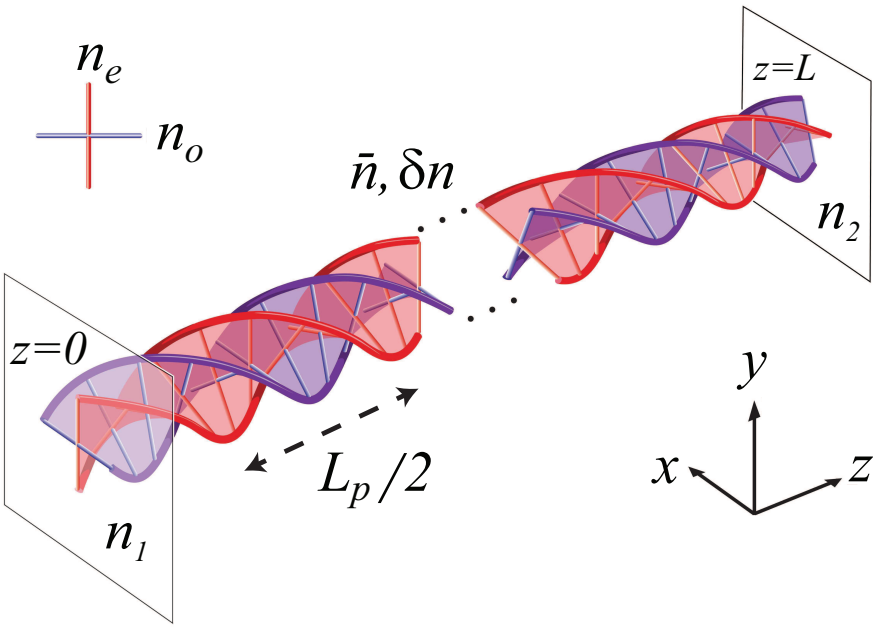

Figure 2.1: Schematic diagram of a right-handed structurally chiral medium with surrounding media of indices n_1 at $z = 0$ and n_2 at $z = L$. The transverse principal axes are aligned with the coordinate axes at $z = 0$, and rotate around the z-axis with period L_p. Reproduced with permission from [1].

grating. In contrast, left circular polarisation travels straight through a right-handed structurally chiral medium, as if it were a homogeneous medium of average refractive index $\bar{n}$. Additionally, the research will make sure to properly account for boundary reflections between the structurally chiral medium and surrounding media, which are chirality reversing and complicate the propagation of electromagnetic waves through structurally chiral media in non-trivial ways.

The structurally chiral medium analysis will form the groundwork from which the theory for numerous chiral lasers that employ structurally chiral media as an integral part of their structure can be developed. As a precursor to these lasers the scalar distributed feedback laser is analysed in Chapter 4, which uses a scalar Bragg grating as its active medium.

The research into the properties and lasing condition of the structurally chiral laser is presented in Chapter 5, which uses a structurally chiral medium as its gain medium. The schematic diagram for it is identical to that of a structurally chiral medium (Figure 2.1),

except that for a structurally chiral laser the ordinary and extraordinary refractive indices (n_o and n_e respectively) have a positive imaginary component to them, which models the gain. The lasing condition for a structurally chiral laser that is index-matched to its surrounding media as well as for one that is not index-matched and therefore includes boundary reflections is developed. Chirality reversing boundary reflections are demonstrated that introduce a new class of lasing modes, which, unlike the conventional right circular polarisation lasing modes found in the index-matched right handed structurally chiral laser, lase left circular polarisation. The implications of these contra-handed modes are discussed and the intriguing possibility is put forward that this class of lasing modes can be used to achieve dynamic polarisation switching.

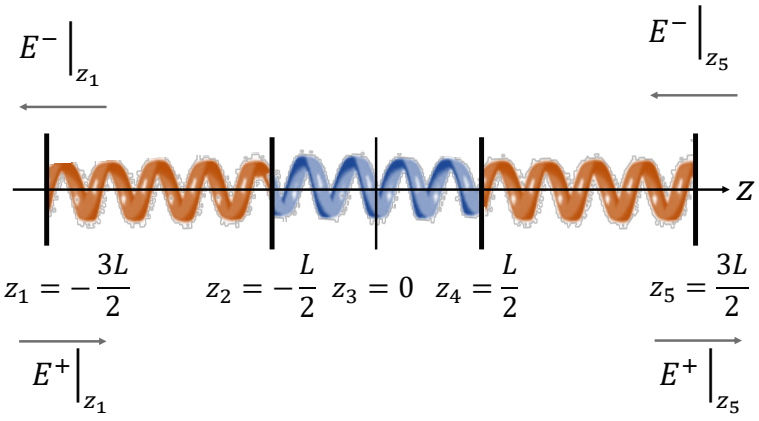

Figure 2.2: Schematic of the hybrid chiral laser consisting of a structurally right-handed active central region surrounded by similar structurally left-handed passive media.

Chapter 6 presents research into the hybrid chiral laser. The hybrid chiral laser has as its active medium a structurally chiral laser and two structurally chiral media of the opposite chirality on either side, which act as polarisation sensitive mirrors (see Figure 2.2). In Section 6.4 research into the theoretical properties of an hybrid chiral laser are presented, which culminate in a theoretical model of the lasing mode structure. It is demonstrated that the hybrid chiral laser uncouples the lasing mechanisms of a structurally chiral laser, thereby providing an added degree of freedom that can be exploited in experimental designs.

The research shows that the hybrid chiral laser is actually a combination of two lasers. It combines the structurally chiral laser analysed in Chapter 3 and the chiral distributed

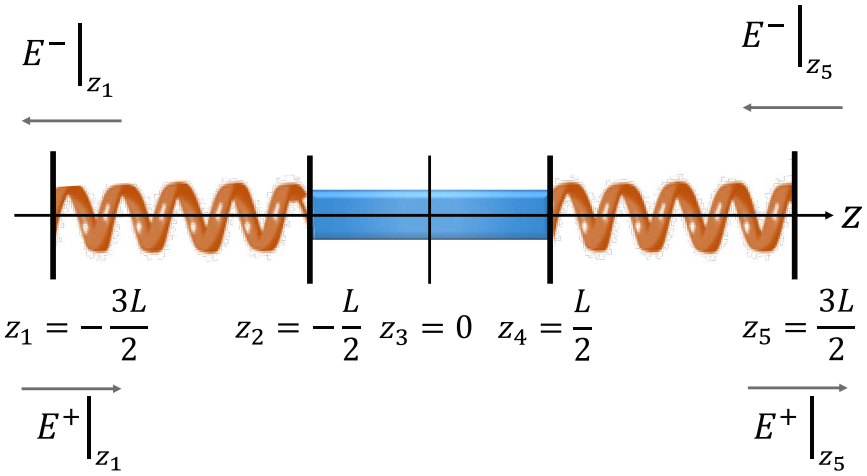

Figure 2.3: Schematic diagram of a Chiral distributed Bragg reflector laser. The active region lies between $z = \pm L/2$ while the passive chiral end mirrors lie between $z = \pm L/2$ and $z = \pm 3L/2$.

Bragg reflector laser, which is a Fabry-Pérot laser with structurally chiral media as its mirrors (see Figure 2.3). Therefore, as a precursor to Section 6.4, in Section 6.3 research into the chiral distributed Bragg reflector laser is presented, the lasing modes are modelled and their intriguing qualities are explained. The research into the chiral distributed Bragg reflector laser and the hybrid chiral laser fully analyses the lasing mode structure of two further chiral lasers. During the analysis intriguing insights into the lasing mode structure are presented, which provide intuition for both lasers.

The analysis of chiral lasers is completed in Chapter 7 with a discussion about the potential uses of chiral lasers in research and industry. This chapter provides a taste of the intriguing uses that chiral lasers may have in the future, given the new possibilities uncovered by the presented research. It provides a crucial spotlight on the concrete applications of the conducted research for research and industry.

Chapter 8 concludes Part I of the thesis by discussing the further research avenues that form logical continuations to the presented research. These comprise of both theoretical research and experimental research, for which a recent collaboration with an experimental research group in Oxford led by Dr. Morris is being introduced. Chapter 8 sheds light on some of the intriguing areas of research left to explore and demonstrates that the vibrant field of Chiral Lasers has great potential.

Chapter 3

Structurally Chiral Media

3.1 Introduction to Structurally Chiral Media

A structurally chiral medium is any medium which consists of a birefringent dielectric with a spatially periodic rotation of the transverse principal axes, as depicted in Figure 2.1 in the previous chapter. The two principal axes, in red and purple, have a refractive index of n_e and n_o respectively. The structure begins at $z = 0$ where a transition exists from the material outside the structurally chiral medium with refractive index n_1. As z increases the principal axes rotate with a right-handed twist at a fixed period of L_p. The twist could also be left-handed, however to ease the discussion and without loss of generality the assumption is made that the structurally chiral medium is right-handed, unless specified otherwise. Notice that the material from which the structurally chiral medium is made has only completed half a rotation by the time the principal axes have already returned to their original position. The period of rotation of the material is therefore half the period of rotation of the principle axes. Inside the structure the average refractive index is given by

$$\bar{n} = \frac{n_e + n_o}{2} \tag{3.1}$$

and the difference between the ordinary and extraordinary refractive indices is given by $\delta n = n_e - n_o$. At $z = L$ the structurally chiral medium ends and is incident to a material with a refractive index of n_2. This is the simplest type of structurally chiral medium and

the only one analysed in this chapter. Other examples can include variations in period or sudden twist defects, often found in nature, such as on the exoskeleton of certain beetles [66]. Examples of structurally chiral media include chiral sculptured thin films [56] and cholesteric liquid crystals [25].

Structurally chiral media have many potential uses in research and industry. They provide polarization specific distributed feedback: Circularly polarised light co-polarised with the medium helicity sees an index modulation of amplitude equal to the local birefringence δn, whereas the orthogonal circular polarization propagates as if through a uniform medium of average refractive index $\bar{n}$. Structurally chiral media can be found integrated into many photonic components, anywhere circular polarisation states need to be manipulated independently.

A prototypical example for the use of structurally chiral media is in optical communications, where their chiral selectivity can be exploited to add a further degree of freedom, thereby effectively doubling the bandwidth. A twisted birefringent glass fibre is also an example of a structurally chiral medium. Chiral Photonics Inc. are in the business of making such fibres for use as couplers, optical switches, polarisers, sensors and lasers [67].

3.2 Problem Statement

In order to understand the electromagnetic properties of a structurally chiral medium it is necessary to solve Maxwell's equations for electromagnetic waves travelling through it. There is a very good approximation using coupled wave theory and an analytic solution using Oseen transformations, which shall be demonstrated in Sections 3.3 and 3.4, respectively. The obtained solution from either method can be used to better understand the propagation of waves through a structurally chiral medium and explicitly calculate the structure's effective reflectances and transmittances. Note that throughout the thesis vectors are expressed in bold ($\mathbf{r}$), matrices with an underline ($\underline{M}$) and functions are introduced explicitly as maps ($f : A \to \mathbb{R}$).

We begin with Maxwell's equations in the frequency domain for a dielectric medium in

the absence of free currents or sources:

$$\nabla \times \mathbf{E}(\mathbf{r},\omega) = i\omega \mathbf{B}(\mathbf{r},\omega), \tag{3.2}$$

$$\nabla \times \mathbf{H}(\mathbf{r},\omega) = -i\omega \mathbf{D}(\mathbf{r},\omega), \tag{3.3}$$

$$\nabla \cdot \mathbf{D}(\mathbf{r},\omega) = 0, \tag{3.4}$$

$$\nabla \cdot \mathbf{B}(\mathbf{r},\omega) = 0, \tag{3.5}$$

where $\mathbf{E}$ represents the *electric field strength*, $\mathbf{H}$ the *magnetising field*, $\mathbf{D}$ the *displacement field*, $\mathbf{B}$ the *magnetic field strength*, $\mathbf{r}$ the position vector and ω the frequency.

The constitutive relations for a structurally chiral medium relating the fields simplify to

$$\mathbf{D}(\mathbf{r},\omega) = \underline{\varepsilon}\mathbf{E}(\mathbf{r},\omega), \tag{3.6}$$

$$\mathbf{B}(\mathbf{r},\omega) = \mu_0 \mathbf{H}(\mathbf{r},\omega), \tag{3.7}$$

where $\underline{\varepsilon}$ represents the permittivity and μ_0 is the permeability of free space. These fields as well as Maxwell's equations and the constitutive relations are analysed in greater detail and more generality in Chapters 10-12 in Part II in order to develop transformation optics. However, that analysis is not necessary in this part of the thesis.

For structurally chiral media these equations can be simplified further by assuming that for a structurally chiral medium aligned along the z-axis the permittivity depends only on z and ω. Equation (3.6) can then be rewritten as

$$\mathbf{D}(\mathbf{r},\omega) = \varepsilon_0 \underline{\varepsilon(z,\omega)} \mathbf{E}(\mathbf{r},\omega), \tag{3.8}$$

where ε_0 is the permittivity of free space and $\underline{\varepsilon}$ has been restricted to a dependence on z and ω only. The analysis of structurally chiral media begins with Equations (3.2)-(3.5), (3.7) and (3.8).

Consider a plane wave incident on a structurally chiral medium travelling in the z-direction, so that

$$\mathbf{E}(\mathbf{r},\omega) = \mathbf{E}(z,\omega) = \mathbf{E}(z)\exp\{-i\omega t\}. \tag{3.9}$$

From Equations (3.2) and (3.7) we have that

$$\left[\hat{\mathbf{z}} \times \frac{\mathrm{d}}{\mathrm{d}z}\mathbf{E}\left(z,\omega\right)\right]_{\perp} = i\omega\mu_0 \left[\mathbf{H}\left(z,\omega\right)\right]_{\perp}, \tag{3.10}$$

where $\hat{\mathbf{z}} = (0,0,1)^T$ is the unit vector in the z-direction and we define the $\perp$ operator as sending 3 vectors to their 2-dimensional projection in the x-y plane and restricting 3×3 matrices to their upper left minor:

$$\begin{pmatrix} v_1 \\ v_2 \\ v_3 \end{pmatrix}_{\perp} = \begin{pmatrix} v_1 \\ v_2 \end{pmatrix}, \quad \begin{pmatrix} a_{11} & a_{12} & a_{13} \\ a_{21} & a_{22} & a_{23} \\ a_{31} & a_{32} & a_{33} \end{pmatrix}_{\perp} = \begin{pmatrix} a_{11} & a_{12} \\ a_{21} & a_{22} \end{pmatrix}. \tag{3.11}$$

We rely on the $\perp$ operator in Equation (3.10) to simplify our calculations by using the fact that $\left[\hat{\mathbf{z}} \times \frac{\mathrm{d}}{\mathrm{d}z}\mathbf{E}\left(z,\omega\right)\right]_z = 0$, where $[*]_z$ represents the z-component of a given vector.

A similar simplification for $\mathbf{H}\left(\mathbf{r},\omega\right) = \mathbf{H}(z)\exp\left\{-i\omega t\right\}$ yields

$$\left[\hat{\mathbf{z}} \times \frac{\mathrm{d}}{\mathrm{d}z}\mathbf{H}\left(z,\omega\right)\right]_{\perp} = -i\omega \left[\mathbf{D}\left(z,\omega\right)\right]_{\perp}. \tag{3.12}$$

We would like to solve Equations (3.10) and (3.12) for $\mathbf{H}\left(\mathbf{r},\omega\right)$ and $\mathbf{E}\left(\mathbf{r},\omega\right)$. We note that

$$\left[\hat{\mathbf{z}} \times \frac{\mathrm{d}}{\mathrm{d}z}\mathbf{H}\left(z,\omega\right)\right]_z = -i\omega \left[\mathbf{D}\left(z,\omega\right)\right]_z = 0 \implies \left[\mathbf{D}\left(z,\omega\right)\right]_z = 0. \tag{3.13}$$

We can rewrite Equation (3.8) as

$$\mathbf{E}\left(z,\omega\right) = \varepsilon_0^{-1}\underline{\varepsilon\left(z,\omega\right)}^{-1}\mathbf{D}\left(z,\omega\right), \tag{3.14}$$

so that

$$\mathbf{E}_{\perp} = \varepsilon_0^{-1}\left[\underline{\varepsilon\left(z,\omega\right)}^{-1}\mathbf{D}\left(z,\omega\right)\right]_{\perp}. \tag{3.15}$$

Using Equation (3.13) we find that

$$\left[\underline{\varepsilon}^{-1}\mathbf{D}\right]_{\perp} = \left(\underline{\varepsilon}^{-1}\right)_{\perp}\mathbf{D}_{\perp}, \tag{3.16}$$

so that

$$\mathbf{E}_\perp = \varepsilon_0^{-1} \left(\underline{\varepsilon}^{-1}\right)_\perp \mathbf{D}_\perp. \tag{3.17}$$

We thus have $\mathbf{D}_\perp = \varepsilon_0 \left[\left(\underline{\varepsilon}^{-1}\right)_\perp\right]^{-1} \mathbf{E}_\perp$, which we can use to rewrite Equation (3.12) as

$$\left[\hat{\mathbf{z}} \times \frac{\mathrm{d}}{\mathrm{d}z}\mathbf{H}(z,\omega)\right]_\perp = -i\omega\varepsilon_0 \left[\left(\underline{\varepsilon}^{-1}\right)_\perp\right]^{-1} \mathbf{E}_\perp. \tag{3.18}$$

Let us now evaluate $\left[\left(\underline{\varepsilon}^{-1}\right)_\perp\right]^{-1} \mathbf{E}_\perp$ in more detail. For a structurally chiral medium such as we are examining, the permittivity matrix is given by [2]

$$\underline{\varepsilon} = \underline{\mathrm{R}} \cdot \underline{\chi} \cdot \underline{\varepsilon_{ref}} \cdot \underline{\chi}^{-1} \cdot \underline{\mathrm{R}}^{-1}, \tag{3.19}$$

where

$$\underline{\mathrm{R}} = \begin{bmatrix} \cos pz & -\sin pz & 0 \\ \sin pz & \cos pz & 0 \\ 0 & 0 & 1 \end{bmatrix}, \underline{\chi} = \begin{bmatrix} \cos\theta & 0 & -\sin\theta \\ 0 & 1 & 0 \\ \sin\theta & 0 & \cos\theta \end{bmatrix}, \underline{\varepsilon_{ref}} = \begin{bmatrix} \varepsilon_b & 0 & 0 \\ 0 & \varepsilon_c & 0 \\ 0 & 0 & \varepsilon_a \end{bmatrix}. \tag{3.20}$$

Here $\underline{\varepsilon_{ref}}$ is the permittivity of the dielectric medium used to create the structurally chiral medium, where the incident plane is set up in such a way that the c-axis of the dielectric is aligned parallel to the y-axis and the b-axis of the dielectric lies in the $x-z$ plane at an angle θ to the x-axis. The $\underline{\chi}$ matrix accounts for the angle of rise θ. It effectively replaces ε_b in $\underline{\varepsilon_{ref}}$ with $\varepsilon_d = \varepsilon_a\varepsilon_b / \left(\varepsilon_b \cos^2\theta + \varepsilon_a \sin^2\theta\right)$. The $\underline{\mathrm{R}}$ matrix constructs the chiral nature of the structurally chiral medium and $p = 2\pi/L_p$. Note that a positive L_p and thus a positive p corresponds to a right-handed structure. We then calculate that

$$\left[\left(\underline{\varepsilon}^{-1}\right)_\perp\right]^{-1} = \begin{pmatrix} \varepsilon_d \cos^2 pz + \varepsilon_c \sin^2 pz & (\varepsilon_d - \varepsilon_c)\sin pz \cos pz \\ (\varepsilon_d - \varepsilon_c)\sin pz \cos pz & \varepsilon_d \sin^2 pz + \varepsilon_c \cos^2 pz \end{pmatrix}. \tag{3.21}$$

We have simplified the problem to a set of four ordinary differential equations, which we can express as follows:

$$\frac{\mathrm{d}}{\mathrm{d}z}\mathbf{F} = i\underline{G}(z)\,\mathbf{F}(z), \tag{3.22}$$

where $\mathbf{F} = \begin{bmatrix} E_x & E_y & H_x & H_y \end{bmatrix}^T$ and

$$\underline{G}(z) = \begin{bmatrix} 0 & 0 & 0 & \omega\mu_0 \\ 0 & 0 & -\omega\mu_0 & 0 \\ -\omega\varepsilon_0(\varepsilon_d - \varepsilon_c)\sin pz\cos pz & -\omega\varepsilon_0(\varepsilon_d \sin^2 pz + \varepsilon_c \cos^2 pz) & 0 & 0 \\ \omega\varepsilon_0(\varepsilon_d \cos^2 pz + \varepsilon_c \sin^2 pz) & \omega\varepsilon_0(\varepsilon_d - \varepsilon_c)\sin pz\cos pz & 0 & 0 \end{bmatrix}. \tag{3.23}$$

Thus, we have simplified the initial problem statement consisting of six ordinary differential equations given by Equations (3.2)-(3.5), (3.7) and (3.8) using the properties of structurally chiral media to a set of four ordinary differential equations, which we can now solve.

As Equation (3.22) is a first-order matrix differential equation it has a solution of the form

$$\mathbf{F}|_z = \underline{M}(z)\,\mathbf{F}|_0, \tag{3.24}$$

where $\mathbf{F}|_z$ is the value of $\mathbf{F}$ at a distance z into the structurally chiral medium and $\mathbf{F}|_0$ is the value of $\mathbf{F}$ at incidence. Note that we are dealing with matrices and therefore

$$\underline{M}(z) \neq \exp\left\{ i \int_0^z \underline{G}(z)\,\mathrm{d}z \right\} \tag{3.25}$$

in general. If G is independent of z, Equation (3.25) does hold, which will be used for the Oseen solution in Section 3.4.

3.3 Coupled Wave Theory of Structurally Chiral Media

Ultimately, we would like to arrive at Equation (3.24) in order to have the fields for $z = L$, given an initial field configuration at $z = 0$. We can then use our results to calculate effective reflectances and transmittances for the structurally chiral medium.

There are a number of ways to solve Equation (3.22) in order to find $\underline{M}$ in Equation (3.24). Any computational ordinary differential equation solver can solve the four ordinary differential equations numerically to a high degree of accuracy. However, in order to get

an insight into how the fields propagate inside the structure, it is instructive to solve the ordinary differential equations approximately using coupled wave theory. Coupled wave theory stipulates that there is a forward and backward propagating component to the electromagnetic fields and that these components are coupled to each other. From that intuitive assumption and some manipulations, a model can be constructed. It should become evident in the remainder of Part I that without resorting to coupled wave theory it is much harder to analyse and understand structurally chiral media, structurally chiral lasers and hybrid chiral lasers.

An analytic solution to the problem statement defined in Section 3.2 also exists, which makes use of the Oseen transformation and is known as the Oseen method. It translates the problem into a frame that rotates with the principal axes of birefringence. While this method is analytic, the resulting fields, as well as the reflectances and transmittances, are difficult to write down and even harder to interpret. We therefore use the Oseen method as a check for the results obtained from coupled wave theory and will demonstrate in Section 3.4 that the two methods agree to a very high degree.

Using coupled wave theory, we begin by stipulating that $\mathbf{E}_\perp$ can be expanded into a forward and backward propagating component as

$$\mathbf{E}_\perp = \mathbf{A}^+ \exp\{ikz\} + \mathbf{A}^- \exp\{-ikz\}, \tag{3.26}$$

where $k = \bar{n}k_0$ is the wave number, $\bar{n} = [(\varepsilon_c + \varepsilon_d)/2]^{1/2} \approx (n_e + n_o)/2$ is the average refractive index, $k_0 = \omega/c$ is the free-space wave number, ω is the angular frequency of the electromagnetic wave and c is the speed of light in a vacuum.

We further expand the forward and backward propagating components of $\mathbf{E}_\perp$ into left circular polarisation and right circular polarisation components, so that

$$\mathbf{A}^+ = \frac{1}{\sqrt{2}} A_L^+(z) \begin{pmatrix} 1 \\ i \end{pmatrix} + \frac{1}{\sqrt{2}} A_R^+(z) \begin{pmatrix} 1 \\ -i \end{pmatrix}, \tag{3.27}$$

$$\mathbf{A}^- = \frac{1}{\sqrt{2}} A_L^-(z) \begin{pmatrix} 1 \\ -i \end{pmatrix} + \frac{1}{\sqrt{2}} A_R^-(z) \begin{pmatrix} 1 \\ i \end{pmatrix}. \tag{3.28}$$

This splits $\mathbf{A}^+$ and $\mathbf{A}^-$ into two linearly independent Eigenvectors

$$v_R = \frac{1}{\sqrt{2}} \begin{pmatrix} 1 \\ -i \end{pmatrix}, \; v_L = \frac{1}{\sqrt{2}} \begin{pmatrix} 1 \\ i \end{pmatrix} \tag{3.29}$$

with different magnitudes $A^{+/-}_{L/R}$. The v_R Eigenvector represents right circular polarisation and the v_L Eigenvector represents left circular polarisation for a choice of basis where

$$v_x = \begin{pmatrix} 1 \\ 0 \end{pmatrix}, \; v_y = \begin{pmatrix} 0 \\ 1 \end{pmatrix}, \tag{3.30}$$

represent horizontally and vertically polarised light, respectively. This is the standard Jones vector notation, used to describe the polarisation state of light and following Hecht's notation, where the phase of the light is given by $\phi = kz - \omega t$ [68].

We combine Equations (3.10) and (3.18) to arrive at the Helmholtz equation:

$$\frac{\mathrm{d}^2 \mathbf{E}_\perp}{\mathrm{d}z^2} + k_0^2 \left[\left(\underline{\varepsilon}^{-1} \right)_\perp \right]^{-1} \mathbf{E}_\perp = 0. \tag{3.31}$$

3.3.1 Calculating the propagation equation

We can rewrite

$$\left[\left(\underline{\varepsilon}^{-1} \right)_\perp \right]^{-1} = \underline{\mathrm{R}}_\perp \, \mathrm{diag} \left(\epsilon_d, \epsilon_c \right) \left(\underline{\mathrm{R}}_\perp \right)^{-1} \tag{3.32}$$

and

$$\underline{\mathrm{R}}_\perp = \frac{1}{2} \left(\sigma e^{ipz} + \sigma^* e^{-ipz} \right), \tag{3.33}$$

where

$$\sigma = \begin{pmatrix} 1 & i \\ -i & 1 \end{pmatrix}. \tag{3.34}$$

Note that

$$\text{diag}\left(a_1, ..., a_n\right) \equiv \begin{pmatrix} a_1 & 0 & \dots & 0 \\ 0 & \ddots & \ddots & \vdots \\ \vdots & \ddots & \ddots & 0 \\ 0 & \dots & 0 & a_n \end{pmatrix}. \tag{3.35}$$

We can now solve the Helmholtz equation (3.31) using Equations (3.26)-(3.28) and (3.32)-(3.34). We can then use the solution found for $\mathbf{E}_\perp$ to solve for the complete electromagnetic fields.

We begin by simplifying the Helmholtz equation (3.31) to

$$\begin{aligned} &\left(2ik\frac{\mathrm{d}\mathbf{A}^+}{\mathrm{d}z} + \frac{\mathrm{d}^2\mathbf{A}^+}{\mathrm{d}z^2}\right)e^{ikz} + \left(-2ik\frac{\mathrm{d}\mathbf{A}^-}{\mathrm{d}z} + \frac{\mathrm{d}^2\mathbf{A}^-}{\mathrm{d}z^2}\right)e^{-ikz} \\ = \;& \left(\bar{n}k_0\right)^2 \boldsymbol{E}_\perp - k_0^2 \underline{\mathrm{R}}_\perp \text{diag}\left(\epsilon_d, \epsilon_c\right)\left(\underline{\mathrm{R}}_\perp\right)^{-1}\boldsymbol{E}_\perp. \end{aligned} \tag{3.36}$$

To solve Equation (3.36) we note that $\mathbf{A}^-$ and $\mathbf{A}^+$ are envelope functions and use the slowly varying envelope approximation to neglect the second order derivatives, thereby simplifying the equation [2].

We rewrite

$$\text{diag}\left(\epsilon_d, \epsilon_c\right) = \bar{n}^2\mathbb{I} + \frac{\left(\epsilon_d - \epsilon_c\right)}{2}\mathbb{J}, \tag{3.37}$$

where $\mathbb{I} = \text{diag}\left(1, 1\right)$ and $\mathbb{J} = \text{diag}\left(1, -1\right)$, to find that the right hand side of Equation (3.36) can be written as

$$-k_0^2\frac{\left(\epsilon_d - \epsilon_c\right)}{2}\underline{\mathrm{R}}_\perp\mathbb{J}\left(\underline{\mathrm{R}}_\perp\right)^{-1}\boldsymbol{E}_\perp. \tag{3.38}$$

We rewrite $\underline{\mathrm{R}}_\perp$ and $\left(\underline{\mathrm{R}}_\perp\right)^{-1}$ in terms of σ to find that Expression (3.38) becomes

$$-k_0^2\frac{\left(\epsilon_d - \epsilon_c\right)}{4}\left(\begin{pmatrix} 1 & i \\ i & -1 \end{pmatrix}\cdot\mathbf{A}^+e^{iz(-2p+k)} + \begin{pmatrix} 1 & -i \\ -i & -1 \end{pmatrix}\cdot\mathbf{A}^-e^{iz(2p-k)}\right). \tag{3.39}$$

From Equation (3.36) we can see that any solution will have to be approximately phase matched to the period of the structure. This argument is made in most texts on the subject and is one of the underlying ideas behind coupled wave theory. Thus, we are only

interested in the case where the wavelength of the incident light is approximately matched to the period of the chiral structure.

We chose a right handed structurally chiral medium, which implies that $p > 0$. Therefore, in order to phase match the right and left side of Equation (3.36), we must have $p \approx k$. We define $\delta k = 2\,(k - p)$ and phase match Equation (3.39) to the left hand side of (3.36) to find that

$$-k_0^2 \frac{(\epsilon_d - \epsilon_c)}{8ik} \begin{pmatrix} 1 & -i \\ -i & -1 \end{pmatrix} \mathbf{A}^- e^{-iz\delta k} = \frac{\mathrm{d}\mathbf{A}^+}{\mathrm{d}z}, \tag{3.40}$$

$$k_0^2 \frac{(\epsilon_d - \epsilon_c)}{8ik} \begin{pmatrix} 1 & i \\ i & -1 \end{pmatrix} \mathbf{A}^+ e^{iz\delta k} = \frac{\mathrm{d}\mathbf{A}^-}{\mathrm{d}z}. \tag{3.41}$$

Thus we have simplified the Helmholtz equation (3.31) to a set of two coupled first order differential equations, which we shall now solve.

We rewrite

$$-\frac{k_0^2\,(\epsilon_d - \epsilon_c)}{8ik} \approx \frac{i\kappa}{2}, \tag{3.42}$$

where

$$\kappa = \frac{\pi\,(n_d - n_c)}{\lambda_0}. \tag{3.43}$$

We use Equations (3.27) and (3.28), define $\mathbf{u} = \begin{bmatrix} 1 & i \end{bmatrix}^T$, $\mathbf{v} = \begin{bmatrix} 1 & -i \end{bmatrix}^T$ and use the relations between $\mathbf{u}$, $\mathbf{v}$, $\begin{pmatrix} 1 & -i \\ -i & -1 \end{pmatrix}$ and $\begin{pmatrix} 1 & i \\ i & -1 \end{pmatrix}$ to find that Equation (3.40) can be rewritten as

$$i\kappa A_R^- \mathbf{v} e^{-iz\delta k} = \frac{\mathrm{d}A_L^+}{\mathrm{d}z}\mathbf{u} + \frac{\mathrm{d}A_R^+}{\mathrm{d}z}\mathbf{v}. \tag{3.44}$$

Multiplying Equation (3.44) by $\mathbf{u}$ and $\mathbf{v}$ provides

$$\frac{\mathrm{d}A_R^+}{\mathrm{d}z} = i\kappa e^{-iz\delta k} A_R^- \quad , \quad \frac{\mathrm{d}A_L^+}{\mathrm{d}z} = 0. \tag{3.45}$$

Identical manipulations of Equation (3.41) show that

$$\frac{\mathrm{d}A_R^-}{\mathrm{d}z} = -i\kappa e^{iz\delta k} A_R^+ \quad , \quad \frac{\mathrm{d}A_L^-}{\mathrm{d}z} = 0. \tag{3.46}$$

In summary, we have that

$$\frac{\mathrm{d}}{\mathrm{d}z}\begin{pmatrix} A_L^+(z) \\ A_R^+(z) \end{pmatrix} = i\kappa \begin{pmatrix} 0 & 0 \\ 1 & 0 \end{pmatrix} \begin{pmatrix} A_R^- \\ A_L^- \end{pmatrix} e^{-i\delta kz}, \tag{3.47}$$

$$\frac{\mathrm{d}}{\mathrm{d}z}\begin{pmatrix} A_R^-(z) \\ A_L^-(z) \end{pmatrix} = -i\kappa \begin{pmatrix} 0 & 1 \\ 0 & 0 \end{pmatrix} \begin{pmatrix} A_L^+ \\ A_R^+ \end{pmatrix} e^{i\delta kz}, \tag{3.48}$$

when separated into forward and backwards propagating waves.

Alternatively, we can separate the differential equations into left and right circularly polarised light to find that

$$\frac{\mathrm{d}}{\mathrm{d}z}\begin{pmatrix} A_L^+(z) \\ A_L^-(z) \end{pmatrix} = \mathbf{0}, \tag{3.49}$$

$$\frac{\mathrm{d}}{\mathrm{d}z}\begin{pmatrix} A_R^+(z) \\ A_R^-(z) \end{pmatrix} = i\kappa \begin{pmatrix} 0 & e^{-i\delta kz} \\ -e^{i\delta kz} & 0 \end{pmatrix} \begin{pmatrix} A_R^+ \\ A_R^- \end{pmatrix}. \tag{3.50}$$

These equations can be solved to find that for $0 < z < L$

$$\begin{bmatrix} E_R^+(z) \\ E_R^-(z) \\ E_L^+(z) \\ E_L^-(z) \end{bmatrix} = \begin{pmatrix} P^+(z) & Q^+(z) & 0 & 0 \\ Q^-(z) & P^-(z) & 0 & 0 \\ 0 & 0 & e^{ikz} & 0 \\ 0 & 0 & 0 & e^{-ikz} \end{pmatrix} \begin{bmatrix} E_R^+(0^+) \\ E_R^-(0^+) \\ E_L^+(0^+) \\ E_L^-(0^+) \end{bmatrix}, \tag{3.51}$$

where

$$E_{L,R}^{\pm}(z) = A_{L,R}^{\pm}(z)\, e^{\pm ikz}, \tag{3.52}$$

$$P^{\pm}(z) = e^{\pm ipz}\left[\cosh(\Delta z) \pm i\frac{\delta k}{2\Delta}\sinh(\Delta z)\right], \tag{3.53}$$

$$Q^{\pm}(z) = \pm\frac{ie^{\pm ipz}\kappa}{\Delta}\sinh(\Delta z), \tag{3.54}$$

$$\Delta = \left[|\kappa|^2 - \left(\frac{\delta k}{2}\right)^2\right]^{\frac{1}{2}}, \tag{3.55}$$

and the superscript in 0^+ indicates that the field values on the right of the boundary are

being considered.

3.3.2 Calculating the distributed reflectance and transmittance

We can use Equation (3.51) to help gain a deeper understanding of the effects of structurally chiral media, subject to the approximations previously made. We are primarily interested in the reflectance and transmittance of the structurally chiral medium with respect to the circular polarisation of the incident light.

We begin by observing that left circular polarisation propagates as if no refractive index change occurs, as evidenced by Equation (3.49). The calculations suggest that left circular polarisation is completely oblivious to the structure of the structurally chiral medium. Left circular polarisation registers no change in refractive index, even when the phases are not phase matched and $\delta k \not\approx 0$. Thus, left circular polarisation acts as if it were traveling through a homogeneous medium with a refractive index $\bar{n}$.

When examining the top two lines of Equation (3.51) we see that forward and backward propagating right circular polarisation registers a sinusoidally varying refractive index. The environment experienced by right circular polarisation is identical to the environment experienced by light of any polarisation travelling through a sinusoidally varying Bragg grating with twice the pitch (see Equation (4.4) in Section 4.2 and [69]).

To calculate the reflectance and transmittance of the modes we note first that while $E_R^+(0)$ is known to be the incident right circular polarisation, $E_R^-(0)$ is not known. Instead we know that $E_R^-(L) = 0$, as the reflected field at the far boundary is 0 when we ignore any boundary reflections occurring between the surrounding media and the structurally chiral medium. (The boundary reflections will be considered later.) To find the amplitude reflectance for right circular polarisation entering the structurally chiral medium at $z = 0$, which we label $r_c = E_R^-(0)/E_R^+(0)$, we rewrite the second line in Equation (3.51) and find that

$$r_c = -\frac{Q^-(L)}{P^-(L)}. \tag{3.56}$$

Further, we calculate using Equation (3.51) that the amplitude transmittance for right circular polarisation entering the structurally chiral medium at $z = 0$, which we label $t_c = E_R^+(L)/E_R^+(0)$, is

$$t_c = \frac{1}{P^-(L)}. \tag{3.57}$$

Note that while the amplitude transmittance for right circular polarisation at $z = 0$ equals the amplitude transmittance for right circular polarisation at $z = L$ this is not true for the reflectance. A phase change is introduced, so that

$$r_c|_{z=L} = e^{2ipL} r_c|_{z=0}. \tag{3.58}$$

We would like to calculate the reflected and transmitted intensity of circularly polarised light entering the structure. We label the reflected intensity R and the transmitted intensity T and use the first subscript to denote the initial polarisation and the second subscript to denote the final polarisation. R_{RL} is therefore the intensity of right circular polarisation entering the structurally chiral medium and being reflected as left circular polarisation. We know that $T_{RR} + T_{LR} + R_{RR} + R_{LR} = 1$, as we have introduced no loss or gain. As we are inside the structurally chiral medium ($0 < z < L$) we have no effects that reverse the direction of polarisation from right to left or vice versa and thus we find that $T_{RR} = 1 - R_{RR}$ in the index matched case. We can calculate these as

$$T_{RR} = |t_c|^2 = \left|\cosh(\Delta L) - i\frac{\delta k}{2\Delta}\sinh(\Delta L)\right|^{-2}, \tag{3.59}$$

$$R_{RR} = |r_c|^2 = \left|\frac{\kappa \sinh(\Delta L)}{\Delta\cosh(\Delta L) + i(\delta k/2)\sinh(\Delta L)}\right|^2. \tag{3.60}$$

The calculations above have simplified the problem to that of two separate Eigenstates characterised by the direction of the circular polarisation of the incident light. The first Eigenstate (left circular polarisation) travels through an effectively homogeneous medium, the second Eigenstate (right circular polarisation) travels through an effectively sinusoidal Bragg grating.

t_c and r_c are the amplitude reflectance and transmittance of right circular polarisation inside the structurally chiral medium caused by the distributed feedback inside the structure. We therefore call them the *distributed* reflection and transmission coefficients.

3.3.3 Calculating the resultant reflectance and transmittance

Ultimately, we are interested in calculating the reflectances and transmittances of light incident from a medium of refractive index n_1 at $z = 0$ travelling into the structurally chiral medium and either being reflected back out or transmitted through the structurally chiral medium into an incident medium of refractive index n_2 at $z = L$. These we call the *resultant* reflection and transmission coefficients.

Calculating these is not trivial, as the distributed reflectance and transmittance are chirality dependent and the reflections at the interfaces of the structurally chiral medium with the surrounding medium are chirality reversing. In contrast, the distributed reflection inside the structurally chiral medium is chirality preserving. There are therefore numerous different possibilities for the propagation path of light incident on the structurally chiral medium, which are definitively developed in [2].

We are guided by the following structure:

1. We begin by defining the *interface,* as well as the *distributed,* reflection/transmission coefficients, which will form the components of our calculations.

2. We then calculate the *internal* reflection/transmission coefficients by considering all possible paths that light can take inside the structurally chiral medium.

3. We finish by calculating the *resultant* reflection/transmission coefficients by multiplying the internal reflection/transmission coefficients by appropriate interface reflection/transmission coefficients, which will account for the interfaces between the structurally chiral medium and the surrounding media.

There are two different types of reflections/transmissions in structurally chiral media:

1. *Interface* reflections/transmissions occur at the boundaries of a structurally chiral medium with the surrounding medium. They are Fresnel reflection/transmission coefficients, they occur at discontinuities of the refractive index and they reverse the chirality of the light.

2. *Distributed* reflections/transmissions occur along the length of a structurally chiral medium (i.e. inside the actual structurally chiral medium, as opposed to at its boundaries or in the surrounding media). These are not associated to discontinuities in the refractive index, they do not reverse chirality and they are given by Equations r_c and t_c calculated previously.

We first state the *interface* reflection/transmission coefficients. These are

$$r_{1c} = \frac{n_1 - \bar{n}}{n_1 + \bar{n}} = -r_{c1} = r_1, \tag{3.61}$$

$$r_{2c} = \frac{n_2 - \bar{n}}{n_2 + \bar{n}} = -r_{c2} = r_2, \tag{3.62}$$

$$t_{1c} = \frac{2n_1}{n_1 + \bar{n}} = \left(\frac{n_1}{\bar{n}}\right) t_{c1}, \tag{3.63}$$

$$t_{2c} = \frac{2n_2}{n_2 + \bar{n}} = \left(\frac{n_2}{\bar{n}}\right) t_{c2}, \tag{3.64}$$

where r_{1c} for instance is the reflection coefficient of light rays approaching the incident boundary at $z = 0$ from outside the structurally chiral medium. Note that we labelled $r_{1c} = r_1$ and $r_{c2} = r_2$ for later use.

We now have both the *interface* and the *distributed* reflection/transmission coefficients and can calculate the *internal* reflection/transmission coefficients by considering the propagation path of light incident on a structurally chiral medium. There are clear restrictions as to which paths circularly polarised light can take in a structurally chiral medium. These stem from the intrinsic properties of a structurally chiral medium, which state that polarised light co-handed with the helicity of the structurally chiral medium registers a varying refractive index while polarised light contra-handed with the helicity of the structurally chiral medium registers a homogeneous medium, passing straight through the structure. For a right handed structurally chiral medium the allowed light paths are restricted by the following rules:

1. Reflections at the boundary of the structurally chiral medium are chirality reversing.
2. Distributive reflections inside the structurally chiral medium are chirality preserving.
3. Left circular polarisation experiences a homogeneous refractive index inside the structurally chiral medium and will therefore only reflect at the boundaries.
4. right circular polarisation experiences a varying refractive index and will therefore partially reflect along the length of the structurally chiral medium and partially reflect at the boundaries.

These restrictions imply that there are exactly four paths that pure circularly polarised light can take to complete one round trip in a structurally chiral medium. These paths are shown schematically in Figure 3.1 [2]. The vertical lines in Figure 3.1 represent the boundaries of the structurally chiral medium while the curved arrow represents the light path. Each section of the light path is labelled with the respective polarisation state of that section. A curve in the light path at a boundary represents a reflection. A curve in the light path inside the structurally chiral medium represents a distributed reflection. Note that in reality these distributed reflections occur continuously in the interior of the structurally chiral medium and not abruptly in the middle of the structure as suggested by the diagrams.

For each subfigure in Figure 3.1 we can write an expression which determines the resultant amplitude of the light travelling along the light path. These can be calculated by following the light as it travels through the structure. For instance, for Figure 3.1 (a) we begin by transmitting right circular polarisation through the structurally chiral medium. This transmission is given by t_c, which we have previously calculated. The light then gets reflected at the far boundary, which is given by r_2. This flips the light from right circular polarisation to left circular polarisation, which now must travel through the structurally chiral medium undisturbed until it reaches the initial boundary. The expression for this section is given by e^{ikL}. Finally, the light reflects at the near boundary, which is given by r_1. The expression which determines the amplitude of right circular polarisation propagating through the structurally chiral medium and returning as right circular polarisation after

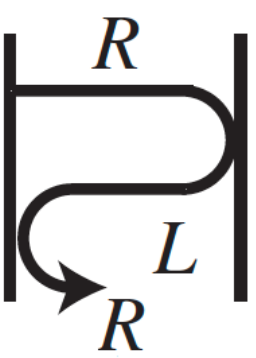

(a) $a_{RR} = e^{ikL} r_1 r_2 t_c$

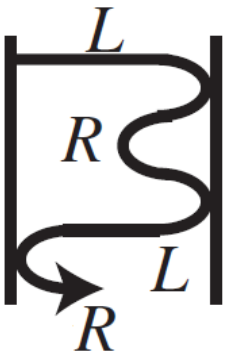

(b) $a_{LR} = e^{2i(k+p)L} r_1 r_2^2 r_c$

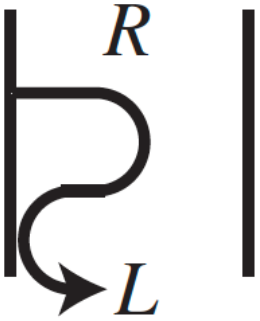

(c) $a_{RL} = r_1 r_c$

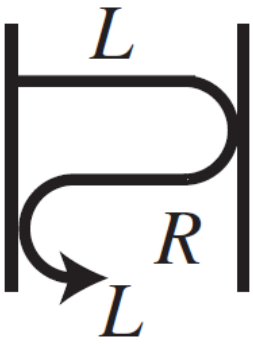

(d) $a_{LL} = e^{ikL} r_1 r_2 t_c$

Figure 3.1: The four possible light paths that can be taken by circularly polarised light completing one round trip in a right handed structurally chiral medium. (a) represents right circular polarisation arriving as right circular polarisation after one round trip, (b) represents left circular polarisation arriving as right circular polarisation, (c) represents right circular polarisation arriving as left circular polarisation and (d) represents left circular polarisation arriving as left circular polarisation. The expressions for the resultant amplitude of the light travelling along the light path is written in the caption of each light path. Reproduced with permission from [2].

one round trip is therefore given as

$$t_c \times r_2 \times e^{ikL} \times r_1 = e^{ikL} r_1 r_2 t_c. \tag{3.65}$$

In a similar fashion the expressions for the other light paths can be calculated. We write these as coefficients a_{LL}, a_{LR}, a_{RL} and a_{RR}. The expressions for these coefficients, written as a matrix, are

$$\begin{pmatrix} a_{RR} & a_{LR} \\ a_{RL} & a_{LL} \end{pmatrix} = \begin{pmatrix} e^{ikL} r_1 r_2 t_c & e^{2i(k+p)L} r_1 r_2^2 r_c \\ r_1 r_c & e^{ikL} r_1 r_2 t_c \end{pmatrix}. \tag{3.66}$$

These can be considered to be the buildings blocks from which all other light paths can

be constructed. They represent the *only* possibilities for pure circularly polarised light to complete a round trip in a structurally chiral medium. Later we shall demonstrate how these can be used to determine the lasing condition of a structurally chiral laser.

We wish to express each of the reflection/transmission coefficients in terms of each other and an extra term, thereby constructing coupled equations [2]. This can be achieved using the four light paths depicted in Figure 3.1. As an example, we consider r_{LL}^{int}, left circular polarisation inside the structurally chiral medium reflected and arriving back at the incident boundary as left circular polarisation (see Figure 3.2).

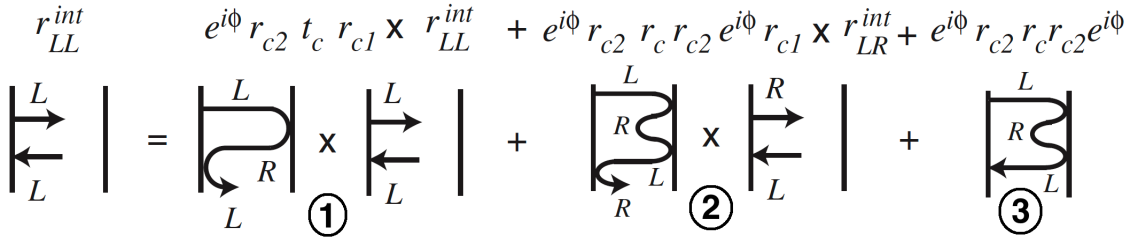

Figure 3.2: All possible paths for left circular polarisation reflecting and returning as left circular polarisation inside the structurally chiral medium. Reproduced with permission from [2].

As left circular polarisation begins travelling inside the structurally chiral medium it initially encounters a homogeneous medium and thus reaches the exit boundary undisturbed. As we know the light arrives back at the incident boundary as left circular polarisation (because we are only considering r_{LL}^{int}, left circular polarisation reflecting as left circular polarisation), it must be reflected at the exit boundary, as otherwise it would escape and not form part of r_{LL}^{int}. This reverses its chirality to right circular polarisation.

Now the right circular polarisation splits into two parts:

The first part is transmitted and reaches the incident boundary as right circular polarisation, where it is reflected and its chirality is reversed to left circular polarisation. We are now back at the incident boundary with left circular polarisation, so we multiply the complex amplitude of this chain of events by r_{LL}^{int}, which symbolises all the possible paths the light ray could now take to arrive back at the boundary as left circular polarisation, which is the initial condition. This is represented by part (1) of Figure 3.2.

The second part is distributively reflected along the length of the structurally chiral

medium and its chirality is preserved. We then have right circular polarisation incident upon the exit boundary where it is reflected. This switches its chirality to left circular polarisation and it travels homogeneously to the incident boundary. Here the light splits into two parts again:

The first part is not reflected at the incident boundary. This is represented by part (3) of Figure 3.2.

The second part is reflected at the boundary and its chirality is reversed to right circular polarisation. The complex amplitude of this chain of events can then be multiplied by r_{RL}^{int}, right circular polarisation inside the structurally chiral medium reflecting and arriving back at the incident boundary as left circular polarisation. This is represented by part (2) of Figure 3.2.

Thus, we have found all possible paths left circular polarisation can take inside the structurally chiral medium to arrive back at the incident boundary as left circular polarisation. Therefore,

$$r_{LL}^{int} = e^{i\phi} r_{c2} t_c r_{c1} \times r_{LL}^{int} + e^{i\phi} r_{c2} r_c r_{c2} e^{i\phi} + e^{i\phi} r_{c2} r_c r_{c2} e^{i\phi} r_{c1} \times r_{RL}^{int} \tag{3.67}$$

where $\phi = \bar{n} k_0 L$ is the phase accumulated by the left circular polarisation as it traverses the medium. Note that the phase delay is only added explicitly when the structurally chiral medium is traversed by left circular polarisation as the phase delay is implicitly incorporated inside the t_c and r_c terms.

Similar logic can be used to calculate the other internal reflectances and transmittances and the remaining diagrams for these can be found in Appendix A. These form four sets of coupled equations that are all solved in a similar way. We shall demonstrate the solution for r_{LL}^{int} and r_{LR}^{int}.

We begin by writing

$$\mathbf{v}_{rL} = \begin{pmatrix} r_{LL}^{int} \\ r_{RL}^{int} \end{pmatrix} = \begin{pmatrix} e^{i\phi} r_{c2} t_c r_{c1} & r_c r_{c2}^2 e^{2i\phi} r_{c1} \\ r_c r_{c1} & t_c r_{c2} e^{i\phi} r_{c1} \end{pmatrix} \begin{pmatrix} r_{LL}^{int} \\ r_{RL}^{int} \end{pmatrix} + \begin{pmatrix} r_c r_{c2}^2 e^{2i\phi} \\ t_c r_{c2} e^{i\phi} \end{pmatrix}. \tag{3.68}$$

We can rewrite

$$\mathbf{v}_{rL} = \underline{N}\mathbf{c}_{rL}, \tag{3.69}$$

where

$$\underline{N} = D^{-1}\begin{pmatrix} 1 - t_c e^{i\phi} r_{c2} r_{c1} & r_c r_{c2}^2 e^{2i\phi} r_{c1} \\ r_c r_{c1} & 1 - t_c r_{c2} e^{i\phi} r_{c1} \end{pmatrix}, \tag{3.70}$$

$$\mathbf{c}_{rL} = \begin{pmatrix} r_c r_{c2}^2 e^{2i\phi} \\ t_c r_{c2} e^{i\phi} \end{pmatrix}, \tag{3.71}$$

$$D = \left(1 - e^{i\phi} r_{c2} t_c r_{c1}\right)^2 - \left(e^{i\phi} r_c r_{c2} r_{c1}\right)^2. \tag{3.72}$$

The other reflectances and transmittances can be solved by replacing $\mathbf{v}_{rL}$ and $\mathbf{c}_{rL}$ in Equation (3.69) and keeping N the same. We find that

$$\mathbf{v}_{rR} = \begin{pmatrix} r_{LR}^{int} \\ r_{RR}^{int} \end{pmatrix} \implies \mathbf{c}_{rR} = \begin{pmatrix} e^{i\phi} r_{c2} t_c \\ r_c \end{pmatrix}, \tag{3.73}$$

$$\mathbf{v}_{tL} = \begin{pmatrix} t_{LL}^{int} \\ t_{RL}^{int} \end{pmatrix} \implies \mathbf{c}_{tL} = \begin{pmatrix} e^{i\phi} \\ 0 \end{pmatrix}, \tag{3.74}$$

$$\mathbf{v}_{tR} = \begin{pmatrix} t_{LR}^{int} \\ t_{RR}^{int} \end{pmatrix} \implies \mathbf{c}_{tR} = \begin{pmatrix} e^{i\phi} r_{c2} r_c \\ t_c \end{pmatrix}. \tag{3.75}$$

We have now established equations for the *internal* reflectances and transmittances.

We are left with finding the *resultant* reflection/transmission coefficients. This is done by simply multiplying the *internal* reflectances and transmittances by the *interface* transmit-

tances at the two boundaries. We thus have

$$r_{LL} = t_{1c} r_{LL}^{int} t_{c1} = t_{1c} D^{-1} r_c r_{c2}^2 e^{2i\phi} t_{c1}, \tag{3.76}$$

$$r_{LR} = r_{1c} + D^{-1} t_{1c} \left[t_c r_{c2} e^{i\phi} + r_{c1} r_{c2}^2 e^{2i\phi} \left(r_c^2 - t_c^2 \right) \right] t_{c1} = r_{RL}, \tag{3.77}$$

$$r_{RR} = D^{-1} t_{1c} r_c t_{c1}, \tag{3.78}$$

$$t_{LL} = D^{-1} t_{1c} \left(1 - t_c e^{i\phi} r_{c2} r_{c1} \right) e^{i\phi} t_{c2}, \tag{3.79}$$

$$t_{LR} = D^{-1} t_{1c} r_c r_{c1} e^{i\phi} t_{c2} = \left(\frac{r_{c1}}{r_{c2}} \right) t_{RL}, \tag{3.80}$$

$$t_{RR} = D^{-1} t_{1c} \left[t_c + r_{c1} e^{i\phi} r_{c2} \left(r_c^2 - t_c^2 \right) \right] t_{c2}. \tag{3.81}$$

Equations (3.76) - (3.81) are the key results of the coupled wave theory approximation for structurally chiral media.

3.4 Comparison to the Oseen Method

Having conducted our calculations using coupled wave theory we are interested in the accuracy of the theory when applied to structurally chiral media, for which we need to compare the reflectances and transmissions derived in Section 3.3 to the analytic reflection/transmission coefficients calculated using the Oseen method [70].

For the Oseen method we translate the problem into a rotating frame, which rotates with the period of the principal axes of birefringence as we propagate into the structurally chiral medium. To do this we introduce two new fields, $\boldsymbol{e}$ and $\boldsymbol{h}$, where

$$\boldsymbol{e} = \underline{\mathrm{R}}_{\perp}^{-1} \mathbf{E}_{\perp}, \tag{3.82}$$

$$\boldsymbol{h} = \underline{\mathrm{R}}_{\perp}^{-1} \mathbf{H}_{\perp}. \tag{3.83}$$

Equation (3.22) can then be rewritten as

$$\frac{\mathrm{d}}{\mathrm{d}z} \mathbf{f} = i \underline{\tilde{\mathrm{G}}} \mathbf{f}, \tag{3.84}$$

where $\mathbf{f} = \begin{bmatrix} e_x & e_y & h_x & h_y \end{bmatrix}^T$ and

$$\underline{\tilde{\mathrm{G}}} = \begin{bmatrix} 0 & -ip & 0 & \omega\mu_0 \\ ip & 0 & -\omega\mu_0 & 0 \\ 0 & -\omega\varepsilon_0\varepsilon_c & 0 & -ip \\ \omega\varepsilon_0\varepsilon_d & 0 & ip & 0 \end{bmatrix}. \tag{3.85}$$

As $\underline{\tilde{\mathrm{G}}}$ does not depend on z, Equation (3.25) holds and we can easily solve Equation (3.84) using Equations (3.24) and (3.25). We find that if $\mathbf{f}|_z = \underline{\mathrm{M}}'\mathbf{f}|_0$, then

$$\underline{\mathrm{M}}' = \exp\left\{ i \int_0^z \underline{\tilde{\mathrm{G}}} \mathrm{d}z \right\} = \exp\left\{ iz\underline{\tilde{\mathrm{G}}} \right\}. \tag{3.86}$$

$\underline{\mathrm{M}}$ in Equation (3.24) is given by

$$\underline{\mathrm{M}} = \begin{bmatrix} \underline{\mathrm{R}}_\perp & \underline{\mathbf{0}} \\ \underline{\mathbf{0}} & \underline{\mathrm{R}}_\perp \end{bmatrix} \underline{\mathrm{M}}' = \begin{bmatrix} \underline{\mathrm{R}}_\perp & \underline{\mathbf{0}} \\ \underline{\mathbf{0}} & \underline{\mathrm{R}}_\perp \end{bmatrix} \exp\left\{ iz\underline{\tilde{G}} \right\}, \tag{3.87}$$

where $\underline{\mathbf{0}}$ is the 2×2 null matrix.

This analytic solution allows for a quick and efficient way of solving for $\mathbf{E}$ and $\mathbf{H}$. However, we are ultimately interested in better understanding the reflectance and transmittance of the structure. The Oseen transformation supplies analytical equations for these, but the equations are very long and not particularly insightful.

Having established the exact solution for $\mathbf{E}$ and $\mathbf{H}$ using the Oseen method, let us now take the surrounding medium into account. For an embedded structurally chiral medium, field matching requires that

$$\mathrm{F}|_0 = \begin{pmatrix} a_x + r_x \\ a_y + r_y \\ -\bar{n}\left(a_y - r_y\right)/\eta_0 \\ \bar{n}\left(a_x - r_x\right)/\eta_0 \end{pmatrix} \text{ and } \mathrm{F}|_L = \begin{pmatrix} t_x \\ t_y \\ -\bar{n}t_y/\eta_0 \\ \bar{n}t_x/\eta_0 \end{pmatrix}, \tag{3.88}$$

where η_0 is the impedance of free space, $\bar{n}$ is the average refractive index of the structurally

chiral medium, a is the incident amplitude of the field, r is the reflected amplitude of the field and t is the amplitude of the field transmitted through the structurally chiral medium. The suffixes denote the x or y components of the vectors.

We assume the incident amplitude is known, which leaves four unknown variables: r_x, r_y, t_x and t_y. We can use the four simultaneous equations that arise from inserting $\mathrm{F}|_0$ and $\mathrm{F}|_L$ from Equation (3.88) into Equation (3.24) with $\underline{\mathrm{M}}$ from Equation (3.87) to solve for the four unknowns r_x, r_y, t_x and t_y in terms of a_x and a_y. We can write the relation between the unknowns r and t with a as

$$\begin{pmatrix} r_x \\ r_y \end{pmatrix} = \begin{pmatrix} r_{xx} & r_{xy} \\ r_{yx} & r_{yy} \end{pmatrix} \begin{pmatrix} a_x \\ a_y \end{pmatrix}, \tag{3.89}$$

$$\begin{pmatrix} t_x \\ t_y \end{pmatrix} = \begin{pmatrix} t_{xx} & t_{xy} \\ t_{yx} & t_{yy} \end{pmatrix} \begin{pmatrix} a_x \\ a_y \end{pmatrix}. \tag{3.90}$$

The entries in the transformation matrices can be physically interpreted. For instance, t_{yx} represents the complex amplitude of x polarised light that gets transmitted as y polarised light.

As we are analysing structurally chiral media we would like to express the amplitudes in a circular basis. We switch from the Cartesian basis to a circular basis using

$$\begin{pmatrix} r_x \\ r_y \end{pmatrix} = \frac{1}{\sqrt{2}} \begin{pmatrix} 1 & 1 \\ -i & i \end{pmatrix} \begin{pmatrix} r_L \\ r_R \end{pmatrix}, \tag{3.91}$$

$$\begin{pmatrix} a_x \\ a_y \end{pmatrix} = \frac{1}{\sqrt{2}} \begin{pmatrix} 1 & 1 \\ i & -i \end{pmatrix} \begin{pmatrix} a_L \\ a_R \end{pmatrix}, \tag{3.92}$$

$$\begin{pmatrix} t_x \\ t_y \end{pmatrix} = \frac{1}{\sqrt{2}} \begin{pmatrix} 1 & 1 \\ i & -i \end{pmatrix} \begin{pmatrix} t_L \\ t_R \end{pmatrix}. \tag{3.93}$$

Combining Equations (3.89)-(3.93), we find that

$$\begin{pmatrix} r_L \\ r_R \end{pmatrix} = \begin{pmatrix} r_{LL} & r_{LR} \\ r_{RL} & r_{RR} \end{pmatrix} \begin{pmatrix} a_L \\ a_R \end{pmatrix}, \tag{3.94}$$

$$\begin{pmatrix} t_L \\ t_R \end{pmatrix} = \begin{pmatrix} t_{LL} & t_{LR} \\ t_{RL} & t_{RR} \end{pmatrix} \begin{pmatrix} a_L \\ a_R \end{pmatrix}, \tag{3.95}$$

where

$$\begin{pmatrix} r_{LL} & r_{LR} \\ r_{RL} & r_{RR} \end{pmatrix} = \frac{1}{2} \begin{pmatrix} 1 & i \\ 1 & -i \end{pmatrix} \begin{pmatrix} r_{xx} & r_{xy} \\ r_{yx} & r_{yy} \end{pmatrix} \begin{pmatrix} 1 & 1 \\ i & -i \end{pmatrix}, \tag{3.96}$$

$$\begin{pmatrix} t_{LL} & t_{LR} \\ t_{RL} & t_{RR} \end{pmatrix} = \frac{1}{2} \begin{pmatrix} 1 & -i \\ 1 & i \end{pmatrix} \begin{pmatrix} t_{xx} & t_{xy} \\ t_{yx} & t_{yy} \end{pmatrix} \begin{pmatrix} 1 & 1 \\ i & -i \end{pmatrix}. \tag{3.97}$$

Given the amplitude and angle of incidence of the electromagnetic wave incident upon the structurally chiral medium we can use Equation (3.24) in conjunction with the discussion above to calculate an analytic solution for the eight circular reflection and transmittance coefficients. We can thus construct an analytic solution for the reflectances and transmittances when provided with the structure of the structurally chiral medium and the nature of the electromagnetic wave incident upon it.

However, while the solutions will be analytic, the individual equations for the reflectances and transmittances are extremely cumbersome to use due to their complexity. We shall now show that the approximate equations for the reflectances and transmittances provided by coupled wave theory agree with those derived using the Oseen method and can therefore be used to easily make predictions about structurally chiral media.

We compare the reflected and transmitted intensities of the analytic Oseen solution to the coupled wave theory approximation to determine the accuracy of the approximation. We

begin by stating that the intensities are

$$\begin{pmatrix} R_{LL} & R_{LR} \\ R_{RL} & R_{RR} \end{pmatrix} = \begin{pmatrix} |r_{LL}|^2 & |r_{LR}|^2 \\ |r_{RL}|^2 & |r_{RR}|^2 \end{pmatrix}, \tag{3.98}$$

$$\begin{pmatrix} T_{LL} & T_{LR} \\ T_{RL} & T_{RR} \end{pmatrix} = \left(\frac{n_2}{n_1}\right) \begin{pmatrix} |t_{LL}|^2 & |t_{LR}|^2 \\ |t_{RL}|^2 & |t_{RR}|^2 \end{pmatrix}. \tag{3.99}$$

The factor n_2/n_1 is introduced in Equation (3.99) in order to conserve the power in the system.

With the initial variables defined in Table 3.1, chosen to reflect a typical structurally chiral medium, we can calculate the reflectances and transmittances over a range of wavelengths. We find the Bragg wavelength as

$$\lambda_0^{Bragg} = \mathrm{Re}\,(\bar{n})\, L_p = 519\mathrm{nm} \tag{3.100}$$

and the bandwidth as

$$\Delta\lambda_0 = 2\mathrm{Re}\,(\delta n)\, L_p = 16\mathrm{nm}. \tag{3.101}$$

Structural period	$L_p = 300$ nm
Principal dielectric constants	$\epsilon_a = 3.2 + 0.02i$
	$\epsilon_b = 2.9 + 0.02i$
	$\epsilon_c = 2.8 + 0.02i$
Rise angle	$\theta = 30°$
Depth of chiral medium	$L = 6\,\mu$m
Refractive index of incident medium	$n_1 = 1$
Refractive index of transmission medium	$n_2 = 2$

Table 3.1: Data used for calculations.

Figures 3.3a and 3.3b demonstrate that the differences between coupled wave theory and the analytic Oseen solution for this prototypical example of a structurally chiral medium are so small as to provide visually identical graphs. In addition, the consistency checks that ensure conservation of energy from right circular polarisation to left circular polarisation and vice versa hold.

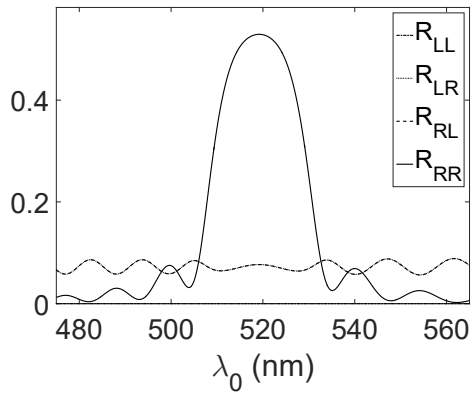

(a) Reflections as calculated using coupled wave theory. The graph is visually identical to the analytic solution.

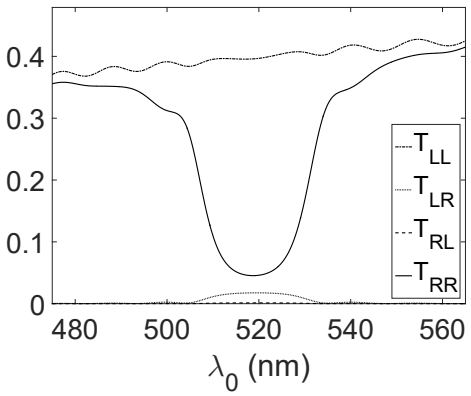

(b) Transmissions as calculated using coupled wave theory. The graph is visually identical to the analytic solution.

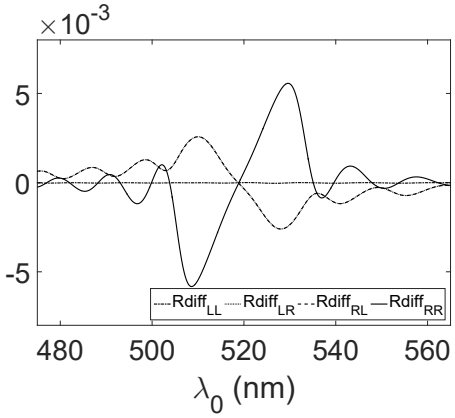

(c) The difference between the reflections calculated by coupled wave theory and those calculated analytically.

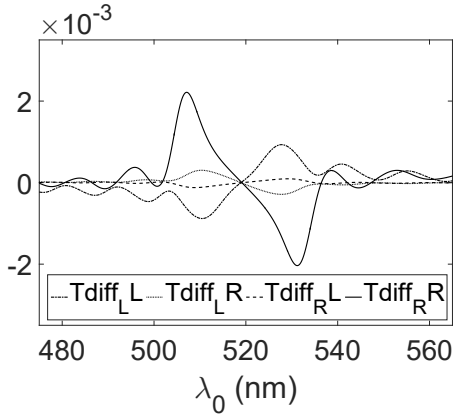

(d) The difference between the transmissions calculated by coupled wave theory and those calculated analytically.

Figure 3.3: Key graphs demonstrating the accuracy of coupled wave theory and confirming its validity for the analysis of structurally chiral media. Made using code from [2].

Examining Figures 3.3c and 3.3d one can see that the discrepancies between the two methods are very small. R_{RR} has the largest discrepancy, which nevertheless remains below 0.6%. On average the discrepancy is around 10^{-3}% and with increasing absorption the discrepancy decreases further. The crucial assumption made in the coupled wave theory approximation was that $|\delta n| \ll \bar{n}$, so one would predict that an increase in birefringence would increase the discrepancy, which is indeed the case.

The graphs seen in Figure 3.3 are for a structurally chiral medium with an incident medium and an exit medium. We can match the refractive indices of these to the structurally chiral medium by setting $n_1 = \bar{n} = n_2$ to filter out the effect of the surrounding media and view

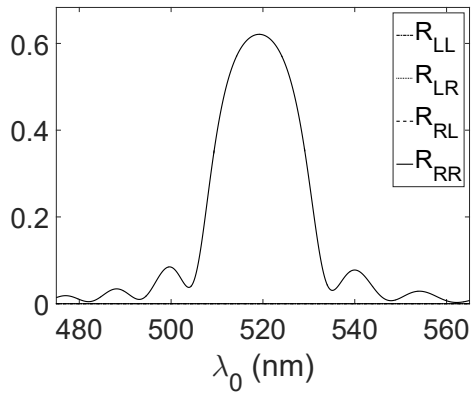

(a) Index matched reflectances as calculated using coupled wave theory. The graph is visually identical to the analytic solution.

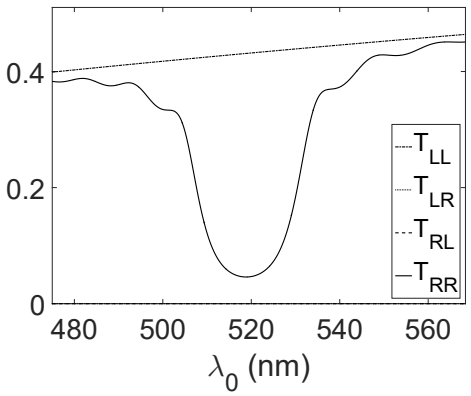

(b) Index matched transmittances as calculated using coupled wave theory. The graph is visually identical to the analytic solution.

Figure 3.4: Graphs demonstrating the index matched reflectances and transmittances of the structurally chiral medium. Made using code from [2].

the effect of the structurally chiral medium only. The results are demonstrated in Figure 3.4.

When index matching, coupled wave theory suggests that any left circular polarisation passing through the structurally chiral medium sees a homogeneous medium of refractive index $\bar{n}$ and therefore index matching should set both R_{RL} and $R_{LL}$to zero. As there are no reflections due to a sudden change in the refractive index at the boundaries there will be no chirality reversing effects. Thus all transmittances and reflectances that refer to a change in chirality will also be zero.

Comparing graphs 3.3a and 3.3b to 3.4a and 3.4b we note that the reflectances have all vanished except for R_{RR}, as we would expect from the coupled wave theory analysis. Further, we notice that $T_{RL} = T_{LR} = 0$ and that the only transmittance demonstrating an interesting pattern is T_{RR}, again as predicted. The reason for $T_{LL} \neq 1$ is the loss built into the structure due to the complex nature of the permittivities ϵ_a, ϵ_b and ϵ_c.

While we have only shown the results for one particular set of initial values given by Table 3.1, the low discrepancy between the analytic Oseen solution and the coupled wave theory approximation holds true for a wide range of initial values, as long as $|\delta n| \ll \bar{n}$. We have thus demonstrated that the coupled wave theory approximation is very close to the analytic solution. With an average discrepancy of around $10^{-3}\%$ we can rely on it to help

gain a deeper understanding of structurally chiral media.

We continue by examining Equations (3.76) - (3.81) in search of significant special cases. It is clear from Equation (3.80) that if the incident medium has a different refractive index than the exit medium, then the contra-handed transmittances will not equate ($t_{RL} \neq t_{LR}$). Examining Equation (3.78) we see that the only way to keep right circular polarisation from reflecting back right circular polarisation is by either setting $D = 0$ or by turning the chirality of the structurally chiral medium off, thereby setting $r_c = 0$. In fact, it turns out that D is an important parameter. Setting $D = 0$ in the presence of gain is connected to the lasing condition for a structurally chiral laser, which we will explore in Chapter 5.

There are many other conditions that can be exploited to manipulate individual transmissions and reflections. Being able to explore these possibilities more easily than with the analytic Oseen solution is one of the key benefits of coupled wave theory analysis and will be relied upon extensively in the following chapters.

Chapter 4

Scalar Distributed Feedback Lasers

4.1 Introduction to Scalar Distributed Feedback Lasers

Having established a strong theoretical foundation from first principles for structurally chiral media we could now develop the theory behind structurally chiral lasers. However, before doing so it will prove instructive to develop a simpler laser first. A scalar distributed feedback laser uses a Bragg grating to lase and has no inbuilt polarisation dependence.

Like the structurally chiral laser, the scalar distributed feedback laser is a type of distributed feedback laser. Both lasers rely on a Bragg like reflection phenomenon to provide the necessary photon dwell time to achieve lasing. Distributed feedback lasers are mirrorless lasers, although sometimes mirrors are added to improve efficiency. It shall become clear that the scalar distributed feedback laser is the simpler, scalar counterpart to the polarisation dependent structurally chiral laser. A comparison between the two will serve as an excellent tool to highlight the novel features found in structurally chiral lasers, which have been unearthed by our research.

4.2 Coupled Wave Theory of Bragg Gratings

A scalar distributed feedback laser consists of a material with periodically changing refractive index, commonly referred to as a Bragg grating (see Figure 4.1). The material is then doped to produce a scalar distributed feedback laser. To understand the structure of a scalar distributed feedback laser we shall first analyse a Bragg grating with no gain. Only after we have noted the differences between Bragg gratings and structurally chiral media we introduce gain into both and discuss the differences between the scalar distributed feedback laser and the structurally chiral laser.

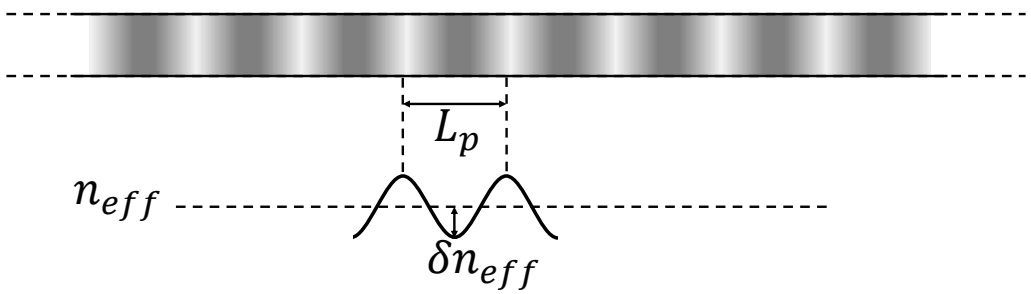

Figure 4.1: Schematic diagram of a Bragg grating with a sinusoidal refractive index modulation δn_{eff}, represented by the greyscale gradient. The high refractive index is represented by white and the low refractive index by dark grey. The pitch of the Bragg grating is L_p.

The reflectances of a Bragg grating are calculated in a very similar manner to those of a structurally chiral medium already discussed in Chapter 3. The key difference is that we no longer need to differentiate between different polarisation states of light. All light is reflected in an identical manner. This will simplify the calculations, as we shall now demonstrate.

The initial problem statement is identical to that already outlined in Section 3.2. The reflections and transmissions of a Bragg grating can therefore also be calculated using coupled wave theory.

The key difference is that the polarisation state of $\mathbf{E}_\perp$ will not change as it passes through the Bragg grating. This allows for a choice of basis $\{x', y'\}$ for which the polarisation state

of $\mathbf{E}_\perp$ is such that

$$\mathbf{E}_\perp = \begin{pmatrix} E_{x'} \\ 0 \end{pmatrix} \tag{4.1}$$

throughout. This choice of basis reduces the complexity of the problem by one degree of freedom, as we can now consider only $E_{x'}$.

The rest of the analysis follows a similar path to Section 3.3. We postulate both a forward and a backward propagating component of $E_{x'}$ and write

$$E_{x'} = A^+(z)\exp\{ikz\} + A^-(z)\exp\{-ikz\}. \tag{4.2}$$

Inserting Equation (4.2) into the x-component of the Helmholtz equation (3.31) and following the same steps as outlined in Section 3.3 we arrive at

$$\frac{\mathrm{d}}{\mathrm{d}z}\begin{pmatrix} A^+(z) \\ A^-(z) \end{pmatrix} = i\kappa \begin{pmatrix} 0 & e^{-i\delta kz} \\ -e^{i\delta kz} & 0 \end{pmatrix}\begin{pmatrix} A^+ \\ A^- \end{pmatrix}. \tag{4.3}$$

Comparing Equation (4.3) to Equations (3.49) and (3.50) we notice first that Equations (4.3) and (3.50) are identical. Thus right circular polarisation in a right-handed structurally chiral medium behaves in the same way as all light behaves passing through a Bragg grating.

We continue the analysis of the Bragg grating by solving the coupled wave theory equations in the same way we solved Equation (3.50). We find that for $0 < z < L$

$$\begin{bmatrix} E^+(z) \\ E^-(z) \end{bmatrix} = \begin{pmatrix} P^+(z) & Q^+(z) \\ Q^-(z) & P^-(z) \end{pmatrix}\begin{bmatrix} E^+(0^+) \\ E^-(0^+) \end{bmatrix}, \tag{4.4}$$

where

$$E^\pm(z) = A^\pm e^{\pm ikz}, \tag{4.5}$$

$$P^\pm(z) = e^{\pm ipz}\left[\cosh(\Delta z) \pm i\frac{\delta k}{2\Delta}\sinh(\Delta z)\right], \tag{4.6}$$

$$Q^\pm(z) = \pm\frac{ie^{\pm ipz}\kappa}{\Delta}\sinh(\Delta z). \tag{4.7}$$

Notice that a factor of a half is introduced when compared to Equations (3.53)-(3.55) intrinsically in the definition of L_p, because a Bragg grating needs a full period to reach the initial refractive index value whereas a structurally chiral medium only needs half a period and therefore has a refractive index modulation that is twice as fast with respect to z.

We can use Equations (4.4) - (4.7) to find that

$$R' = |r'|^2 = \left| -\frac{Q^-(L)}{P^-(L)} \right|^2 = \left| \frac{\kappa \sinh(\Delta L)}{\Delta \cosh(\Delta L) + i(\delta k/2)\sinh(\Delta L)} \right|^2 \tag{4.8}$$

and

$$T' = |t'|^2 = \left| \frac{1}{P^-(L)} \right|^2 = \left| \cosh(\Delta L) - i\frac{\delta k}{2\Delta}\sinh(\Delta L) \right|^{-2}. \tag{4.9}$$

This concludes the coupled wave theory analysis of Bragg gratings. Comparing Equations (4.8)-(4.9) to Equations (3.60)-(3.59) shows that electromagnetic waves travelling through the two structures react in a very similar manner. However, there are some crucial differences to be highlighted.

The most straightforward of these differences is the fact that the refractive index of a structurally chiral medium repeats itself after half a turn while the refractive index of a Bragg grating repeats itself after a full turn.

Next, consider an index matched Bragg grating and structurally chiral medium. Let an arbitrarily polarised electromagnetic wave enter the Bragg grating. As there is no discrimination between different polarisation states the wave will reflect and transmit as specified by Equations (4.8) and (4.9). The same wave entering a right handed structurally chiral medium will be affected very differently. The initial polarisation state can be split into right circular polarisation and left circular polarisation. Right circular polarisation will be affected in an identical manner to the total wave travelling through the Bragg grating (assuming the period of the Bragg grating is twice the period of the structurally chiral medium). The crucial point is that left circular polarisation will be entirely unaffected by the structurally chiral medium. The component of the electromagnetic wave transmitted

through the structure will therefore consist of all left circular polarisation of the initial wave and whichever component of right circular polarisation gets transmitted, specified by t_c. This will change the polarisation state of the transmitted wave. Following the same logic, the reflected electromagnetic wave will consist only of the reflected part of right circular polarisation of the incident wave, specified by r_c. Thus a structurally chiral medium changes the polarisation while a Bragg grating does not and the total transmitted and reflected intensities differ as well.

There is an interesting special case, where an electromagnetic wave passing through an index matched Bragg grating is reflected and transmitted in exactly the same way as if it passed through an index matched right handed structurally chiral medium (with half the period of the Bragg grating). This occurs when the incident electromagnetic wave is pure right circular polarisation.

Note the emphasis on index matching. Once the structure is not index matched the reflections at the boundary will change the polarisation of the reflected right circular polarisation to left circular polarisation. This will introduce left circular polarisation and the polarisation of the reflected light in the structurally chiral medium will differ from that in the Bragg grating. However, if the Bragg grating and structurally chiral medium are index matched they represent completely identical structures to right circular polarisation travelling through them.

We shall demonstrate later that it is not possible to maintain this identity when gain is introduced to produce a scalar distributed feedback laser and a structurally chiral laser. This stems from the fact that the complex refractive index of the active gain medium necessitated by the introduction of gain cannot be index matched to the surrounding media, which is devoid of gain. Thus the *only* time that Bragg gratings and structurally chiral medium are identical is in an index matched case for right circular polarisation. Scalar distributed feedback lasers and structurally chiral lasers can *never* be identical.

The challenge encountered when analysing a structurally chiral laser as opposed to a scalar distributed feedback laser is considering the effect of the left circular polarisation component of the electromagnetic wave traveling through the structure and understanding

how it induces a more complex structure for a structurally chiral laser, not present in a scalar distributed feedback laser.

4.3 Lasing Condition for Scalar Distributed Feedback Lasers

In order to model a scalar distributed feedback laser and calculate its lasing condition we introduce gain α into a Bragg grating. Such an introduction comes most naturally by allowing complex permittivities ε_a, ε_b and ε_c where a positive complex component models gain. If we now consider the complex nature of $\bar{n}$:

$$\varepsilon_j \to \varepsilon_j + i\alpha \implies \bar{n} \to \bar{n}_r + i\bar{n}_i. \tag{4.10}$$

While negative permittivity values in materials such as metals can also lead to a complex refractive index, in our model the real part of the permittivities remain positive and it is specifically the imaginary component of the permittivity that complexifies the refractive index. Note that as $\bar{n}$ is the root of the average permittivity, letting α vary leads to a variation in both the real and imaginary part of $\bar{n}$.

The rest of the calculations in Sections 3.3 and 4.2 remain valid, simply by replacing the real $\bar{n}$ with its complex equivalent from Expression (4.10). As many of the intermediate parameters in the calculations depend on $\bar{n}$ the gain is thus implicitly introduced into the whole analysis.

For lasing in an index-matched scalar distributed feedback laser we need $r' = \infty$ [71], which implies that

$$\boxed{\Delta \cosh(\Delta L) = -i\frac{\delta k}{2}\sinh(\Delta L)} \tag{4.11}$$

from Equation (4.8). Equation (4.11) is thus the lasing condition for an index-matched scalar distributed feedback laser.

An examination of Equation (4.11) demonstrates that a complexification of $\bar{n}$ as above

with $\alpha > 0$ is necessary for solutions to exist. Considering

$$\begin{aligned} E(\boldsymbol{r}) &= E(z)\exp\{-ikz\} && (4.12)\\ &= E(z)\exp\{-i(\bar{n}_r + i\bar{n}_i)k_0 z\} && (4.13)\\ &= E(z)\exp\{-i\bar{n}_r k_0 z\}\cdot\exp\{\bar{n}_i k_0 z\} && (4.14)\end{aligned}$$

we see that $\alpha > 0$ corresponds to gain in the medium, thereby demonstrating that gain is necessary for the lasing condition to hold, as expected.

For the non-index-matched scalar distributed feedback laser the lasing condition is more complex. We consider Equation (4.4) and impose the boundary conditions

$$\begin{aligned} E^+(0) &= r_1 E^-(0), && (4.15)\\ E^-(L) &= r_2 E^+(L), && (4.16)\end{aligned}$$

where $r_1 = r_{c1}$ and $r_2 = r_{c2}$ are the Fresnel reflection coefficients defined in Equations (3.61) and (3.62) and we drop the superscript on 0. These boundary conditions impose that the electric field travelling inside the Bragg grating and hitting the boundary between the Bragg grating and the incident medium gets partially reflected, with the reflected component having its chirality reversed. They further impose that there is no external field entering the Bragg grating. This second imposition is crucial for a laser, as one way of expressing the lasing condition is by requiring the generation of a field without any external input.

We can now solve Equation (4.4) using the boundary conditions:

$$\begin{bmatrix} E^+(L) \\ E^-(L) \end{bmatrix} = \begin{bmatrix} E^+(L) \\ r_2 E^+(L) \end{bmatrix} = \begin{pmatrix} P^+(L) & Q^+(L) \\ Q^-(L) & P^-(L) \end{pmatrix} \begin{bmatrix} r_1 E^-(0) \\ E^-(0) \end{bmatrix} \tag{4.17}$$

implying that

$$\left[P^-(L) + r_1 Q^-(L) - r_2 Q^+(L) - r_1 r_2 P^+(L)\right] E^-(0) = 0. \tag{4.18}$$

Equation (4.18) trivially holds when $E^{-}(0) = 0$. For a laser we are interested in the case when Equation (4.18) holds and $E^{-}(0) \neq 0$. This produces a finite output (see the boundary conditions given by Equations (4.15) and (4.16)) without any external input. The only way this can occur is when

$$\boxed{P^{-}(L) + r_1 Q^{-}(L) - r_2 Q^{+}(L) - r_1 r_2 P^{+}(L) = 0} \tag{4.19}$$

which is the lasing condition for a non-index-matched scalar distributed feedback laser, not seen in existing literature.

We plot the lasing modes of a non-index-matched scalar distributed feedback laser as a surface plot and a contour plot in Figure 4.2 on the left, with the lasing modes of an index-matched scalar distributed feedback laser as previously reported by Kogelnik and Shank [3] on the right for comparison.

Notice that in the absence of boundary reflections ($r_1 = r_2 = 0$) the lasing condition for an scalar distributed feedback laser becomes

$$\boxed{P^{-}(L) = 0} \tag{4.20}$$

which agrees with the index matched lasing condition given by Equation (4.11). The respective lasing mode surface and contour plot is on the right side of Equation 4.2.

Comparing the figures for the index matched scalar distributed feedback laser to the non index matched scalar distributed feedback laser in Figure 4.2 we see that a new lasing mode appears in the plotted detuning range and that the lasing modes have shifted in general on the detuning versus threshold gain plot.

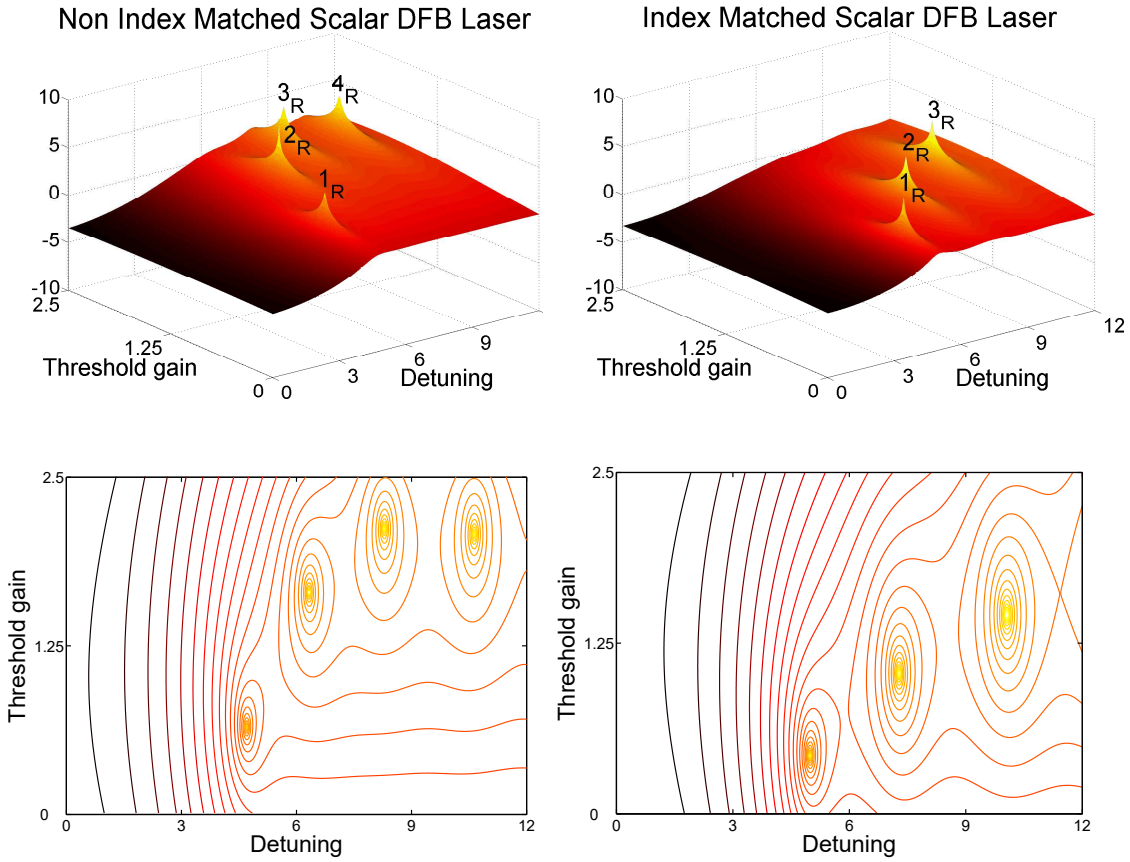

Figure 4.2: Surface (top) and contour (bottom) plots of a non index-matched scalar distributed feedback laser on the left and of an index-matched scalar distributed feedback laser on the right. Notice the extra lasing mode of the non index-matched scalar distributed feedback laser.

Chapter 5

Structurally Chiral Lasers

5.1 Introduction to Structurally Chiral Lasers

With the results from Chapter 3 we can follow the same path set out in Chapter 4 to derive a lasing condition for a structurally chiral laser. We compare the calculated results to the scalar distributed feedback laser in order to highlight the similarities as well as the key differences between the two distributed feedback lasers.

The development of the lasing condition for a structurally chiral laser and the subsequent analysis of the lasing modes presented here uncovers an intriguing coupling between two separate lasing mechanisms. The coupling produces lasing modes of the opposite chirality to the structurally chiral laser, thereby complicating the mode structure significantly. A new class of lasing modes is discovered, which allow a structurally chiral laser with a right-handed structurally chiral medium to lase left circular polarisation. Suggested exploitations of this observation conclude this chapter.

5.2 Lasing Condition for Structurally Chiral Lasers

Just as a scalar distributed feedback laser uses a Bragg grating as its active medium to achieve lasing, a structurally chiral laser uses a structurally chiral medium as its active

medium. As done for the scalar distributed feedback laser, a model for the structurally chiral laser is constructed using exactly the same equations as used for a structurally chiral medium by adding a positive imaginary component to the permittivity. The schematic diagram for a structurally chiral laser is therefore identical to that of a structurally chiral medium with $\bar{n}$ now being complex, which we showed in Figure 2.1.

In a similar vein to Section (4.3) we write

$$\varepsilon_j \to \varepsilon_j + i\alpha \implies \bar{n} \to \bar{n}_r + i\bar{n}_i \tag{5.1}$$

with $\alpha > 0$. This is a simple way to model gain, where we assume that the gain is uniform with regard to wavelength. While this is unlikely to be the case, as gain media have wavelength specific gain profiles (and other complexities), it serves as a simple and effective model from which extrapolations can later be made. In order to impose a wavelength dependent gain spectrum, α would have to be wavelength dependent. Note that α represents the net gain, which subtracts from the total gain any losses due to scattering, absorption, etc. Clearly this model would have to be refined when modelling a particular structurally chiral laser, but for our analysis it provides a useful indication of the lasing properties of a structurally chiral laser.

To develop the lasing theory of structurally chiral lasers we reproduce Equation (3.51), which provides a relationship between the electric field at $z = 0^+$ and $z = L^-$ (so just inside the structurally chiral medium):

$$\begin{bmatrix} E_R^+(L^-) \\ E_R^-(L^-) \\ E_L^+(L^-) \\ E_L^-(L^-) \end{bmatrix} = \begin{pmatrix} P^+(L^-) & Q^+(L^-) & 0 & 0 \\ Q^-(L^-) & P^-(L^-) & 0 & 0 \\ 0 & 0 & e^{ikL^-} & 0 \\ 0 & 0 & 0 & e^{-ikL^-} \end{pmatrix} \begin{bmatrix} E_R^+(0^+) \\ E_R^-(0^+) \\ E_L^+(0^+) \\ E_L^-(0^+) \end{bmatrix}. \tag{5.2}$$

We drop the superscripts and impose the boundary conditions

$$E_L^+(0) = r_1 E_R^-(0), \tag{5.3}$$

$$E_L^-(L) = r_2 E_R^+(L), \tag{5.4}$$

$$E_R^+(0) = r_1 E_L^-(0), \tag{5.5}$$

$$E_R^-(L) = r_2 E_L^+(L). \tag{5.6}$$

These boundary conditions impose that the electric field travelling inside the structurally chiral laser and hitting the boundary between the structurally chiral laser and the incident medium gets partially reflected, with the reflected component having its chirality reversed. They further impose that there is no external field entering the structurally chiral laser, which ensures the generation of a field without any external input when $E_L^+(0) \neq 0$ and $E_R^+(0) \neq 0$.

Using the boundary conditions we can rewrite Equation (5.2) in terms of the four variables $E_R^+(L)$, $E_L^+(L)$, $E_R^-(0)$ and $E_L^-(0)$ as

$$\begin{bmatrix} E_R^+(L) \\ r_2 E_L^+(L) \\ E_L^+(L) \\ r_2 E_R^+(L) \end{bmatrix} = \begin{pmatrix} P^+(L) & Q^+(L) & 0 & 0 \\ Q^-(L) & P^-(L) & 0 & 0 \\ 0 & 0 & e^{ikL} & 0 \\ 0 & 0 & 0 & e^{-ikL} \end{pmatrix} \begin{bmatrix} r_1 E_L^-(0) \\ E_R^-(0) \\ r_1 E_R^-(0) \\ E_L^-(0) \end{bmatrix}. \tag{5.7}$$

We use the bottom two equations

$$E_L^+(L) = e^{ikL} r_1 E_R^-(0), \tag{5.8}$$

$$r_2 E_R^+(L) = e^{-ikL} E_L^-(0), \tag{5.9}$$

to simplify Equation (5.7) to

$$\begin{bmatrix} e^{-ikL} E_L^-(0) \\ e^{ikL} r_1 r_2 E_R^-(0) \end{bmatrix} = \begin{pmatrix} r_2 P^+(L) & r_2 Q^+(L) \\ Q^-(L) & P^-(L) \end{pmatrix} \begin{bmatrix} r_1 E_L^-(0) \\ E_R^-(0) \end{bmatrix}. \tag{5.10}$$

We can rearrange Equation (5.10) to find that

$$\begin{aligned}
\mathbf{0} &= \begin{pmatrix} e^{ikL}r_1^2r_2P^+(L) - r_1 & e^{ikL}r_1r_2Q^+(L) \\ -r_1^2Q^-(L) & e^{ikL}r_1^2r_2 - r_1P^-(L) \end{pmatrix} \begin{bmatrix} E_L^-(0) \\ E_R^-(0) \end{bmatrix} \\
&= \begin{pmatrix} e^{ikL}r_1r_2P^+(L) - 1 & e^{ikL}r_2Q^+(L) \\ -r_1Q^-(L) & e^{ikL}r_1r_2 - P^-(L) \end{pmatrix} \begin{bmatrix} r_1E_L^-(0) \\ r_1E_R^-(0) \end{bmatrix} \\
&= \begin{pmatrix} e^{ikL}r_1r_2P^+(L) - 1 & e^{ikL}r_2Q^+(L) \\ -r_1Q^-(L) & e^{ikL}r_1r_2 - P^-(L) \end{pmatrix} \begin{bmatrix} E_R^+(0) \\ E_L^+(0) \end{bmatrix} \\
&= \begin{pmatrix} e^{ikL}r_1r_2P^+(L) - 1 & e^{ikL}r_2Q^+(L) \\ -r_1Q^-(L) & e^{ikL}r_1r_2 - P^-(L) \end{pmatrix} \begin{bmatrix} E_R^+(0) \\ E_L^+(0) \end{bmatrix}.
\end{aligned} \tag{5.11}$$

Note that the calculations are slightly cumbersome as we could not assume that $r_1, r_2 \neq 0$.

Equation (5.11) holds in the trivial case whenever $E_R^+(0) = E_L^+(0) = 0$. For a laser we are interested in the case when Equation (5.11) holds and $E_R^+(0) \neq 0$ and $E_L^+(0) \neq 0$. This produces a finite output (see the boundary conditions (5.3) and (5.5)) without any external input. The only case when this can occur is when the determinant of the matrix in Equation (5.11) is 0, so we find that the lasing condition for a structurally chiral laser is

$$\boxed{\left(e^{ikL}r_1r_2\right)^2 P^+(L) - 2e^{ikL}r_1r_2 + P^-(L) = 0} \tag{5.12}$$

where we use that $P^+P^- - Q^+Q^- = 1$.

In the absence of boundary reflections ($r_1 = r_2 = 0$) the lasing condition reduces to

$$\boxed{P^-(L) = 0} \tag{5.13}$$

which is the same lasing condition as for an index-matched scalar distributed feedback laser and simply implies that

$$r_c, t_c \to \infty. \tag{5.14}$$

To better understand the lasing condition for a non-index-matched structurally chiral laser we can explicitly exclude the case where $P^-(L) = 0$. We divide Equation (5.11) by $P^-(L)$

and use Equations (3.53), (3.54), (3.56) and (3.57) to find that

$$\begin{pmatrix} e^{ikL}r_1r_2t_c & e^{2i(k+p)L}r_1r_2^2r_c \\ r_1r_c & e^{ikL}r_1r_2t_c \end{pmatrix} \begin{bmatrix} E_R^+(0) \\ E_L^+(0) \end{bmatrix} = \begin{bmatrix} E_R^+(0) \\ E_L^+(0) \end{bmatrix}. \tag{5.15}$$

Examining the coefficients in the matrix in Equation (5.15) shows that they coincide exactly with the round trip coefficients introduced in Equation (3.66). The matrix

$$\begin{pmatrix} a_{RR} = e^{ikL}r_1r_2t_c & a_{LR} = e^{2i(k+p)L}r_1r_2^2r_c \\ a_{RL} = r_1r_c & a_{LL} = e^{ikL}r_1r_2t_c \end{pmatrix} \tag{5.16}$$

is the round trip propagation matrix, which propagates the forward moving portion of the field at $z = 0^+$ through the structurally chiral medium along the permissible light paths (seen in Figure 3.1) and returns the fields to $z = 0^+$ in the forward moving direction after one round trip.

Equation (5.15) therefore states that after the forward moving portion of the field at $z = 0^+$ is propagated by the round trip propagation matrix it must retain its value exactly. Any losses incurred inside the structurally chiral medium and at the boundaries must be compensated for by the gain and the polarisation must remain the same. This is the round trip lasing condition and provides a logical and physically more easily interpretable condition than Equation (5.11). It is less complete, as for it to hold boundary reflections must exist, since otherwise the round trip paths depicted in Figure 3.1 make little sense and need to be reinterpreted. However, as boundary reflections will always exist between a gain medium with complex refractive index and a medium with a real refractive index the two lasing conditions are essentially the same.

We compare the lasing conditions for an index-matched and a non-index-matched scalar distributed feedback laser and structurally chiral laser in Table 5.1. Notice that the lasing condition of a scalar distributed feedback laser and a structurally chiral laser agree in the index-matched case. This occurs because there are no chirality reversing boundary reflections, which might alter any number of factors determining the lasing condition, including the photon dwell time. The index-matched scalar distributed feedback laser

lasing condition was first discovered by Kogelnik and Shank in 1972 [3]. The only difference between the scalar distributed feedback laser and the structurally chiral laser is the output polarisation of the laser, where the output polarisation of the scalar distributed feedback laser is undetermined while the output polarisation of the structurally chiral laser must be right circular polarisation for a right-handed structure.

	Index-matched	non-index-matched
scalar distributed feedback laser	$P^{-}(L)=0$	$P^{-}(L)+r_1Q^{-}(L)-r_2Q^{+}(L)-r_1r_2P^{+}(L)=0$
structurally chiral laser	$P^{-}(L)=0$	$\left(e^{ikL}r_1r_2\right)^2 P^{+}(L)-2e^{ikL}r_1r_2+P^{-}(L)=0$

Table 5.1: Comparison of the lasing conditions of index-matched and non-index-matched scalar distributed feedback lasers and structurally chiral lasers.

In reality, a perfectly index-matched laser is not feasible, as the complex refractive index inside the laser cannot be matched to the real refractive index in the media surrounding the lasing cavity. Once gain is introduced the Fresnel reflections automatically occur. These reflections introduce a shift in the lasing modes with regard to both the lasing wavelength and the threshold gain, as we shall demonstrate in the next section. For a scalar distributed feedback laser these changes have no qualitative significance when the reflections are low. We shall demonstrate in the coming section that the Fresnel reflections are important in a structurally chiral laser, as they introduce another lasing mechanism, which allows for more lasing modes of opposite chirality as well as lasing within the photonic bandgap. These surprising results highlight the possibility of intriguing new uses of structurally chiral lasers.

5.3 Modelling Structurally Chiral Lasers

Equation (5.12) is a transcendental equation, which we would like to solve over a range of detuning and threshold gain. In order to keep our plots dimensionless we use $\mathrm{Re}\,[\delta kL/2]$ as a dimensionless measure of detuning and $\mathrm{Im}\,[\delta kL/2]$ as a dimensionless measure of gain. $\mathrm{Re}\,[\delta kL/2] = 0$ represents the Bragg wavelength while $\mathrm{Im}\,[\delta kL/2] = 0$ represents no gain.

We plot only for positive gain and for wavelengths higher than the Bragg wavelength. The plots for wavelengths lower than the Bragg wavelength are mirrored with respect to the ones presented here. In doing so we follow the conventions set out in [3] and [71].

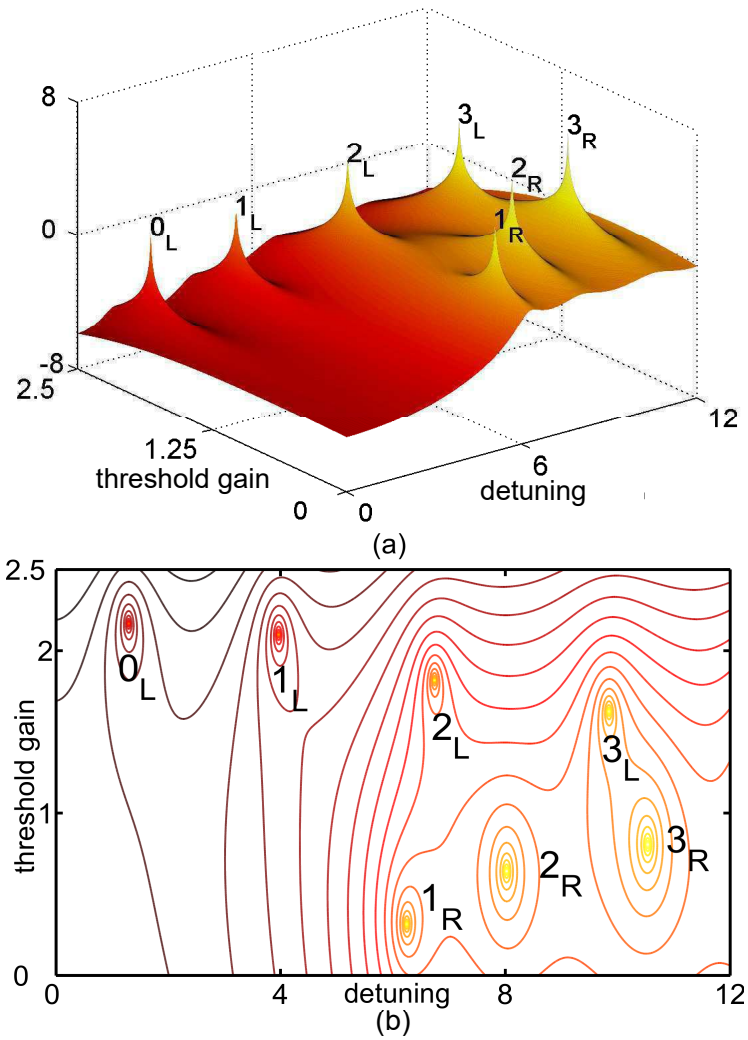

Figure 5.1: Lasing Modes for a structurally chiral laser as a surface plot (a) and as a contour plot (b) plotted with respect to detuning ($\mathrm{Re}\,[\delta kL/2]$) and threshold gain ($\mathrm{Im}\,[\delta kL/2]$). The lasing modes appear as poles that occur in two groups, one group with high gain thresholds ($0_L, 1_L, 2_L, 3_L$) and a group with low gain thresholds ($1_R, 2_R, 3_R$). Reproduced with permission from [1].

Given the real parameters κL, n_1, n_2 and n_c, Equation (5.12) can be solved numerically for the lasing modes. In Figure 5.1 we plot a surface plot as well as a contour plot of the absolute reciprocal of the left hand side of Equation (5.12), so that diverging peaks correspond to lasing modes. We fix the coupling strength ($\kappa L = 4$) and use the values specified in Table 5.2, for which $r_1 = r_2 = 0.278$ and $\lambda_0^{Br} = 530.4$nm. Figure 5.1 (a) and (b) are logarithmic plots constructed using MATLAB, so that peaks mark detuning and gain values for which the inverse of the left hand side of Equation (5.12) diverges. The left hand side of Equation (5.12) then approaches 0, as required for the lasing condition to hold.

Structural period	$L_p = 300$ nm
Depth of chiral medium	$L = 6\,\mu$m
Number of half periods	$L/L_p = 20$
Average refractive index (Re)	$\mathrm{Re}\,(\bar{n}) = 1.7680$
Chiral birefringence at λ_0^{Br}	$\delta n = 0 - 0.1126$
Refractive index of surrounding media	$n_1 = n_2 = 1$

Table 5.2: Data used for calculations.

Within the range plotted, seven lasing peaks are observed, which can be divided into a group with high gain thresholds $(0_L, 1_L, 2_L, 3_L)$ and a group with low gain thresholds $(1_R, 2_R, 3_R)$. The labelling scheme relates to the chirality of the modes, as discussed below.

In order to determine the physical origin and characteristics of the modes, their movement is traced as the coupling strength κL is reduced to zero, as seen in Figure 5.2. Throughout we will refer to the lines tracing the movement of the modes as *lasing loci*. The coupling represents the birefringence of the structurally chiral medium, with higher coupling representing a more birefringent material, which will be more distributively reflecting. At zero coupling the only reflection mechanism is reflection from the boundaries, so that the modes marked by black crosses are Fabry-Pérot modes spaced $\Delta(\delta kL/2) = \pi$ apart. Three of the four Fabry-Pérot lasing modes split into paired branches as the coupling is introduced. The bifurcation thereby created shows that 6 of the lasing modes can be paired up as $(1_L, 1_R)$, $(2_L, 2_R)$ and $(3_L, 3_R)$. The dashed lines in Figure 5.2 identify constant values of κL.

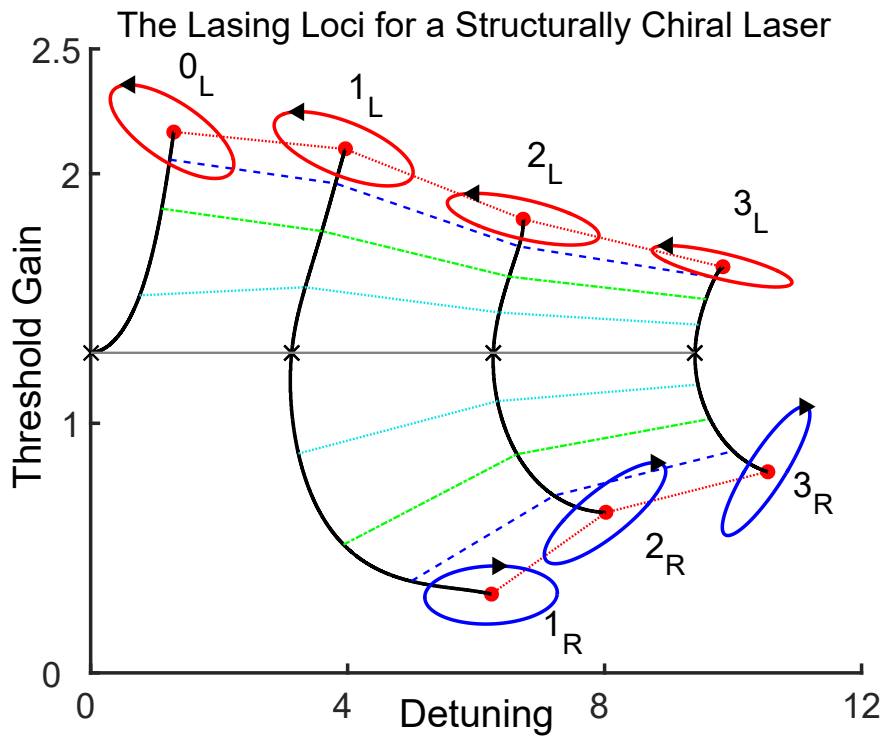

Figure 5.2: Movement of the lasing modes with respect to varying κL, plotted with respect to detuning ($\mathrm{Re}\,[\delta kL/2]$) and threshold gain ($\mathrm{Im}\,[\delta kL/2]$). The solid lines trace the evolution of the modes of Figure 5.1 (red dots) as κL is reduced to zero (black crosses). The dashed lines connect modes of constant κL. The superimposed ellipses represent the lasing output polarization when $\kappa L = 4$. Reproduced with permission from [1].

Once a lasing mode has been identified, the forward propagating field at $z = 0^+$ is determined from Equation (5.11). While in general there are a number of eigenmode solutions to Equation (5.11), we found that for the lasing modes, when $\kappa L \neq 0$,

$$\begin{bmatrix} E_R^+(0) \\ E_L^+(0) \end{bmatrix} = \begin{bmatrix} P^-(L) - r_1 r_2 e^{ikL} \\ -r_1 Q^-(L) \end{bmatrix}. \tag{5.17}$$

All lasing polarizations are elliptical, becoming more circular as κL increases. When $\kappa L = 0$ the chiral laser becomes a pure Fabry-Pérot laser and the modes become polarization degenerate. The output polarization $[E_L^+(L), E_R^+(L)]^T$ is determined from Equations (5.3)-(5.6). From Figure 5.2 we note that the high gain threshold modes lase left circular polarisation (dashed red ellipses) while the low gain threshold modes lase right circular polarisation (solid blue ellipses).

In Figure 5.3 we plot the total intensity envelope $I(z) = |E_L^+(z)|^2 + |E_R^-(z)|^2 + |E_L^-(z)|^2 +$

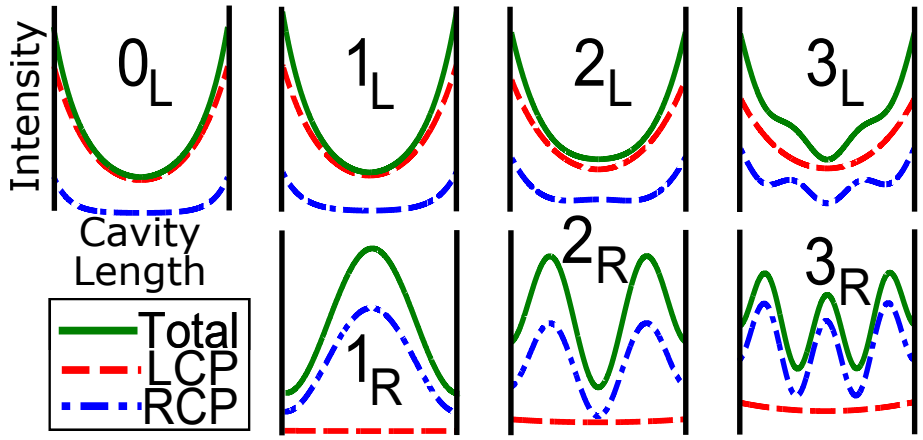

Figure 5.3: Intracavity intensity envelopes for the seven modes in Figure 5.1 of the total (green), left circular polarisation (red) and right circular polarisation (blue) electric fields for a 6 μm structurally chiral medium cavity. Reproduced with permission from [1].

$|E_R^+(z)|^2$, as well as the left circular polarisation and right circular polarisation intensity envelopes $I_{L,R}(z) = |E_{L,R}^+|^2 + |E_{L,R}^-|^2$ for $0 < z < L$. The black vertical lines represent the boundaries of the structurally chiral laser and the vertical axis is a measurement of the intensity, in arbitrary units. The total energy of the higher gain threshold modes is concentrated at the boundary, whereas for the lower gain threshold modes the total energy is concentrated within the gain medium. In the higher gain threshold modes right circular polarisation remains concentrated at the boundary and the Fabry-Pérot mechanism generating left circular polarisation provides the majority of the laser power. The opposite is true for the lower modes, where the distributed feedback mechanism generating right circular polarisation dominates over the Fabry-Pérot mechanism generating left circular polarisation. There is therefore a clear distinction between the higher gain thershold modes lasing left circular polarisation, which rely on the Fabry-Pérot mechanism to lase and the conventional, lower gain threshold modes lasing right circular polarisation, which rely on the distributed feedback mechanism.

The distributed feedback mechanism in the lower gain threshold modes allows lasing at a lower gain threshold than the degenerate Fabry-Pérot modes at $\kappa L = 0$. However, for the higher gain threshold modes, intracavity left circular polarisation experiences a homogeneous medium, for which chirality reversing boundary reflections represent a loss mechanism into right circular polarisation. Introducing a right-handed structurally chiral medium therefore increases the lasing threshold for the left circular polarisation high gain

threshold modes, which lase due to the Fabry-Pérot mechanism. When such a medium is introduced, the polarization degeneracy of the Fabry-Pérot modes is lifted, so that the modes bifurcate as shown in Figure 5.2.

The lone status of the 0_L mode results from lasing *within* the photonic bandgap for all κL. For this mode the photon density of states is zero for right circular polarisation, and it can therefore only lase via the Fabry-Pérot mechanism. We see the intriguing possibility that a structurally chiral laser can operate within the photonic bandgap. The unique properties of the structurally chiral laser ensure that this isolated mode occurs with opposite polarization to the principal modes of the structurally chiral medium.

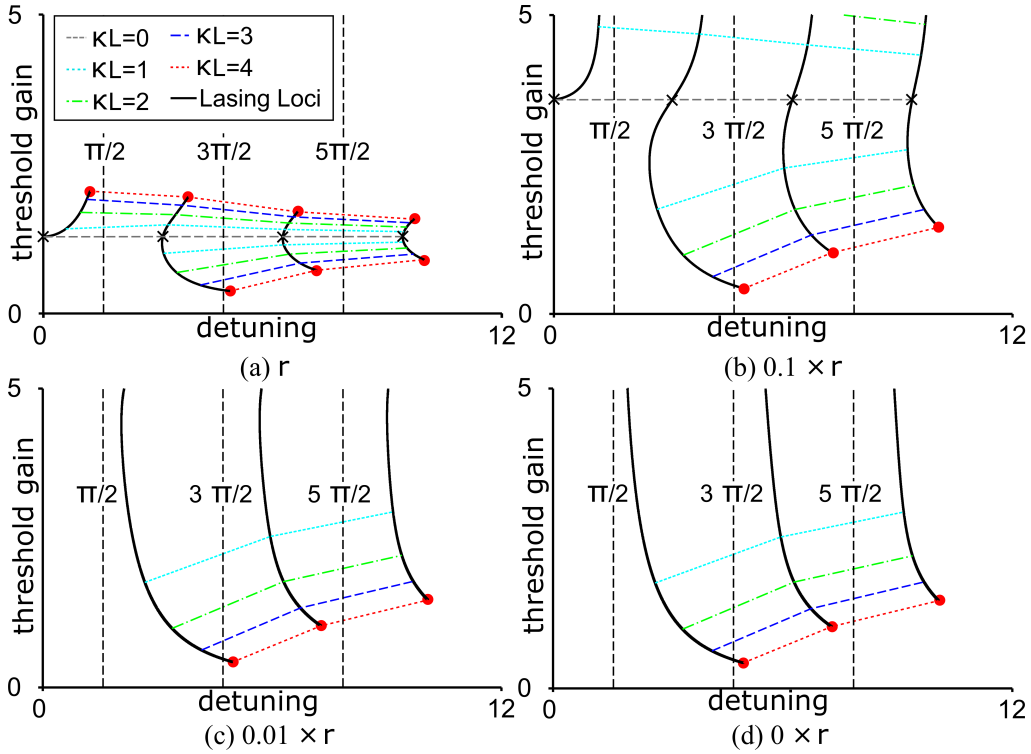

Figure 5.4: Evolution of chiral modes as the facet reflectivities are reduced by the given factor, plotted with respect to detuning ($\mathrm{Re}\,[\delta kL/2]$) and threshold gain ($\mathrm{Im}\,[\delta kL/2]$). Subfigure (a) corresponds to Figure 5.2, while in Subfigure (d) the purely right circular polarisation modes correspond exactly to the index-matched scalar distributed feedback laser modes enumerated by Kogelnik and Shank [3]. Reproduced with permission from [1].

In Figure 5.4 the boundary reflections are gradually reduced in order to examine the effect that decreasing the Fabry-Pérot lasing mechanism has on the chiral lasing modes. We establish that as the boundary reflections approach zero the gain threshold for the higher gain threshold modes diverges and only the lower gain threshold modes remain. When

the facet reflectances are eliminated (Figure 5.4(d)), the remaining modes agree with the scalar distributed feedback laser modes enumerated by Kogelnik and Shank [3].

5.4 Why Lasing Occurs at the Long Wavelength Band-edge

In this section a recent discovery is highlighted, which explains why lasing is predominantly observed at the long wavelength end of the bandgap. In existing literature on distributed feedback lasers the coupling constant κL is kept constant when producing graphs [3, 71]. However, by doing so an important subtlety is missed. Consider that

$$\kappa L = \frac{L\pi\left(n_d - n_c\right)}{\lambda_0}, \tag{5.18}$$

so that keeping κL constant while changing the detuning (and thereby the wavelength λ_0) implies that the birefringence $n_d - n_c$ of the structurally chiral medium must change. Therefore keeping κL constant for a given graph changes the birefringence and therefore means that the graph drawn does not hold for a single material.

If instead the graph is drawn for a constant birefringence and varying κL the lasing mode structure shifts slightly, as seen in Figure 5.5. The lasing modes move with respect to detuning and threshold gain when compared to Figure 5.1, but the movement is minimal. However, the observed changes indicate that when the birefringence is kept constant the symmetry with regards to wavelength is broken. The modes with shorter wavelengths ($\mathrm{Re}\left(\delta kL/2\right) < 0$) have a slightly higher gain threshold than their counterparts with longer wavelengths. The difference in wavelengths between the modes is highlighted by the pink and blue dotted lines in Figure 5.5. The short wavelength primary mode lies on the higher gain threshold pink line while the long wavelength primary mode lies on the low gain threshold blue line.

In reality experimental considerations may easily counteract the slight threshold gain difference between the two modes, so that short wavelength lasing may occur. Nevertheless, all else remaining equal, a structurally chiral laser will lase on the long wavelength lasing

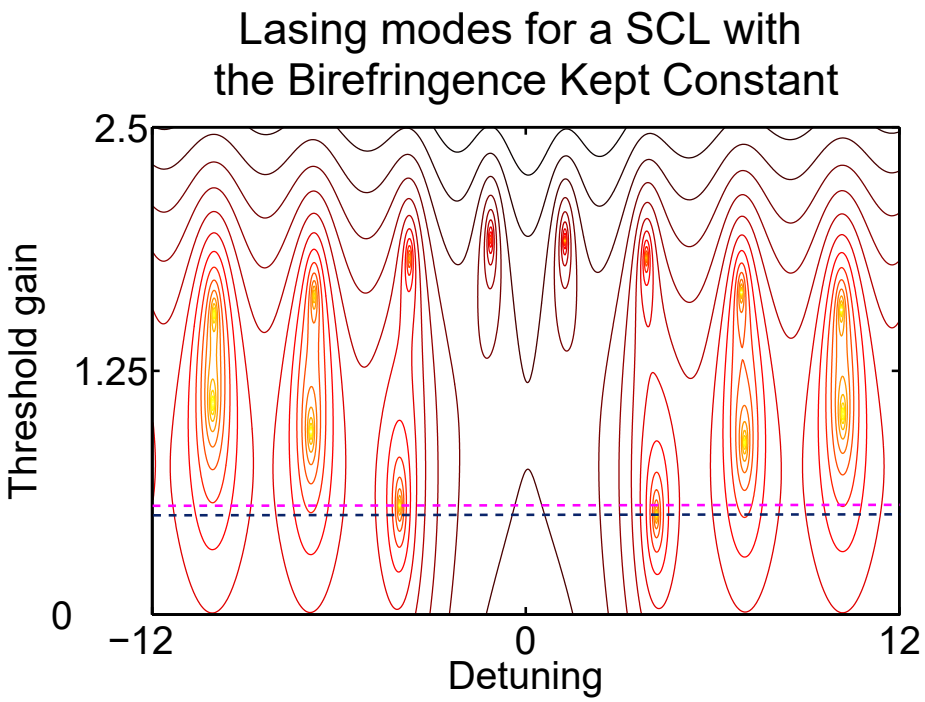

Figure 5.5: Lasing mode contour plot for a structurally chiral laser with constant birefringence, plotted over a range of detuning from $-12 < \mathrm{Re}\,(\delta kL/2) < 12$ and threshold gain ($\mathrm{Im}\,[\delta kL/2]$). Notice the slight shift in the lasing modes when compared to the lasing mode contour plof for a structurally chiral laser with κL kept constant. The short wavelength primary lasing mode has a slightly higher threshold gain (marked by the pink dotted line) than the long wavelength primary lasing mode (blue dotted line).

mode. This phenomenon has been observed experimentally and our research now shows why it occurs.

5.5 Summary of the Research into structurally chiral lasers

The analysis drawn from the calculations and figures presented in this chapter provide a clear and compelling picture of the lasing modes of a structurally chiral laser. We have shown that there are two separate, competing lasing mechanisms in a structurally chiral laser, which feed into one another.

The first is the expected distributed feedback mechanism, which is attributed to the distributed reflections caused by the structure of the structurally chiral medium. It provides gain to right circular polarisation (for a right-handed structure) and the more dominant it is, the more right-handed the polarisation ellipse of the lasing mode will be.

The distributed feedback mechanism of the structurally chiral laser works in the same way to the distributed feedback mechanism of a scalar distributed feedback laser as covered in [3], except that it is polarisation dependent. We therefore have a band-edge lasing mode (1_R) and consecutively higher gain threshold lasing modes (2_R, 3_R, etc.), each lasing at the band edge of the secondary (tertiary etc.) reflection peaks of the Bragg reflection spectrum. As expected, there is no lasing mode within the photonic band-gap. The lasing mechanism is strengthened by an increase in κL, as a higher coupling strength induces a stronger distributed feedback. The lasing modes of a structurally chiral laser attributed to the distributed feedback mechanism are therefore qualitatively the same as those of a scalar distributed feedback laser.

The distributed feedback mechanism is further strengthened by the boundary reflections caused by the index mismatch. A portion of the right circular polarisation that would exit the structurally chiral medium at the boundary is instead reflected back into the structure due to the Fresnel reflections. There it becomes left circular polarisation, travels through the structure and either exits the structure or is fed back into the distributed feedback mechanism. This has two consequences. The first is that the output polarisation can never be purely right circular polarisation, as left circular polarisation is generated. The second is that the photon dwell time is increased, so that the gain threshold for the modes is lower than for distributed feedback lasing modes that do not have additional boundary reflections.

The second lasing mechanism encountered in structurally chiral lasers is the Fabry-Pérot mechanism, which is introduced by the refractive index mismatch at the boundary between the structurally chiral laser and the surrounding media and induces Fresnel reflections. The Fabry-Pérot mechanism works in the same way as in a regular Fabry-Pérot laser, with constant gain being provided throughout the length of the structure and boundary reflections providing the necessary reflections to create the laser. The Fabry-Pérot mechanism provides gain to left circular polarisation and the more dominant it is the more left-handed the polarisation ellipse of the lasing mode will be. It is independent of polarisation and can therefore lase at any wavelength for which the Fabry-Pérot resonance condition holds, even inside the photonic bandgap.

There are some subtleties to consider with the Fabry-Pérot mechanism. Firstly, the optical path length of any given lasing mode is not immediately obvious, as the boundary reflections switch the handedness of the polarisation and right circular polarisation does not travel straight through the structure. The distributed feedback right circular polarisation experiences is dependent on the coupling strength, so right circular polarisation has a varying optical path length. As the optical path length of the right circular polarisation forms part of the total optical path length of the lasing mode, the optical path taken by light attributed to the Fabry-Pérot mechanism is dependent on the coupling strength. This effect explains the gradual shift in detuning of the Fabry-Pérot lasing modes seen in Figure 5.2.

Secondly, the Fabry-Pérot mechanism converts all the energy that is reflected at the boundary into right circular polarisation after every reflection. The energy then remains right circular polarisation until the distributed feedback mechanism converts it back into left circular polarisation at the boundary. As the distributed feedback reflection relies on the incremental reflection inside the structure the proportion spent as right circular polarisation is usually much longer than the proportion spent as left circular polarisation. The Fabry-Pérot mechanism with left circular polarisation can therefore only dominate when the dwell time of the right circular polarisation in the distributed feedback mechanism is extremely low. Figure 5.3 supports this conclusion, as we can see that right circular polarisation is concentrated at the boundaries. For the detuning at which the Fabry-Pérot mechanism lases the distributed feedback mechanism is highly overcoupled. Any light travelling into the structurally chiral medium as right circular polarisation is almost immediately reflected back towards the boundary, which reduces the dwell time to considerably below that of left circular polarisation. Only when this occurs can the Fabry-Pérot mechanism dominate and lase.

Finally, the Fabry-Pérot modes as presented so far rely on very weak reflections caused by the index mismatch at the boundary. Any Fabry-Pérot laser has mirrors with much stronger reflectances than those created by the index mismatch of the structurally chiral laser presented here. The gain threshold for these modes is therefore very high. They are inefficient modes, but modifications to the structure can easily rectify the situation, as we

will demonstrate in Chapter 6.

5.6 Dynamic Polarisation Switching

Our analysis of structurally chiral lasers uncovered previously undocumented features, which may be harnessed for improvements in research and industry, where structurally chiral lasers in the form of liquid crystal lasers are regularly used. The obvious new uses include lasing inside the photonic band gap and building a non-index-matched laser for which the exact lasing wavelength and gain threshold can be calculated ahead of time. Currently most structurally chiral lasers are built, pumped and expected to lase at the band-edge, which in our analysis is the 1_R mode. A preliminary theoretical analysis using our methodology could allow for greater finesse when designing and fabricating structurally chiral lasers.

Another intriguing possibility, which has not yet been observed experimentally, is lasing left circular polarisation using a right-handed structure. As the gain threshold for these modes is higher than for the right circular polarisation modes and they have not been predicted by previous theoretical analyses they have never been sought for and observed experimentally. Inducing a simple structurally chiral laser to lase with a polarisation contra-handed to the helicity of the structurally chiral medium would be a novel result in its own right.

Perhaps the most interesting proposition is to achieve dynamic polarisation switching using a structurally chiral laser. Let us suggest one possible way in which this may be possible. Begin by doping the structurally chiral medium with an active medium that has a fluorescence profile that fits inside the photonic band gap of the structurally chiral medium (see Figure 5.6a). While most dyes used in structurally chiral lasers have wide gain profiles, there are a number of possible dye and liquid crystal combinations that could be chosen. Pumping the structurally chiral laser should now target the only lasing mode inside the fluorescence profile, which is the left circular polarisation 0_L mode.

Once lasing occurs the structurally chiral medium can be tuned using an electric field (or

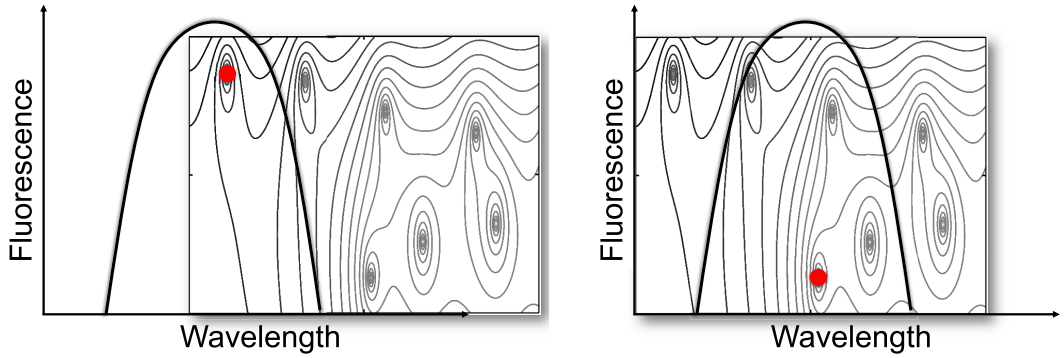

(a) Plot of the fluorescence profile of the active medium against the wavelength. The lasing mode structure of the structurally chiral laser is shown in grey. Left circular polarisation lasing using the 0_L lasing mode (red circle) will occur, as no other mode is inside the fluorescence profile.

(b) Plot of the fluorescence profile of the active medium against the wavelength. The lasing mode structure of the structurally chiral laser is shown in grey. Right circular polarisation lasing using the 1_R lasing mode (red circle) will occur, as it is the lowest gain threshold lasing mode.

Figure 5.6: Subfigure (a) demonstrates a structurally chiral medium tuned to target the high gain threshold left circular polarisation lasing mode inside the photonic band-gap. Subfigure (b) demonstrates a structurally chiral medium tuned to target the low gain threshold right circular polarisation lasing mode at the band-edge. It is possible to tune a structurally chiral medium to switch between the two set-ups dynamically.

a number of other methods), so that the 0_L lasing mode shifts out of the fluorescence profile of the gain medium and the band-edge shifts into the fluorescence profile. It should then no longer be possible to lase using the 0_L mode and instead the lowest gain threshold mode, which is the band-edge mode (1_L), would be targeted (see Figure 5.6b).

Using this method we can dynamically switch from left circular polarisation to right circular polarisation lasing. The reverse procedure can then be used to dynamically switch from right circular polarisation to left circular polarisation lasing. If the tuning is done carefully, the wavelength of both modes can be kept virtually the same, so that even though we change lasing modes only the polarisation changes.

While the ideas presented above are interesting from a research perspective, there are certainly improvements on the structurally chiral laser design that would make these types of lasers more realistic for use in industry. In Chapter 6 we use our research on structurally chiral lasers to analyse the hybrid chiral laser, which is one such design.

Chapter 6

Hybrid Chiral Lasers

6.1 Introduction to Hybrid Chiral Lasers

The motivation for studying the hybrid chiral laser comes from a desire to improve upon the feasibility of using the structurally chiral laser for applications. The coupling of the two lasing mechanisms observed in a structurally chiral laser restricts its flexibility. One restriction is the technical difficulty inherent in switching circular polarisation states using the method discussed in Section 5.6. Another is the need to improve upon the purity of the circular polarisation of the lasing modes. It is also not yet clear if the left circular polarisation modes are easily accessible, as their threshold is higher than that of an inefficient Fabry-Pérot laser (see the black crosses in Figure 5.2).

These restrictions can be eliminated if the boundary reflections are replaced by mirrors that reflect only left circular polarisation and preserve chirality. In this way the chirality reversal seen in a structurally chiral laser is eliminated and no new reflections are introduced into the distributed feedback mechanism. A left-handed structurally chiral medium has exactly these properties, as it distributively reflects left circular polarisation without affecting right circular polarisation and the reflections are chirality preserving.

In this chapter we therefore analyse the hybrid chiral laser, which consists of a right handed active structurally chiral medium surrounded by, and index matched to, two passive left

handed structurally chiral media, each of length L (see Figure 2.2). Examining the hybrid chiral laser we predict that it incorporates two decoupled lasing mechanisms. The first lasing mechanism uses the structurally chiral laser inside the central region and has been analysed in Chapter 5. The second lasing mechanism uses the two passive structurally chiral media mirrors on either side of the central cavity. Before a thorough analysis of the hybrid chiral laser can be conducted the second lasing mechanism needs to be understood.

Consider the chiral distributed Bragg reflector laser presented in Figure 2.3, which consists of a birefringent active central region surrounded by, and index matched to, two passive left handed structurally chiral media, each of length L. We shall demonstrate that the lasing modes of a chiral distributed Bragg reflector laser are a subset of the lasing modes of a hybrid chiral laser. It is therefore instructive to begin by modelling the chiral distributed Bragg reflector laser before modelling the hybrid chiral laser.

We begin the chapter by establishing the general lasing condition for the hybrid chiral laser in Section 6.2. We shall demonstrate that the lasing condition for the chiral distributed Bragg reflector laser is a special case of the general lasing condition for the hybrid chiral laser. In Section 6.3 we model the chiral distributed Bragg reflector laser and analyse the nature of the discovered lasing modes. In Section 6.4 we model the hybrid chiral laser using the general lasing condition and demonstrate that the lasing modes of the hybrid chiral laser are a combination of the lasing modes of an index-matched structurally chiral laser and a chiral distributed Bragg reflector laser. We shall further demonstrate that the two lasing mechanism are uncoupled, as expected.

6.2 Lasing Condition for Hybrid Chiral Lasers

A given structurally chiral medium is characterized by $\bar{n}$, its mean (complex) refractive index, δn, the birefringence between modes propagating along the axis of the helix, and L_p, the structural period of the helix. We have used coupled wave theory in Chapter 3 to analyse the propagation of electromagnetic waves through structurally chiral media. As the chiral distributed Bragg reflector laser and the hybrid chiral laser are constructed from

three consecutive structurally chiral media building blocks, some of our previous analysis can be used.

We rewrite Equation (3.51) as

$$\mathbf{E}|_{z_2^-} = \begin{bmatrix} E_{co}^+ \\ E_{co}^- \\ E_{contra}^+ \\ E_{contra}^- \end{bmatrix}_{z_2^-} = \begin{bmatrix} \mathcal{P}^+ & \mathcal{Q}^+ & 0 & 0 \\ \mathcal{Q}^- & \mathcal{P}^- & 0 & 0 \\ 0 & 0 & e^{ikl} & 0 \\ 0 & 0 & 0 & e^{-ikl} \end{bmatrix} \begin{bmatrix} E_{co}^+ \\ E_{co}^- \\ E_{contra}^+ \\ E_{contra}^- \end{bmatrix}_{z_1^+}, \tag{6.1}$$

where the forward and backward propagating electric fields are considered at z_1^+ (i.e. just beyond z_1) and z_2^- (i.e. just before z_2) and the subscript *co* (respectively *contra*) represents the electric field component that is co-handed (contra-handed) with the structurally chiral medium. Further, we define modified versions of P and Q, so that

$$l = z_2 - z_1, \tag{6.2}$$

$$p = \pm\frac{2\pi}{L_p}, \tag{6.3}$$

$$\mathcal{P}^\pm = e^{\pm ip\ell}\left[\cosh(\Delta\ell) \pm i\frac{\delta k}{2\Delta}\sinh(\Delta\ell)\right], \tag{6.4}$$

$$\mathcal{Q}^\pm = \pm ie^{\pm ip(z_1+z_2)}\frac{\kappa}{\Delta}\sinh(\Delta\ell), \tag{6.5}$$

and p is positive for a right-handed structurally chiral medium and negative for a left-handed structurally chiral medium. Note that for a homogeneous medium lying between z_1 and z_2 we can set $p = 0$, yielding simply $\mathcal{P}^\pm = e^{\pm ik\ell}$ and $\mathcal{Q}^\pm = 0$. Doing so for the central region will allow us to model a chiral distributed Bragg reflector laser.

The structures considered in this chapter consist of three separate regions, each of length L. The first goes from $-3L/2$ to $-L/2$, the second from $-L/2$ to $+L/2$ and the third from $L/2$ to $3L/2$. Both the sign and magnitude of p vary from one region to the next, resulting in distinct propagation matrices for each region.

The propagation matrices through each region must be combined with matrices that ensure continuity of the transverse fields at the boundary between adjacent regions. For a

boundary at z_0

$$\mathbf{E}|_{z_0^+} = \begin{bmatrix} E_{co}^+ \\ E_{co}^- \\ E_{contra}^+ \\ E_{contra}^- \end{bmatrix}_{z_0^+} = \frac{1}{2} \begin{bmatrix} 1+\frac{\bar{n}^-}{\bar{n}^+} & 0 & 0 & 1-\frac{\bar{n}^-}{\bar{n}^+} \\ 0 & 1+\frac{\bar{n}^-}{\bar{n}^+} & 1-\frac{\bar{n}^-}{\bar{n}^+} & 0 \\ 0 & 1-\frac{\bar{n}^-}{\bar{n}^+} & 1+\frac{\bar{n}^-}{\bar{n}^+} & 0 \\ 1-\frac{\bar{n}^-}{\bar{n}^+} & 0 & 0 & 1+\frac{\bar{n}^-}{\bar{n}^+} \end{bmatrix} \begin{bmatrix} E_{co}^+ \\ E_{co}^- \\ E_{contra}^+ \\ E_{contra}^- \end{bmatrix}_{z_0^-}, \tag{6.6}$$

where $\bar{n}^-$ is the average refractive index at z_0^- and $\bar{n}^+$ the average refractive index at z_0^+.

Labelling the matrices in Equations (6.1) and (6.6) as $\underline{M}_{z_1}^{z_2}$ and $\underline{T}_{z_0}$ respectively, and the column vector of electric field components as $\mathbf{E}|_z$, we have for the composite structure

$$\mathbf{E}|_{(3L/2)^+} = \underline{S}\,\mathbf{E}|_{(-3L/2)^-}, \tag{6.7}$$

where

$$\underline{S} = \underline{T}_{3L/2} \cdot \underline{M}_{3L/2}^{L/2} \cdot \underline{T}_{L/2} \cdot \underline{M}_{-L/2}^{L/2} \cdot \underline{T}_{-L/2} \cdot \underline{M}_{-3L/2}^{L/2} \cdot \underline{T}_{-3L/2}. \tag{6.8}$$

The lasing condition requires that there is no externally injected light, so that the following boundary conditions must be satisfied:

$$E_{co}^+|_{-3L/2} = E_{contra}^+|_{-3L/2} = E_{co}^-|_{3L/2} = E_{contra}^-|_{3L/2} = 0. \tag{6.9}$$

We then have that

$$\begin{bmatrix} E_{co}^+ \\ 0 \\ E_{contra}^+ \\ 0 \end{bmatrix}_{3L/2} = \underline{S} \begin{bmatrix} 0 \\ E_{co}^- \\ 0 \\ E_{contra}^- \end{bmatrix}_{-3L/2}, \tag{6.10}$$

which can be rewritten as

$$\begin{bmatrix} A_{11} & A_{13} \\ A_{31} & A_{33} \end{bmatrix} \begin{bmatrix} E_{co}^+ \\ E_{contra}^+ \end{bmatrix}_{3L/2} = \mathbf{0}, \tag{6.11}$$

with $[A] = \underline{S}^{-1}$ [72]. Non-trivial solutions of Equation (6.11) are found when

$$\boxed{|A_{11}A_{33} - A_{13}A_{31}| = 0,} \tag{6.12}$$

which represents the lasing condition for both a hybrid chiral laser and a chiral distributed Bragg reflector laser.

6.3 Modelling Chiral Distributed Bragg Reflector Lasers

The chiral distributed Bragg reflector laser we shall model has transverse principal axes of the central active region aligned at the boundaries to the corresponding principal axes of the passive regions, in order to minimize chirality-reversing reflections within the device. All three sections have length L and the external medium is considered to be a homogeneous, isotropic medium of index equal to the average index of the passive structurally chiral medium. The remaining parameters are identical to those used in previous chapters, which can be found in Table 5.2, except that the refractive index of the surrounding media is now $n_1 = n_2 = 1.7680$.

For a chiral distributed Bragg reflector laser with these parameters and with $\kappa L = 2.5$, Figure 6.1 shows a contour and surface plot of the inverse of the left hand side of Equation (6.12), with respect to normalized detuning and normalized gain. Lasing modes are identified as the poles where $|A_{11}A_{33} - A_{13}A_{31}|^{-1} \to \infty$, whilst ridges of high transmission correspond to single pass amplification away from the Bragg resonance of the chiral mirrors. Note that there are no amplification ridges associated with the two modes with lowest gain, as these occur within the Bragg zone of the chiral mirrors.

In Figure 6.2 we plot a side view of the lasing mode surface plot for a chiral distributed Bragg reflector laser. Below it we show the passive transmission characteristics of the three-section structure (blue line), along with the transmission characteristic of just one of the chiral reflectors (red, dotted line) given by

$$T_s = \left| \left(\cosh \Delta L - i \frac{\delta k}{2\Delta} \sinh \Delta L \right)^{-2} \right|^2 . \tag{6.13}$$

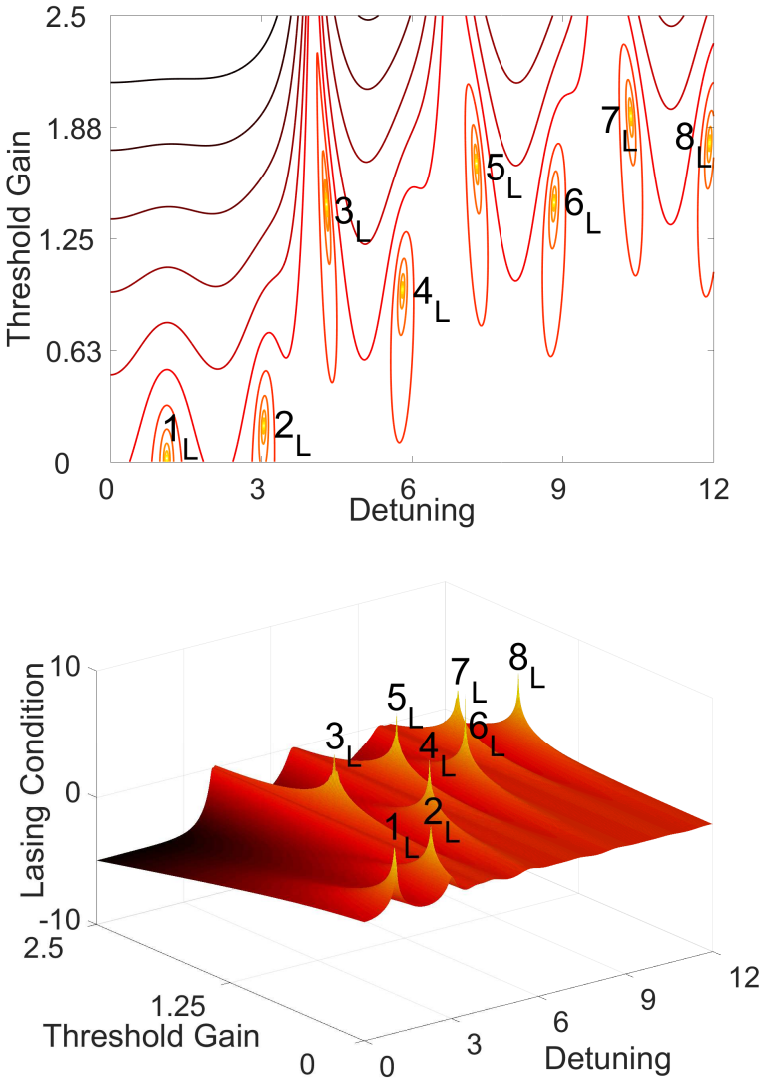

Figure 6.1: Lasing mode structure of an index-matched chiral distributed Bragg reflector laser as a contour plot (top) and a surface plot (bottom), plotted with respect to detuning ($\mathrm{Re}\,[\delta kL/2]$) and threshold gain ($\mathrm{Im}\,[\delta kL/2]$).

The two figures are aligned along the detuning axis in order to highlight the connection between the passive transmission spectrum of the whole structure, the transmission characteristic of a single structurally chiral medium mirror and the lasing modes. Each lasing peak in the surface plot corresponds to unit transmission for the whole structure caused by a Fabry-Pérot resonance and *not* present in the structurally chiral medium transmission plot. These lasing modes experience relatively high reflection by the distributed mirrors (hence no unitary transmission in the red, dotted structurally chiral medium plot) and use the Fabry-Pérot resonance to lase. The ridges occur at unitary transmission for the

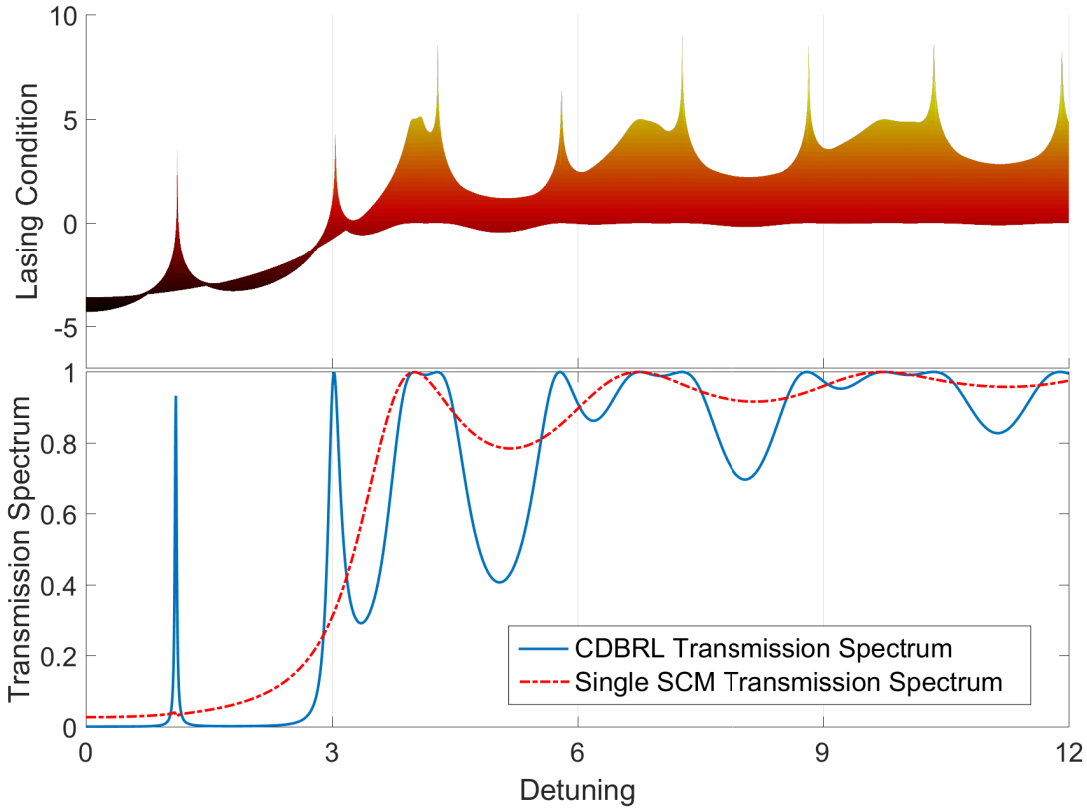

Figure 6.2: Lasing mode structure of an index-matched chiral distributed Bragg reflector laser, plotted with respect to detuning ($\mathrm{Re}\,[\delta kL/2]$). At the top we show a sideview of the surface plot of the lasing condition. Below we show the transmission spectrum of the passive structure as a solid blue line with the transmission spectrum of a single structurally chiral medium mirror of the structure superimposed as a red, dotted line. Compare the position of the lasing peaks and amplification ridges of the chiral distributed Bragg reflector laser in the top half with the transmission peaks of the two spectra in the lower half.

whole structure *and* the structurally chiral medium. At these wavelengths the distributed mirrors do not reflect and no Fabry-Pérot resonance exists. The electromagnetic field passes straight through the structure. The wave is amplified while passing through the active section of the structure, so that amplification ridges are formed in the surface plot. As only infinite peaks in the surface plot are solutions to the lasing condition these ridges are *not* lasing modes.

In Figure 6.3 the polarization ellipses are superimposed onto the lasing modes and we can see that the polarisation purity is very high. However, even though the central region is rotated so that the axes of birefringence can be aligned between the central region and the distributed mirrors to minimise index mismatch, the introduction of gain necessitates

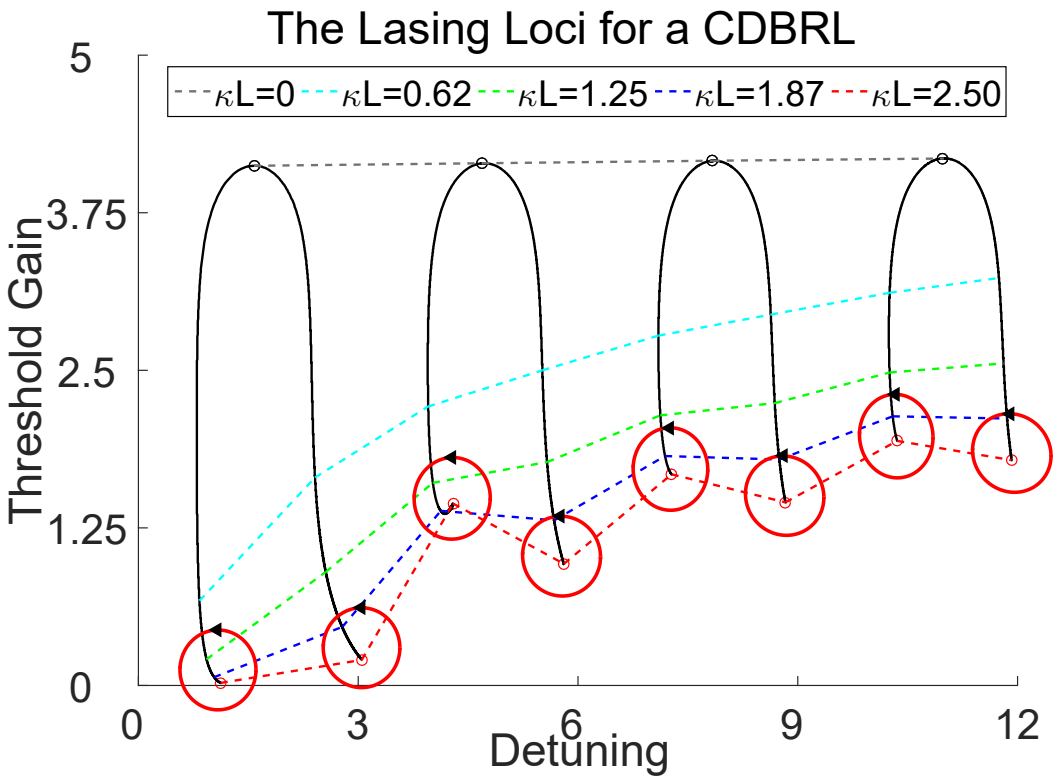

Figure 6.3: Bifurcation of left circular polarisation modes from the degenerate Fabry-Pérot modes in a left-handed chiral distributed Bragg reflector laser when changing the coupling constant $\kappa L : 0 \to 2.5$, plotted with respect to detuning ($\mathrm{Re}\,[\delta k L/2]$) and threshold gain ($\mathrm{Im}\,[\delta k L/2]$). Zero coupling corresponds to a polarisation independent Fabry-Pérot laser. Red circles with arrows indicate the polarisation state of the respective modes.

some reflections. Higher gain introduces a larger imaginary component of the refractive index in the central region, which causes an index mismatch with the passive regions and introduces chirality reversing boundary reflections. Therefore the higher the gain threshold of the lasing mode, the more elliptical it becomes. However the ellipticity remains very small, even at high gain thresholds.

After having analysed the lasing modes, let us use Figure 6.3 to examine how they arise. When the coupling constant $\kappa L = 0$ in a chiral distributed Bragg reflector laser the device consists of an active region surrounded by two homogeneous passive regions, with an index mismatch at the boundaries caused by the gain in the central region. This structure is a weak Fabry-Pérot laser and will lase at high gain threshold using the round trip condition fulfilled by a standing wave solution of a Fabry-Pérot cavity. These lasing modes are the black hollow circles in Figure 6.3.

If we introduce coupling by increasing $\kappa L \to 2.5$ in the passive regions we can track the

movement of the Fabry-Pérot lasing peaks (see Figure 6.3). As we move from a Fabry-Pérot laser to a chiral distributed Bragg reflector laser the lasing loci seen in Figure 6.3 are formed and each Fabry-Pérot mode bifurcates into two chiral distributed Bragg reflector laser modes.

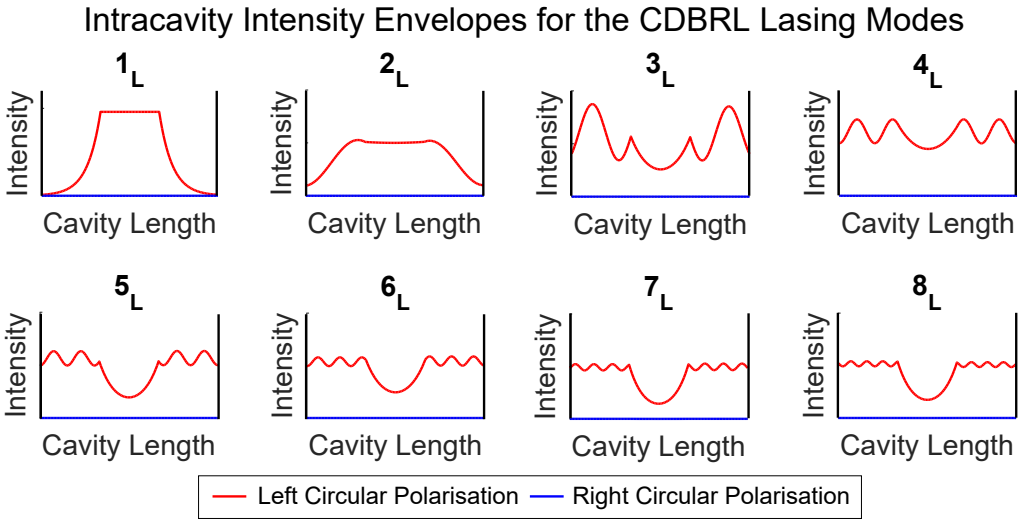

Figure 6.4: Intracavity intensity envelopes for the chiral distributed Bragg reflector laser lasing modes, arranged by increased detuning from the Bragg wavelength. The blue line represents right circular polarisation while the red line represents left circular polarisation. The right circular polarisation intensity for all modes is 0.

In order to understand the bifurcation we conduct an intracavity intensity envelope analysis of the lasing modes, by plotting

$$I_{L,R}(z) = |E^{+}_{L,R}(z)|^2 + |E^{-}_{L,R}(z)|^2 \tag{6.14}$$

for $\kappa L = 2.5$ in Figure 6.4. The chiral distributed Bragg reflector laser modes demonstrate a typical Fabry-Pérot exponential intracavity intensity profile in the central region and experience no reflection inside the central active region. The intensity profile in the passive regions is sinusoidal (or exponentially decaying when inside the Bragg zone: see $1L$ mode), as expected from a passive distributed mirror.

From Figure 6.3 we know that the lasing modes are paired. Figure 6.4 explains why this occurs. Each Fabry-Pérot mode bifurcates into an intracavity intensity profile with an odd and an even number of intensity peaks in the passive chiral mirrors. All lasing modes are

solutions to the maximisation problem of the total internal intensity within the constraints imposed by the structure. The chiral distributed Bragg reflector laser intensity profile is constrained by the central region being a Fabry-Pérot cavity and must therefore have an exponentially decaying intensity profile in the central region. It is further constrained by the passive distributed mirrors on either side, which can either support an exponentially decaying field or a sinusoidally varying field.

At $\kappa L = 0$ the intracavity intensity of the Fabry-Pérot modes is exponentially decaying in the active region and constant in the passive regions. Introducing coupling to the passive regions activates the distributed mirrors. Each Fabry-Pérot mode then has two solutions that maximise the intracavity intensity locally. One solution has an odd number of intensity peaks over both mirrors and the other has an even number of intensity peaks.

The reason that the modes differ with regards to detuning from the Bragg wavelength is that the difference between the intracavity intensities in the mirrors mean that the optical cavity length is different for the two modes. Different optical cavity lengths imply different wavelengths at which the Fabry-Pérot resonance will hold. The added reflection of the distributed mirrors reduces the gain threshold of the laser, so that the bifurcating lasing loci seen in Figure 6.3 are formed.

In conclusion, we have established that the lasing modes of a chiral distributed Bragg reflector laser are paired, bifurcating from the Fabry-Pérot lasing modes as the coupling in the structurally chiral medium mirrors is introduced. The paired lasing modes represent separate solutions to the local maximisation problem of the total intensity. As the different solutions have different optical path lengths the detuning of the lasing modes is not identical and the lasing loci seen in Figure 6.3 are formed.

The structure of the chiral distributed Bragg reflector laser is a Fabry-Pérot etalon and as such it has a number of transmission peaks at different detuning values. Lasing modes exist for each of these peaks, as seen in Figure 6.2. However, the gain threshold of the lasing modes varies, depending on the transmission spectrum of the structurally chiral medium mirrors at that particular wavelengths. In the photonic bandgap the structurally chiral media mirrors are strongly reflective, so that the gain threshold for modes 1_L and

2_L is very low. For the other lasing modes the mirrors are not as strongly reflective and the gain threshold is accordingly higher.

6.4 Modelling Hybrid Chiral Lasers

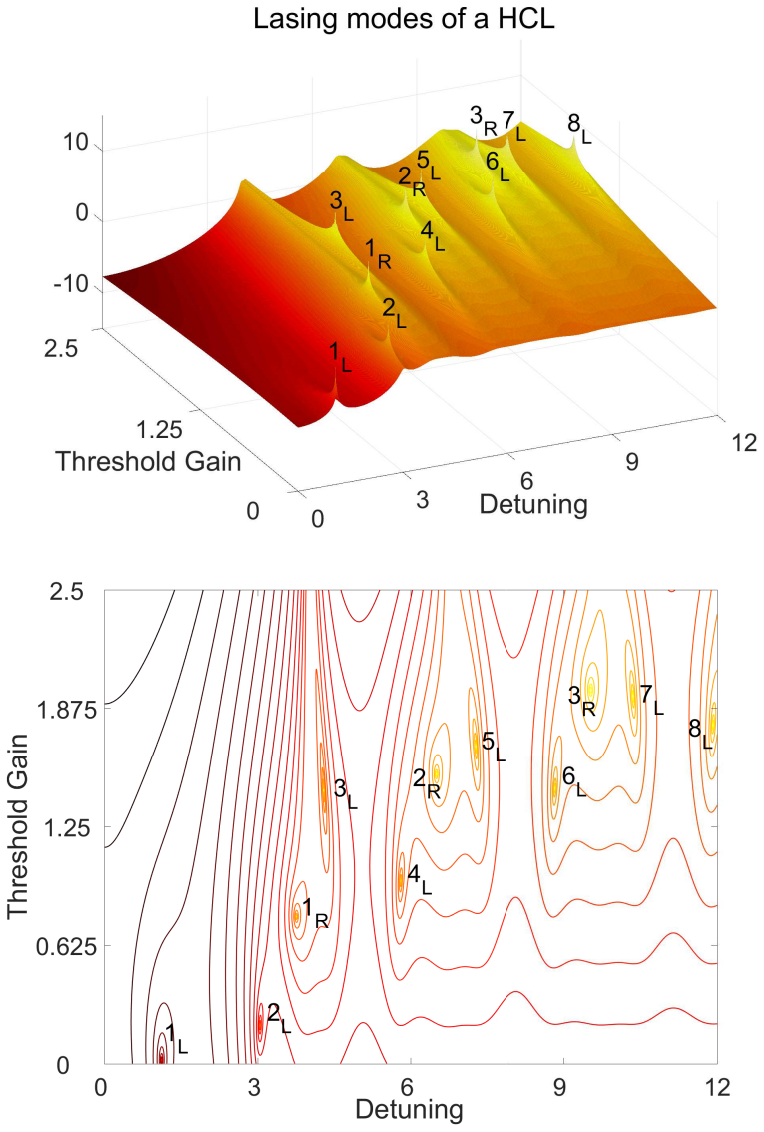

Figure 6.5: Lasing mode structure of an hybrid chiral laser as a surface plot (top) and a contour plot (bottom), plotted with respect to detuning ($\mathrm{Re}\,[\delta kL/2]$) and threshold gain ($\mathrm{Im}\,[\delta kL/2]$).

Now that we understand how the chiral distributed Bragg reflector laser functions and how its lasing modes are formed we can combine the results from Chapter 5 and Sections 6.2 and 6.3 to analyse the hybrid chiral laser. The model for the hybrid chiral laser we analyse consists of a right handed active structurally chiral medium surrounded by, and

index matched to, two passive left handed structurally chiral media, each of length L. As before, the parameters used are given in Table 5.2. We use the lasing condition given by Equation (6.12) and plot the lasing modes for varying detuning and gain for a hybrid chiral laser in Figure 6.5. Comparing the lasing modes in Figure 6.5 with those in Figure 6.1 we notice that all chiral distributed Bragg reflector laser lasing modes are contained in the hybrid chiral laser. The remaining modes in the hybrid chiral laser agree exactly with those of an index-matched structurally chiral laser, as seen in Figure (5.4)(d). It seems likely that the hybrid chiral laser is a combination of the structurally chiral laser and the chiral distributed Bragg reflector laser. To confirm, we analyse the polarisation and intracavity field intensities of the lasing modes and compare them with those of the chiral distributed Bragg reflector laser and index-matched structurally chiral laser.

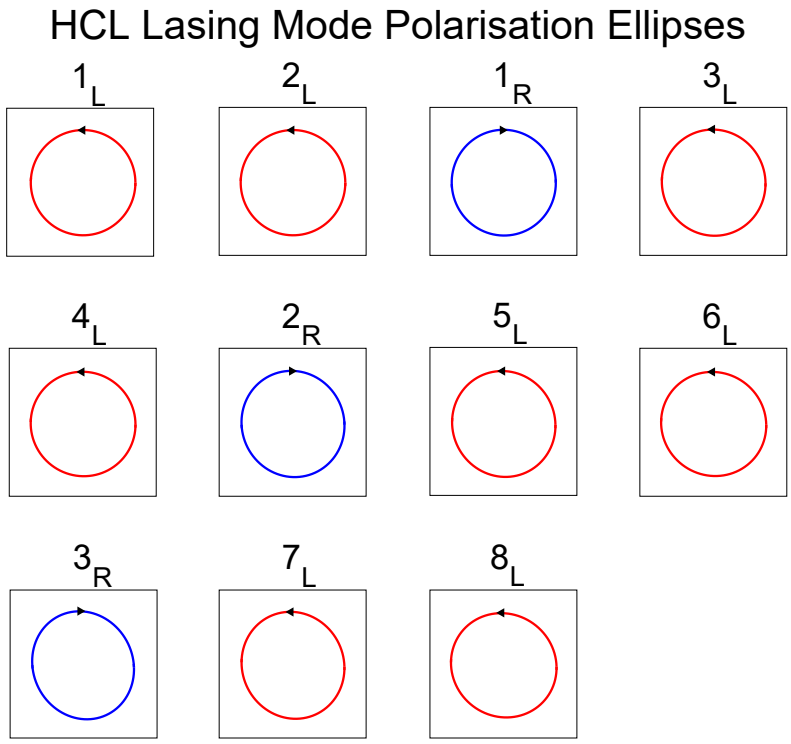

Figure 6.6: Polarisation ellipses of the lasing modes of the hybrid chiral laser at $\kappa L = 2.5$. Red ellipses represent left circular polarisation modes and blue ellipses represent right circular polarisation modes. The lasing modes are numbered by increased detuning from the Bragg wavelength.

In order to find the polarisation of the lasing peaks we rewrite Equation (6.11) as an Eigenmode equation, solve for the Eigenvectors and plot the polarisation ellipses in Figure

6.6. We present the angle

$$\varepsilon = \arctan\left(\frac{b}{a}\right) \tag{6.15}$$

in Table 6.1, which is the angle adjacent to the major axis in the triangle formed by the point a where the major axis intersects the ellipse, the point b where the minor axis intersects the ellipse and the origin. We confirm the purity of the lasing modes, with ε being close to $45°$ for all modes.

Lasing Mode	ε (in degrees)
1_L	45.00°
2_L	44.95°
1_R	44.65°
3_L	44.19°
4_L	44.54°
2_R	43.57°
5_L	43.68°
6_L	43.93°
3_R	41.95°
7_L	42.92°
8_L	43.17°

Table 6.1: ε values for the hybrid chiral laser lasing modes at $\kappa L = 2.5$. The subscript R represents the right circular polarisation modes and L the left circular polarisation modes, with the modes numbered by increased detuning from the Bragg wavelength and the circular polarisations grouped separately. $\varepsilon = 45°$ corresponds to a pure circular state.

Note that as the threshold gain of the lasing modes increases the circular purity of the modes decreases. This occurs because the index mismatch between the active central region and the passive regions increases with increased gain, which causes chirality reversing reflections and creates crosstalk between the two lasing mechanisms.

As a comparison, the lasing modes of the non-index matched structurally chiral laser with $\kappa L = 2.5$ have a maximum ε value of 20°. This shows that the polarisation state of the lasing modes of the hybrid chiral laser are far more pure circularly polarised. The ε values are very similar to those of a chiral distributed Bragg reflector laser for the left circular polarisation modes and those of an index matched structurally chiral laser for the right circular polarisation modes. The small differences are due to the boundary reflections at

high gain threshold feeding into the second lasing mechanism rather than into isotropic media.

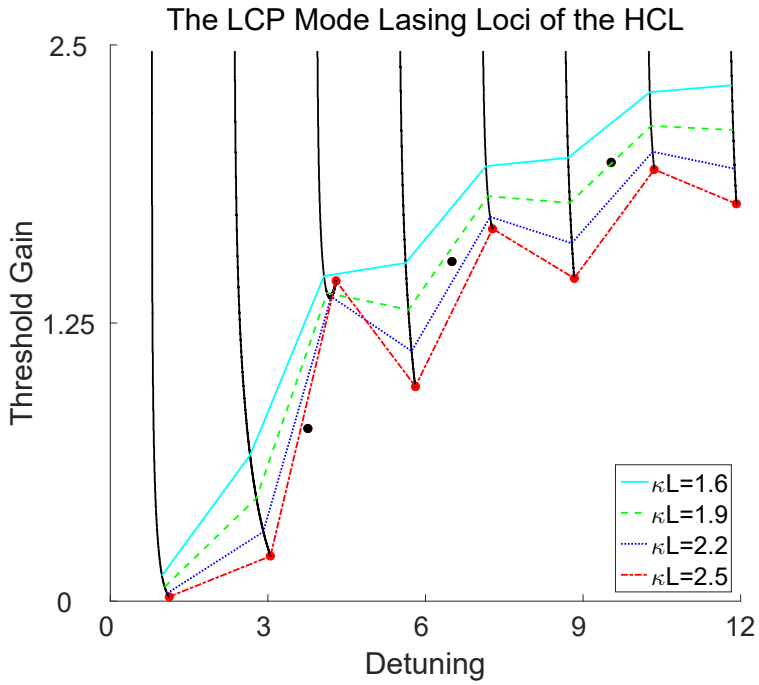

Figure 6.7: Chiral lasing loci plot for a hybrid chiral laser as the coupling constant κL in the passive regions approaches 0, plotted with respect to detuning ($\mathrm{Re}\,[\delta kL/2]$) and threshold gain ($\mathrm{Im}\,[\delta kL/2]$). Note that the left handed modes disappear and the hybrid chiral laser evolves into a right-handed index-matched structurally chiral laser.

In order to examine to what extent the two competing lasing mechanisms are decoupled we change the coupling constant κL, first in the passive regions and then in the active region. Decreasing κL in the passive regions weakens the left circular polarisation modes. We plot the created lasing loci in Figure 6.7. The right handed modes (black circles) are not affected. However, the left handed modes (red circles) move, requiring a higher gain threshold to lase. This happens because the coupling constant and thereby the reflectance of the passive regions is decreased. The modes disappear into the ridges identified in Figure 6.5 as $\kappa L \to 0$.

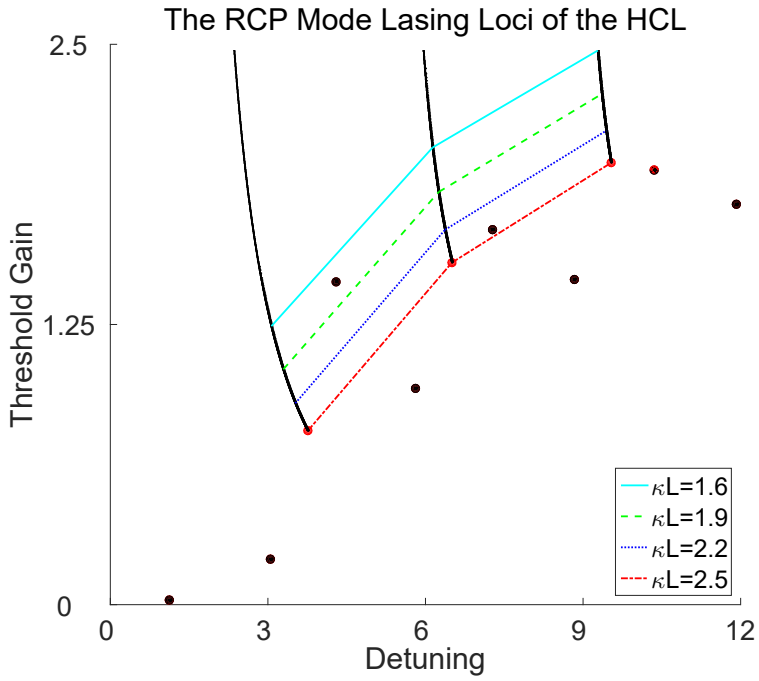

Figure 6.8: Chiral lasing loci plot for a hybrid chiral laser as the coupling constant κL in the active region approaches 0, plotted with respect to detuning ($\mathrm{Re}\,[\delta kL/2]$) and threshold gain ($\mathrm{Im}\,[\delta kL/2]$). Note that the right handed modes disappear and the hybrid chiral laser evolves into a chiral distributed Bragg reflector laser.

Figure 6.7 demonstrates that changing the coupling constant of the passive structure affects only the left-handed lasing modes, which shows that the right-handed modes are decoupled from the DBR lasing mechanism. In fact, any changes to the passive structurally chiral media sections that do not introduce boundary reflections will leave the right-handed lasing modes completely unaffected. This is a crucial benefit of the hybrid chiral laser, which we shall attempt to exploit in Section 7.

The same analysis can be conducted on the right handed modes by decreasing κL in the central active region of the hybrid chiral laser. The lasing loci are plotted in Figure 6.8, where the gain threshold of the right handed modes (red circles) increases as the coupling constant is decreased. The left-handed modes (black circles) are not affected, thereby demonstrating that the left-handed modes are decoupled from the distributed feedback mechanism. As before, we note that any changes to the active central structurally chiral medium that do not introduce boundary reflections will leave the left-handed modes unaffected. The decoupled nature of the two lasing mechanisms provides a degree of freedom that future designs may be able to exploit.

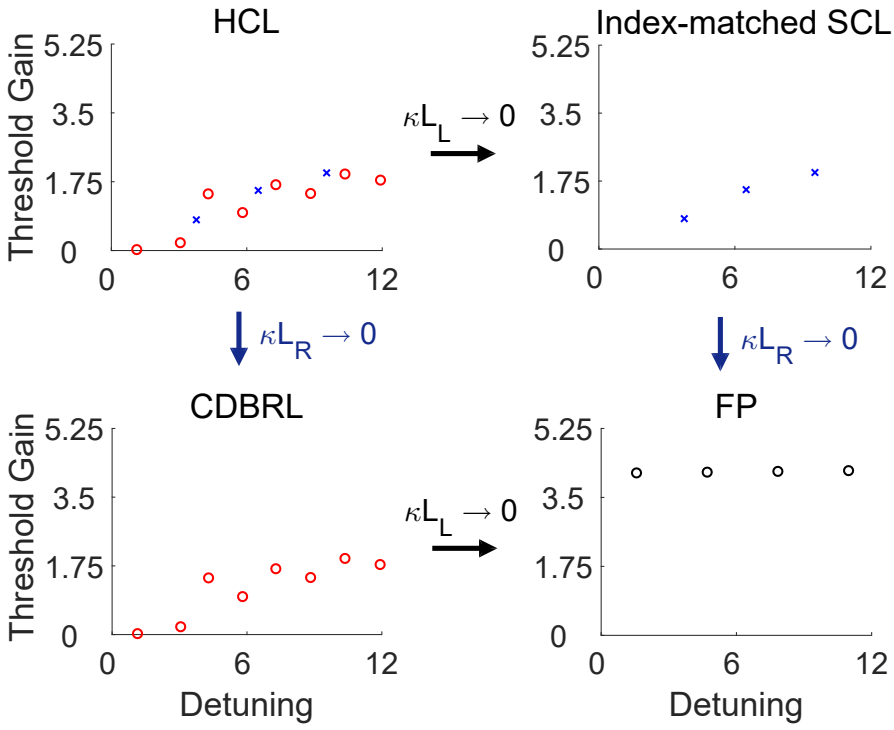

Figure 6.9: Evolution of lasing mode structure from a hybrid chiral laser to the conventional Fabry-Pérot laser as the coupling constants inside the passive structure or inside the active structure are reduced, plotted with respect to detuning ($\mathrm{Re}\,[\delta kL/2]$) and threshold gain ($\mathrm{Im}\,[\delta kL/2]$).

Once we have decreased the coupling inside the active region, decreasing the coupling in the passive region transforms the chiral distributed Bragg reflector laser into a purely Fabry-Pérot laser, as seen in Figure 6.3 previously. Similarly, decreasing the coupling in the active region after having turned off the coupling in the passive region transforms the index-matched structurally chiral laser into a purely Fabry-Pérot laser. These transitions are demonstrated in Figure 6.9.

Finally, we would like to look at the intracavity intensity envelopes, seen in Figure 6.10, to confirm our findings. There are indeed two fundamentally different types of intracavity intensity profiles. The right circular polarisation modes demonstrate a typical structurally chiral laser intracavity intensity profile in the central active region, with a constant gain profile in the passive left circular polarisation mirrors. The intensity profile is qualitatively similar to the 1_R, 2_R and 3_R lasing modes in Figure 5.3 and to the intracavity intensity envelopes for an index matched distributed feedback [3]. Thus, the right circular polarisation modes lase solely due to the distributed mechanism in the central region and are not

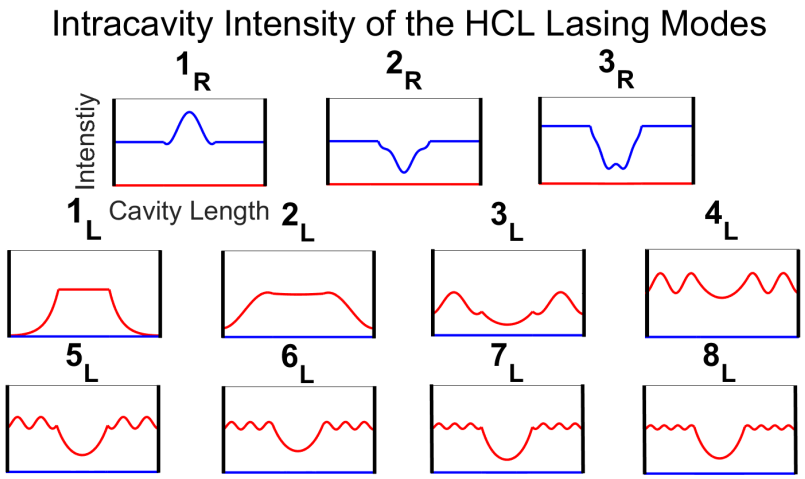

Figure 6.10: Intracavity intensity envelopes for the hybrid chiral laser lasing modes, arranged by polarisation type and increased detuning from the Bragg wavelength. The blue lines represent right circular polarisation while the red lines represent left circular polarisation.

affected by the left circular polarisation mirrors. In contrast, the left circular polarisation modes demonstrate the chiral distributed Bragg reflector laser intracavity intensity profile seen in Figure 6.4 in the central region.

In conclusion, we have shown that the hybrid chiral laser is a combination of the index-matched structurally chiral laser and the chiral distributed Bragg reflector laser. It has both pure left circular polarisation and right circular polarisation lasing modes and each family of lasing modes can be manipulated without affecting the other. In Chapter 7 we examine how one might potentially use the added freedom provided by the hybrid chiral laser.

Chapter 7

Potential Uses of Chiral Lasers

The analysis conducted in the previous chapters showcases the properties of three different chiral lasers. In this chapter we showcase two potential uses for some of the newly discovered properties for display technologies. These applications represent preliminary ideas as to how the chiral laser research can be applied in order to improve upon real devices used in commercial products today.

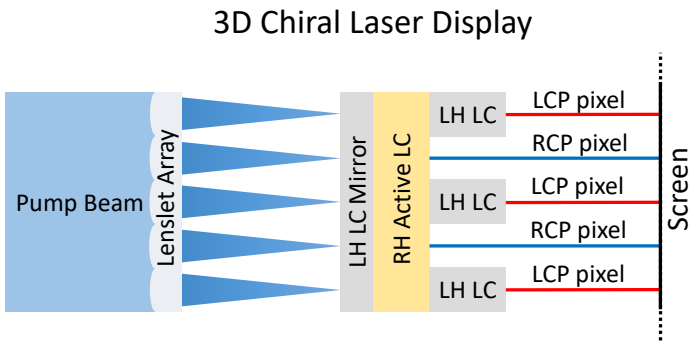

Figure 7.1: Schematic diagram for a three dimensional (3D) Chiral Laser Display. The pump beam passes through a lenslet array to create a pixel pattern. Each pixel hits a different area of the hybrid chiral laser. For half of the beams the hybrid chiral laser has no left handed liquid crystal (LH LC) mirror on the far side, so no chiral distributed Bragg reflector laser mode can exist and those pixels lase right circular polarisation. The other half lase the dominant left circular polarisation.

Let us consider Chiral Laser Pixels for use in three dimensional (3D) screens, depicted in Figure 7.1, which shows a pump beam incident to a lenslet array. This array focus the beam into a 2D lattice of concentrated pump beams. Each beam hits a different area on

the chiral laser set-up. The chiral laser set-up begins with a left-handed liquid crystal mirror, followed by a right-handed active liquid crystal layer. Both of these layers can be created as polymers for ease of manufacture. Onto these two layers an array of left-handed liquid crystal droplets/pieces can be applied, so that every second pixel from the pump beam hits one such liquid crystal droplet/piece. This completes the hybrid chiral laser, but only for every second pixel. The remainder of the pixels have no second, left-handed mirror, so none of the chiral distributed Bragg reflector laser modes are available to them. If we ensure that the chiral distributed Bragg reflector laser mode is the dominant lasing mode for the laser pixels which include the left-handed droplets, then we have a device which lases an array of right circular polarisation and left circular polarisation pixels onto a screen.

3D displays work by projecting two seperate images simultaneously, with one image being left circularly polarised and the other being right circularly polarised. The viewer then puts on glasses with a left circular polarisation filter as one lens and a right circular polarisation filter as the other lens. In this way each eye sees a different image. The images themselves depict the same scene, but are offset from each other in such a way that viewing one image with the left eye and the other with the right eye creates an illusion of depth and tricks the brain into believing that the displayed scene is three dimensional.

The pixel array described above can be used as a normal screen while the 3D effect is not desired, thereby providing full use of all the available pixels to create a high resolution image. When a 3D projection is desired the user can put on 3D glasses and the picture passed to the right circular polarisation pixels can be slightly shifted from that passed to the left circular polarisation pixels. Thus we have a device that works like a regular 2D screen until the 3D mode is activated and the glasses are put on.

Liquid crystals are used for all types of displays, from large TVs to compact cellphones. While the device described above may not be similar to current liquid crystal display configurations the ubiquity of liquid crystals in industry suggests that there may be a way to integrate such a device into a large TV or a gadget as small as a cellphone.

An alternative use for chiral lasers is in 3D projectors. Conventional 3D projectors use

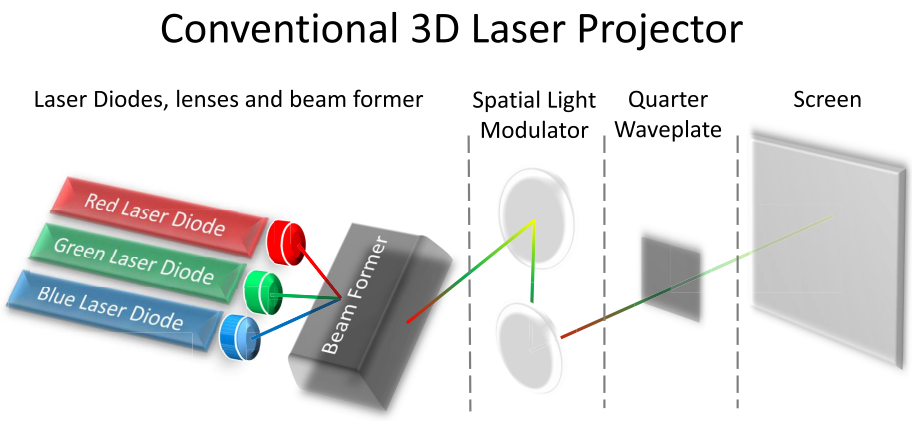

Figure 7.2: Schematic diagram of a conventional 3D laser projector.

a red, green and blue (RGB) laser diode in conjunction with a complicated lens array to combine the beams and form a given colour (see Figure 7.2). A spatial light modulator is then used to target a particular point on the screen and the laser light is passed through a quarter waveplate to become circularly polarised [73]. The apparatus is complicated, lossy, and therefore expensive, even after optimisation for commercial viability.

Using a structurally chiral laser the three laser diodes and the lens array used to create the coloured laser beam could be replaced. The structurally chiral laser can be tuned to any wavelength in the visible spectrum, thereby allowing for an even greater usable colour space than that provided by the RGB lasers. The spatial light modulator is needed by both set-ups in order to scan over the entirety of the screen. However, the quarter waveplate can be removed, as the structurally chiral laser laser output can be dynamically switched from one circular polarisation to another. This saves on the cost of the quarter waveplate, but it also removes the need to circularly polarise the laser output, thereby halving the loss. The positive benefits of a structurally chiral laser 3D projector are therefore the single laser source, fewer components, larger colour space, dynamic circular polarisation switching, no loss and increased efficiency.

However, there are a number of problems that need to be taken into account. Current structurally chiral lasers still need to be optically pulse pumped, which is impractical and needs to be overcome before commercial viability can be achieved for structurally chiral laser 3D projectors as well as for Chiral Laser pixels. If a non-index-matched structurally

chiral laser laser is used the output is not purely circular, so we would expect some loss. Alternatively, an hybrid chiral laser can be used, but switching between left circular polarisation and right circular polarisation using an electric field, on the left-handed mirror for instance, may not be quick enough. Indeed, the speed at which the projector needs to switch between circular polarisation states as well as wavelength necessitates a possibly prohibitive tuning speed and dynamic polarisation switching speed. Experiments will need to be conducted in order to test these ideas.

These are just some of the issues that will need to be addressed, but the idea of using structurally chiral lasers commercially for their dynamic circular polarisation switching, their cost effectiveness and their broad tunability is tantalising. There is a lot of research being conducted into improving the viability of chiral lasers for use in research, industry and commercial applications. The hope is that the added intricacies uncovered by our research, including the possibility of dynamic circular polarisation switching and lasing inside the photonic band-gap may give chiral lasers a new edge that will help in this endeavour.

Chapter 8

Further Research Avenues

8.1 Theoretical Research

The research conducted thus far has opened numerous possible research avenues, both theoretical and experimental. Perhaps the most pressing theoretical project is a stability analysis of the lasing modes in order to determine whether all the modes can lase stably. Intuitively, as both sets of modes come from well established, stable lasing mechanisms, they should be stable, but this statement needs to be verified rigorously. The band-edge mode has been demonstrated to be stable experimentally, however all the other modes have not been attained.

Even though chiral media have been studied for many years, the current understanding of the dynamics and propagation characteristics of light travelling through a chiral structure lag behind the understanding of the dynamics of many other systems. The most advanced modelling technique available for chiral media is the coupled wave theory approach used in this thesis, but this approach can't readily be adapted to dynamics, as it inherently assumes a static state for forward and backward propagating light. An alternative approach can be used in order to analyse the stability of the lasing modes. Consider a pulse travelling through the structure with coordinate $\xi = z - vt$. This pulse can be analysed using coupled wave theory by adapting the slowly varying envelope approximation to os-

cillations in time rather than space. In such a way a stability analysis of the modes might be possible, but this approach would need to be developed.

Alternatively, a fully dynamic analysis of a structurally chiral laser could be conducted. For such an analysis it would be necessary to combine coupled wave theory with directional techniques by splitting the Helmholtz equations into a forward and backward propagating component, but new theoretical and numerical tools would need to be generated. With these tools the research avenues discussed in the remainder of this section may be easier to conduct and new research avenues such as noise analysis can be investigated. The dynamic model could even be extended in order to model the quantum properties of chiral light, however a method other than coupled wave theory would have to be used.

Another direction in which the research presented in this thesis can be taken is towards improving the model. In Section 3.2 we make numerous assumptions that do not necessarily hold in experimental implementations of chiral laser devices.

Consider the laser pump, where we currently assume that pumping occurs homogeneously along the length of the active medium of our devices. In reality, longitudinal end pumping is often used, which implies gain attenuation along the cavity according to the Beer-Lambert law. One can introduce inhomogeneous pumping into the model through a change to the gain introduced in the refractive index, by sending $\mathrm{Im}\,(n) \rightarrow \mathrm{Im}\,(n)\exp\,(-z/L)$. This adjustment will create a more realistic model and provide an asymmetry to the system that could be exploited to target specific lasing modes or to further other desirable features. After a more realistic model for the pumping is introduced the pump intensity profile can be overlapped with the lasing mode intensity profiles. Comparing the two profiles can help optimise the laser with regards to minimising the threshold power and reducing dye bleaching.

It could prove beneficial to introduce a more realistic model for both loss and gain. As briefly mentioned in Section 5.2, we currently ignore loss and have a wavelength independent gain. In such a model it seems that the threshold energy needed for lasing decreases monotonically with respect to cavity length. Experiments conducted by Dr. Morris' group in Oxford suggest that this is not the case [74]. Introducing more realistic lasing models

for loss and gain will help us understand where the discrepancy occurs and find ways to optimise structurally chiral lasers to minimise the gain threshold. A first step towards a realistic model is introducing inhomogeneous pumping, as discussed above. Adding a negative constant imaginary part to the refractive index will then crudely model the losses. Once such a model has been developed it can be compared to experimental results and then refined [75].

If the pump profile is not constant throughout the structure, then it should be possible to optimise the dye distribution in structurally chiral lasers. The placement could be optimised for maximal gain or for minimal bleaching. Experimentally, the dye placement can be specified in dye doped liquid crystal polymers, so that any improvements to the model can be verified. For instance, it could be shown that placing the dye only where left circular polarisation is strongest targets the left circular polarisation modes.

A final suggestion towards improving the current model is considering a second dimension. Experimental results suggest that lasing can also occur transverse to the chiral structure of the laser [74]. To better understand the effect of off axis pumping and transverse lasing a two dimensional analysis is required.

There are numerous side projects that have emerged during the PhD. One such project would be to conduct a density of states calculation using coupled wave theory, which can be compared to other density of states calculations [75] in order to improve our understanding of band-edge lasing (1_R mode in the structurally chiral laser). Such an analysis could also explain how and why contra-handed lasing inside the photonic bandgap is possible.

Another project involves an investigation into the spatial and temporal coherence of chiral lasers with a particular focus on structural changes that could improve the coherences. It seems that a structurally chiral laser produces no speckle, but still has a narrow linewidth, which suggest a long coherence length.

Many structurally chiral lasers use an intracavity defect in order to lase, as these lasers can have even narrower linewidths than the band-edge structurally chiral lasers analysed in this thesis [76]. There are numerous different ways of adding such a defect [25], but

as a first step one could model a 90 degree twist in the pitch of the structurally chiral medium. Such a device has been studied by Kopp and Genack using a transfer matrix approach [16], but a coupled wave theory analysis may complement their research and reveal new insights. Particularly the lasing paths, which form an integral part of the coupled wave theory analysis, are not considered in the transfer matrix approach and are likely to provide a more intuitive understanding of the dynamics occurring due to the intracavity defect in the structurally chiral laser.

Another variation on the structurally chiral laser introduces a constant rate of change of rotation to the birefringent axis of the structurally chiral medium. While the model itself seems simple, it is difficult to analyse using coupled wave theory. An approach using Möbius transformations has been attempted and has proved promising, but further research is needed.

A further modelling project could examine a laser which uses an optically active gain medium. It should be possible to model the intracavity polarisation change due to optical activity. The lasing condition would then require two conditions: That the polarisation remain the same after one round trip, where the reflections are caused by mirrors at the boundaries, and that the intensity after one round trip remain the same. This added requirement will turn a Fabry-Pérot laser into a more complicated one. It could potentially help with mode locking, but it could also be very difficult to realise experimentally, as two conditions need to be fulfilled. A proper modal analysis would have to be conducted to see if such a laser is feasible.

Another avenue that lends itself to further research is varying the variables included in our model, thereby manipulating the lasing modes for desirable outcomes. The boundary reflections of a structurally chiral laser are currently equated. Changing them with respect to each other or strengthening them with respect to r_c will alter the lasing mode structure and may facilitate left circular polarisation lasing. Alternatively, realistic parameters from existing structurally chiral lasers can be inserted into the current model to model lasers that are already in operation. Comparing the predictions made by our theoretical model to the actual laser output should shed light on the accuracy of our model and suggest

areas of improvement that could be simple to implement and prove effective at reducing errors.

An intriguing link connects the research conducted on structurally chiral lasers in Part I with the research in Part II. The rotation used in the Oseen calculations in order to calculate an analytic solution for the electromagnetic field is essentially a map on the fields. As the fields are forms on a manifold, it may be possible to relate the rotation of the electric and magnetic fields to a diffeomorphism of the manifold. This would allow us to examine structurally chiral media from a transformation optics point of view using differential geometry, which would provide a new research methodology for studying structurally chiral lasers. Research we have conducted towards this goal has culminated in the development of a unique twisted medium, introduce in Section 13.4. While the twisted medium is not a structurally chiral medium as defined in Chapter 3, the links between the two fields of research are apparent. Further research may shed light on how far reaching the connections between the two media are.

8.2 Experimental Research

In conjunction to the numerous theoretical research opportunities there are a number of experimental directions in which our research can be taken. The three research projects that have already been discussed are demonstrating dynamic polarisation switching, trying to create chiral laser pixels and conducting a feasibility study for a 3D projector with a chiral laser source.

In order to demonstrate dynamic polarisation switching the very first step would be to demonstrate left circular polarisation lasing using a structurally chiral laser. One possible approach is to choose a dye and cholesteric liquid crystal combination so that the emission spectrum of the dye is within the photonic bandgap of the liquid crystal. An electric field could be used to tune the liquid crystals to the necessary wavelengths. It seems that a number of appropriate material choices exist that can be used to fabricate a liquid crystal laser [18]. Once the laser has been built the hope is that strong enough pulsed pumping

will achieve lasing. If this proves to be the case, then the lasing output and polarisation should be measured to verify that the lasing mode is indeed left circular polarisation and inside the photonic bandgap. The next step would be to tune the liquid crystal in order to shift the band-edge 1_R lasing mode into the emission spectrum of the dye. In doing so the 0_L left circular polarisation mode should no longer be in the emission spectrum and lasing should switch to the 1_R mode. Once this is demonstrated tuning the liquid crystals back should switch the laser to the 0_L mode and dynamic polarisation switching will have been demonstrated. Optimisation can then take place to increase the speed at which dynamic polarisation switching can occur.

Demonstrating dynamic polarisation switching is an ambitious project, as a number of assumptions have been made during our analysis that may prove problematic during construction. The approach suggested above may need to be modified as new insights become apparent. However, achieving dynamic polarisation switching is an enticing prospect and is perhaps the key challenge presented by the theoretical research of Part (I).

Both the 3D chiral laser pixels and the 3D chiral laser projector represent potential uses for which further development is needed. It is not currently possible to simply build the suggested designs and expect a functioning product. For the 3D chiral laser pixels the hybrid chiral laser needs to be better understood. The first step would be to build a hybrid chiral laser and characterise it in order to determine if it could be used in commercial products effectively. Once both right circular polarisation and left circular polarisation lasing have been demonstrated the polymerisation process would need to be tested in order to produce a mirror with varying thickness or pixels with a mirror and pixels without one. A method would then need to be found to create the pattern needed for a 3D chiral laser pixel array.

If the 3D chiral laser projector is to use a structurally chiral laser as its light source, then the dynamic polarisation switching has to be confirmed before any progress can be made. Once the dynamic polarisation switching is confirmed the next big challenge is the tuning speed. Most cinema projectors show 24 frames per second, with some movies being shown at 48 frames per second [77]. In order to use the structurally chiral laser for both circular polarisations it would be necessary to switch between the polarisation states at

twice that speed. Most projectors combine red, green and blue to create the right colour for each pixel. If the structurally chiral laser would be used to produce all three colours it would need to change between all three wavelengths. The structurally chiral laser would therefore need to either switch its lasing polarisation with 48Hz and its wavelength with 144Hz in order to lase $R_R G_R B_R R_L G_L B_L$ or switch its lasing polarisation with 144Hz and its wavelength with 72Hz in order to lase $R_R R_L G_R G_L B_R B_L$, where the letter represents the colour and the subscript represents the polarisation. If the structurally chiral laser could be tuned faster than 144Hz, then more colours become available and the colour space can be improved.

In commercial projectors there are far more sophisticated ways to achieve a 3D image and these would have to be taken into consideration, but the above calculation provides a ballpark at which the polarisation switching as well as the wavelength tuning would have to operate. If these are shown to be unrealistic, alternative approaches involving more lasers or a more sophisticated structurally chiral laser can be examined. It has been shown that a more sophisticated structurally chiral laser set-up combining numerous dyes can lase RGB [78]. Such a set-up could be developed upon so that depending on which wavelength the pump is operating at a different colour is produced. In such a way the wavelength tuning would become unnecessary.

The discussion above represents just some of the numerous ideas that arose while conducting the research into structurally chiral lasers. Discussions with experimentalists and theoreticians in the field continue to supply new and exciting directions in which the research can be taken. We hope the examples presented in this chapter provide a taste of where the research may go.

Part II

Transformation Theory

Chapter 9

Introduction to Part II

9.1 Mathematical Preliminaries

In Part II Maxwell's equations are presented and manipulated using the mathematical environment of differential geometry. As differential geometry is a rigorous and well understood area of mathematics it is important that the tools it provides are used correctly in order to insure that any conclusions drawn from the investigations will be valid. It is therefore necessary to define all used terms and concepts properly to ensure that when a differential 1-form is mentioned, it is indeed a differential 1-form and not something else. Luckily, the definitions, theorems and corresponding proofs have been excellently presented in many texts, such as [63, 79]. For completeness, all the definitions and theorems used in the following chapters are presented in italics when they are first used and defined in Appendix B.

Without loss of generality the units are chosen so that the speed of light $c = 1$ and the vacuum permeability and the vacuum permittivity $\mu_0 = \varepsilon_0 = 1$ in Cartesian coordinates. The Minkowski metric is taken as $\eta_{\mu\nu} = \text{diag}\,(-1, 1, 1, 1)$. Einstein summation notation is used throughout, so that Greek indices denote a range from 0 to 3 and Latin indices denote a range from 1 to 3. Three-component vectors are expressed in bold, differential forms as capital letters in italics, tensors with subscripts and superscripts, matrices with an underline and functions are introduced explicitly as maps $f : A \to \mathbb{R}$.

9.2 Motivation for the Presented Approach

In transformation optics, differential geometry can be used as a tool to find the necessary material parameters for devices that distort light in a predefined way. To do so it is very helpful to develop the covariant approach to Maxwell's equations in order to be able to manipulate the fields effectively on arbitrary *Manifolds* and for arbitrary coordinate systems.

The presented approach begins by deriving Maxwell's equations as regular vector equations as well as in covariant notation from Lagrangian considerations using the principle of least action. To do so the electric and magnetic potentials ϕ and $\mathbf{A}$ are introduced and the electric and magnetic fields $\mathbf{E}$ and $\mathbf{B}$ are derived from them. The potentials are combined into the 1-form known as the 4-potential A and the electromagnetic field tensor is derived from it as

$$F = \mathrm{d}A. \tag{9.1}$$

Finally, the electromagnetic field tensor is shown to incorporate the electric and magnetic field strengths.

Once the electromagnetic field tensor is identified, the first pair of Maxwell's equations is demonstrated to appear simply because F is an *exact form*:

$$\mathrm{d}F = \mathrm{d}^2 A = 0. \tag{9.2}$$

In order to derive the second pair of Maxwell's equations the action is modified by a term that takes the action of the fields into account. The second pair of Maxwell's equations are then calculated in covariant notation, which has not been done in existing literature. From these the second pair of Maxwell's equations are explicitly derived in their well known vector form.

In doing so the map $\chi : \Lambda^2(M) \to \Lambda^2(M)$ from F to the excitation tensor G is introduced. This map is important as it encodes the constitutive relations, from which the

necessary material parameters for a given transformation are derived. Its change under a transformation is the core of transformation optics.

Once the deformation of χ under a transformation is understood, the necessary permittivity and permeability (as well as the matrices allowing for magnetoelectric coupling) need to be extracted from it. It is therefore shown explicitly how the well known vector constitutive relations relate to χ.

The motivations to begin with such a fundamental approach stems from a desire for completeness as well as rigour. This approach has the added bonus of illuminating aspects of the underlying physics of Maxwell's equations as well as transformation optics that would otherwise not necessarily be considered. In addition, our research interests include developing Maxwell's equations using a Lagrangian that incorporates continuous media, for which the approach presented here is ideal.

After Maxwell's equations have been derived the remainder is a straightforward path towards developing the constitutive relations in covariant notation. The theory of transformation optics can then be presented in a concise, mathematically complete and beautiful manner.

This sets an ideal foundation for discussing our research, ensuring that the work is conducted within a solid and rigorous framework and any conclusions drawn follow directly from the work previously presented.

Such an approach allows for an earnest analysis of transformation optics, as all the preliminary definitions and concepts have been introduced. In Chapter 12 the theory of transformation optics is developed, concluding with Equation (12.40), from which the material parameters necessary to create a transformation device able to mimic any permissible transformation can be derived.

Finally, in Chapter 13 research towards the refractive index of reciprocal electromagnetic media is presented, which was conducted with Kinsler and McCall [4]. It is shown that reciprocal electromagnetic media $\left(\underline{\varepsilon} = \underline{\mu}\right)$ are completely described by a refractive index

$n(\mathbf{r}, \hat{\mathbf{s}})$, which depends on the position $\mathbf{r}$ and the direction $\hat{\mathbf{s}}$, but not on the polarisation. The refractive index is shown to be representable by an ellipsoidal phase surface.

We apply our discovery to the well known cylindrical cloak to demonstrate how it can be used for a better understanding of the cloak and in order to familiarise the reader with our methodology on a well known transformation optics device. We continue by introducing a new transformation, which creates a structurally chiral medium by way of a twist deformation. We analyse the transformation, establish its uniqueness from the structurally chiral medium introduced in Part I and suggest interesting uses for such a transformation optics device. We end by demonstrating, using a simple example, that electromagnetically reciprocal media in general do *not* preserve impedance, which raises questions as to the possibility of perfect transformation optics.

In conclusion, the theory of transformation optics is presented in a concise and rigorous fashion. From this foundation current research is introduced and its implications discussed.

Chapter 10

Covariant Representation of Maxwell's Equations

In 1904 Hendrik Lorentz published his theory on Lorentz transformations, which are transformations between two inertial frames [80]. Unlike Galilean transformations, they preserve the speed of light and insure that the laws of physics remain the same for all inertial observers. These are the postulates used by Albert Einstein to develop his theory of special relativity in 1905 [81].

Maxwell's equations can be expressed in an alternate notation known as covariant notation, in which they remain invariant under Lorentz transformations. This insures that Maxwell's equations do not depend on the inertial frame of reference chosen for a given calculation and allows us to easily translate the electromagnetic fields from one inertial frame to another. The same can not be said for the standard vector notation of Maxwell's equations and it is for this reason that the covariant approach is chosen in the following chapters.

In developing the covariant Maxwell's equations we begin with Lagrange formalism and the principle of least action. We develop Maxwell's equations in standard vector notation and in covariant notation in parallel in order to demonstrate that they are the same equations, and provide insight into how the covariant representation arises.

An alternate approach would be to begin with the axioms concerning conservation laws,

mechanical forces etc. as done by Hehl and Obukhov [61]. Such an approach is perhaps more physically meaningful, but it is more cumbersome, longer and loses the intrinsic beauty of the Lagrangian formalism. The results, of course, are the same.

We begin by considering the action of a charged particle moving through an electromagnetic field. Following the derivation in [62], we present the equations of motion for a charged particle and find the electric and magnetic field strengths in terms of the potentials. From there we continue by finding Maxwell's equations and construct the covariant representation of Maxwell's equations.

10.1 The Electric and Magnetic Field Strengths in Terms of the Potentials

The action of a charged particle moving through an electromagnetic field consists of two terms, where the first term is responsible for the free movement of the particle and the second term is responsible for the particle's interaction with the field:

$$\mathcal{S} = \mathcal{S}_{free} + \mathcal{S}_{interaction}. \tag{10.1}$$

The value of the action for a free moving particle must be independent of the choice of reference system, so the integrand must be a scalar. The action must therefore be of the form

$$\mathcal{S}_{free} = -\int_a^b \alpha \mathrm{d}s \tag{10.2}$$

where α is a positive scalar constant, $\mathrm{d}s^2 = g_{\mu\nu}\mathrm{d}x^\mu \mathrm{d}x^\nu$ and the integral $\int_a^b$ is along the world line of the particle between two given world points of the particle. The negative sign is included in order to ensure that a minima for the action exits when the world points are arbitrarily close, as is required by the principle of least action. $\mathcal{S}_{free}$ can be rewritten as a time integral

$$\mathcal{S}_{free} = \int_{t_1}^{t_2} L \mathrm{d}t, \tag{10.3}$$

where

$$L = -\alpha\sqrt{1-\mathbf{v}^2} \tag{10.4}$$

and we use the fact that $c = 1$ and that

$$\mathrm{d}s = \mathrm{d}t\sqrt{1-\mathbf{v}^2} \tag{10.5}$$

with

$$\mathbf{v}^2 = \left|\frac{\mathrm{d}x^i}{\mathrm{d}t}\right| \leq 1. \tag{10.6}$$

To find α we can approximate

$$L \approx -\alpha + \frac{\alpha v^2}{2} \tag{10.7}$$

and remember that the constant term does not affect the equations of motion. Comparing the approximation to the classical Lagrangian $L_{classical} = mv^2/2$ we see that $\alpha = m$ where m is the mass of the particle. Therefore

$$\mathcal{S}_{free} = -m\int_a^b \mathrm{d}s. \tag{10.8}$$

The action for the particle's interaction with the field must contain terms characterising the particle and terms characterising the field. Experimental findings indicate that the particle is characterised by its charge e. We define the electric potential ϕ and magnetic potential $\mathbf{A}$ as the terms encoding the field and combine them into a 1-form known as the four-potential $A = A_\mu \mathrm{d}x^\mu$. We then have that

$$\mathcal{S}_{interaction} = -\int_a^b eA_\mu \mathrm{d}x^\mu = -\int_a^b eA \tag{10.9}$$

The action is therefore given as [62]

$$\mathcal{S} = -\int_a^b m\mathrm{d}s - \int_a^b eA. \tag{10.10}$$

Switching to Minkowski coordinates we can write $A_\mu = (\phi, -\mathbf{A})$ in order to rewrite the

action as a time integral:

$$\begin{aligned}\mathcal{S} &= \int_a^b -m\mathrm{d}s - \int_a^b eA_\mu \mathrm{d}x^\mu \\ &= \int_{t_1}^{t_2} -m\sqrt{1-\mathbf{v}^2}\mathrm{d}t + \int_{x_1^i}^{x_2^i} e\mathbf{A}\cdot\mathrm{d}\mathbf{r} - \int_{t_1}^{t_2} e\phi \mathrm{d}t \\ &= \int_{t_1}^{t_2} \left(-m\sqrt{1-\mathbf{v}^2} + e\mathbf{A}\cdot\mathbf{v} - e\phi\right)\mathrm{d}t. \end{aligned} \tag{10.11}$$

The Lagrangian is therefore

$$L = -m\sqrt{1-\mathbf{v}^2} + e\mathbf{A}\cdot\mathbf{v} - e\phi \tag{10.12}$$

and we can now use the Euler-Lagrange equations to find the equations of motion. Note that we have previously chosen Minkowski coordinates, so that we are now operating in the regime of classical electrodynamics with regards to the fields.

We have that

$$\begin{aligned}\frac{\partial L}{\partial \mathbf{v}} &= \frac{m\mathbf{v}}{\sqrt{1-\mathbf{v}^2}} + e\mathbf{A} \\ &= \mathbf{p} + e\mathbf{A}, \end{aligned} \tag{10.13}$$

$$\begin{aligned}\frac{\partial L}{\partial \mathbf{r}} &= \nabla L \\ &= e\nabla\left(\mathbf{A}\cdot\mathbf{v}\right) - e\nabla\phi \\ &= e\left[\mathbf{v}\cdot\nabla\mathbf{A} + \mathbf{v}\times\left(\nabla\times\mathbf{A}\right) - \nabla\phi\right], \end{aligned} \tag{10.14}$$

where we use the vector identity $\nabla\left(\mathbf{A}\cdot\mathbf{B}\right) = \mathbf{B}\cdot\nabla\mathbf{A} + \mathbf{B}\times\left(\nabla\times\mathbf{A}\right)$ We now use that

$$\frac{\mathrm{d}\mathbf{A}}{\mathrm{d}t}\mathrm{d}t = \frac{\partial\mathbf{A}}{\partial t}\mathrm{d}t + \left(\mathrm{d}\mathbf{r}\cdot\nabla\right)\mathbf{A} \tag{10.15}$$

to write

$$\begin{aligned}\frac{\mathrm{d}}{\mathrm{d}t}\left(\frac{\partial L}{\partial \mathbf{v}}\right) &= \frac{\mathrm{d}}{\mathrm{d}t}\left(\mathbf{p}+e\mathbf{A}\right)\\ &= \frac{\mathrm{d}}{\mathrm{d}t}\mathbf{p}+e\frac{\partial \mathbf{A}}{\partial t}+e\left(\frac{\mathrm{d}\mathbf{r}}{\mathrm{d}t}\cdot\nabla\right)\mathbf{A}\\ &= \frac{\mathrm{d}}{\mathrm{d}t}\mathbf{p}+e\frac{\partial \mathbf{A}}{\partial t}+e\left(\mathbf{v}\cdot\nabla\right)\mathbf{A}, \end{aligned} \tag{10.16}$$

so that from the Euler-Lagrange equations we find that the equation of motion of a particle in an electromagnetic field is

$$\begin{aligned}&\frac{\mathrm{d}}{\mathrm{d}t}\left(\frac{\partial L}{\partial \mathbf{v}}\right)=\frac{\partial L}{\partial \mathbf{r}}\\ \Longrightarrow\quad &\frac{\mathrm{d}\mathbf{p}}{\mathrm{d}t}=e\left[-\frac{\partial \mathbf{A}}{\partial t}-\nabla\phi\right]+e\mathbf{v}\times\left(\nabla\times\mathbf{A}\right), \end{aligned} \tag{10.17}$$

where $\mathbf{p}$ is the momentum of the particle [62]. The change in momentum with respect to time (left hand side of Equation (10.17)) equals the force exerted on the particle. We can therefore identify the right hand side of Equation (10.17) with the different forces felt by the particle.

A force per unit charge called the *electric field strength* $\mathbf{E}$ is introduced for the first term in Equation (10.17). The second term is rewritten by introducing the *magnetic field strength* $\mathbf{B}$, which is proportional and perpendicular to the velocity of the particle. They are defined as

$$\mathbf{E} = -\frac{\partial}{\partial t}\mathbf{A}-\nabla\phi, \tag{10.18}$$

$$\mathbf{B} = \nabla\times\mathbf{A}, \tag{10.19}$$

and the equation of motion is rewritten as

$$\frac{\mathrm{d}\mathbf{p}}{\mathrm{d}t}=e\left(\mathbf{E}+\mathbf{v}\times\mathbf{B}\right), \tag{10.20}$$

where the right hand side is known as the *Lorentz force.*

Note that the field strengths, not the potentials, define the equations of motion and

that the field strengths only depend on derivatives of the potentials. A gauge invariance therefore exists, so that $\mathbf{A}$ and ϕ can be replaced by

$$\mathbf{A}' = \mathbf{A} + \nabla f, \tag{10.21}$$

$$\phi' = \phi - \frac{1}{c}\frac{\partial}{\partial t} f, \tag{10.22}$$

for any differentiable function f. The freedom of choice of f implies that the potentials can always be chosen so that $\phi = 0$.

10.2 The Electromagnetic Field Tensor in Terms of the Potentials

In a similar vein to Section 10.1 we can calculate the equations of motion from the action while remaining in covariant notation [62]. We begin with the principle of least action to write that

$$\begin{aligned} \delta\mathcal{S} &= -\delta \int_a^b (m\mathrm{d}s + eA) = 0 \\ &= -\int_a^b \left(m\frac{\mathrm{d}x_\mu \mathrm{d}\delta x^\mu}{\mathrm{d}s} + eA_\mu \mathrm{d}\delta x^\mu + e\delta A_\mu \mathrm{d}x^\mu \right), \end{aligned} \tag{10.23}$$

where we use the fact that $\mathrm{d}s = \sqrt{\mathrm{d}x_\mu \mathrm{d}x^\mu}$.

In Equation (10.23) integration by parts can be used to rewrite the first two terms. We define the four velocity $u = u_\mu \mathrm{d}x^\mu$ with $u_\mu = \mathrm{d}x_\mu/\mathrm{d}s$ and rewrite the first two terms as

$$\begin{aligned} & -\int_a^b m\frac{\mathrm{d}x_\mu \mathrm{d}\delta x^\mu}{\mathrm{d}s} + eA_\mu \mathrm{d}\delta x^\mu \\ = & -\int_a^b (mu_\mu + eA_\mu)\, \mathrm{d}\delta x^\mu \\ = & -\left[(mu_\mu + eA_\mu)\, \delta x^\mu\right]_a^b + \int_a^b (m\mathrm{d}u_\mu + e\mathrm{d}A_\mu)\, \delta x^\mu. \end{aligned} \tag{10.24}$$

The first term equals 0 as $\delta x^\mu|_a = \delta x^\mu|_b$, so we can write

$$\begin{aligned}
\delta\mathcal{S} &= -\int_a^b \left(m\frac{\mathrm{d}x_\mu \mathrm{d}\delta x^\mu}{\mathrm{d}s} + eA_\mu \mathrm{d}\delta x^\mu + e\delta A_\mu \mathrm{d}x^\mu \right) \\
&= \int_a^b m\mathrm{d}u_\mu \delta x^\mu + e\mathrm{d}A_\mu \delta x^\mu - e\delta A_\mu \mathrm{d}x^\mu \\
&= \int_a^b m\mathrm{d}u_\mu \delta x^\mu + e\partial_\nu A_\mu \mathrm{d}x^\nu \delta x^\mu - e\partial_\nu A_\mu \delta x^\nu \mathrm{d}x^\mu \\
&= \int_a^b m\mathrm{d}u_\mu \delta x^\mu - e\left(\partial_\mu A_\nu - \partial_\nu A_\mu\right)\mathrm{d}x^\nu \delta x^\mu \\
&= \int_a^b \left[m\mathrm{d}u_\mu - e\left(\partial_\mu A_\nu - \partial_\nu A_\mu\right)\mathrm{d}x^\nu\right]\delta x^\mu \\
&= \int_a^b \left[m\frac{\mathrm{d}u_\mu}{\mathrm{d}s} - e\left(\partial_\mu A_\nu - \partial_\nu A_\mu\right)u^\mu\right]\delta x^\mu \mathrm{d}s = 0, \qquad (10.25)
\end{aligned}$$

where $\partial_\mu = \partial/\partial x^\mu$ and we use integration by part to get from the third to the fourth line in the calculation.

Equation (10.25) needs to hold for arbitrary variations, so that

$$m\frac{\mathrm{d}u_\mu}{\mathrm{d}s} - e\left(\partial_\mu A_\nu - \partial_\nu A_\mu\right)u^\mu = 0 \qquad (10.26)$$

must hold.

We define the *electromagnetic field tensor* F as

$$\begin{aligned}
F &= \mathrm{d}A \\
&= \mathrm{d}\left(A_\nu \mathrm{d}x^\nu\right) \\
&= \partial_\mu A_\nu \mathrm{d}x^\mu \wedge \mathrm{d}x^\nu \\
&= \frac{1}{2}\left(\partial_\mu A_\nu - \partial_\nu A_\mu\right)\mathrm{d}x^\mu \wedge \mathrm{d}x^\nu \\
&= \frac{1}{2}F_{\mu\nu}\mathrm{d}x^\mu \wedge \mathrm{d}x^\nu, \qquad (10.27)
\end{aligned}$$

as $\mathrm{d}x^\mu \wedge \mathrm{d}x^\nu = -\mathrm{d}x^\nu \wedge \mathrm{d}x^\mu$ (the *wedge product* $\wedge$, the *exterior derivative* d and the *partial differential operator* ∂_μ are defined in Appendix B). We can therefore rewrite Equation (10.26) as

$$m\frac{\mathrm{d}u_\mu}{\mathrm{d}s} = eF_{\mu\nu}u^\nu, \qquad (10.28)$$

which is the equation of motion of a particle moving in an electromagnetic field, but this time in covariant form.

10.3 Identifying the Electromagnetic Field Tensor with the Electric and Magnetic Field Strengths

By choosing a coordinate system and setting we can calculate the components of F individually. We find that

$$\begin{aligned} F_{\mu\mu} &= 0, && (10.29)\\ F_{\mu\nu} &= -F_{\nu\mu}, && (10.30)\\ F_{0i} &= -\frac{\partial}{\partial t}\mathrm{A}_i - \frac{\partial}{\partial x^i}\phi \\ &= \mathrm{E}_i, && (10.31)\\ F_{ij} &= \frac{\partial}{\partial x^j}\mathrm{A}_i - \frac{\partial}{\partial x^i}\mathrm{A}_j \\ &= \epsilon_{ijk}\left[\nabla \times \mathbf{A}\right]_k \\ &= \epsilon_{ijk}\mathrm{B}_k, && (10.32) \end{aligned}$$

where ϵ_{ijk} is the totally antisymmetric tensor. We can represent F in matrix form as

$$F_{\mu\nu} = \begin{pmatrix} 0 & -\mathrm{E}_x & -\mathrm{E}_y & -\mathrm{E}_z \\ \mathrm{E}_x & 0 & \mathrm{B}_z & -\mathrm{B}_y \\ \mathrm{E}_y & -\mathrm{B}_z & 0 & \mathrm{B}_x \\ \mathrm{E}_z & \mathrm{B}_y & -\mathrm{B}_x & 0 \end{pmatrix}. \qquad (10.33)$$

This demonstrates that the electric and magnetic field strengths are completely encoded in the electromagnetic field tensor F. It is also clear that as the four-potential A is a *1-form*, $F = \mathrm{d}A$ must be a *2-form*. We can now manipulate F as we wish using differential geometry while remaining certain that we have the field strengths encoded in it, thereby manipulating them appropriately as well.

As seen in [63, 79] and other reference texts, the divergence, curl and gradient are all

particular examples of the exterior derivative. More precisely, in $\mathbb{R}^3$ the gradient is the exterior derivative taking functions to 1-forms, the curl is the exterior derivative taking 1-forms to 2-forms and the divergence is the exterior derivative taking 2-forms to 3-forms.

If we examine Maxwell's equations (3.2)-(3.5) we see that **E** can be interpreted as a 1-form and **B** can be interpreted as a 2-form. In fact, choosing the dual basis ($\mathrm{d}t$, $\mathrm{d}x$, $\mathrm{d}y$, $\mathrm{d}z$) we can write

$$E = E_x \mathrm{d}x + E_y \mathrm{d}y + E_z \mathrm{d}z, \tag{10.34}$$

$$B = B_x \mathrm{d}y \wedge \mathrm{d}z + B_y \mathrm{d}z \wedge \mathrm{d}x + B_z \mathrm{d}x \wedge \mathrm{d}y, \tag{10.35}$$

$$F = B + E \wedge \mathrm{d}t. \tag{10.36}$$

10.4 The First Pair of Maxwell's Equations

The first pair of Maxwell's equations can now be derived in vector notation and in covariant form in order to demonstrate their agreement with each other. Taking the curl of Equation (10.18) and using the fact that the curl of a gradient is identically zero one finds using Equation (10.19) that

$$\nabla \times \mathbf{E} = -\frac{\partial}{\partial t}\mathbf{B}. \tag{10.37}$$

Taking the divergence of Equation (10.19) and using the fact that the divergence of a curl is identically zero one finds that

$$\nabla \cdot \mathbf{B} = 0. \tag{10.38}$$

The are the first two Maxwell's equations.

The rules that were just used are specific cases of the general rule for exterior derivatives, which states that taking the exterior derivative twice is identically zero:

$$\mathrm{d}^2 = 0. \tag{10.39}$$

Alternatively and more simply one can write

$$\mathrm{d}F = \mathrm{d}^2 A = 0, \tag{10.40}$$

which expresses the first pair of Maxwell's equations in covariant notation.

To see that these are identical one writes

$$\begin{aligned} \mathrm{d}F &= \mathrm{d}\left(B + E \wedge \mathrm{d}t\right) \\ &= \mathrm{d}B + \mathrm{d}E \wedge \mathrm{d}t \\ &= \mathrm{d}_S B + \mathrm{d}t \wedge \partial_t B + (\mathrm{d}_S E + \mathrm{d}t \wedge \partial_t E) \wedge \mathrm{d}t \\ &= \mathrm{d}_S B + (\mathrm{d}_S E - \partial_t B) \wedge \mathrm{d}t, \end{aligned} \tag{10.41}$$

where

$$\mathrm{d}_S \omega = \partial_i \omega_I \mathrm{d}x^i \wedge \mathrm{d}x^I \tag{10.42}$$

is the spatial part of the exterior derivative of a form and a summation over a capital letter represents a range. In the above calculation we use the fact that both B and E are not dependent on $\mathrm{d}t$ to separate out the spatial part of the exterior derivative.

We therefore recover

$$\mathrm{d}_S B = 0 \leftrightarrow \nabla \cdot \mathbf{B} = 0 \quad , \quad \mathrm{d}_S E - \partial_t B = 0 \leftrightarrow \nabla \times \mathbf{E} - \frac{\partial}{\partial t}\mathbf{B} = 0. \tag{10.43}$$

We can now see that the first pair of Maxwell's equations come directly from the properties of the exterior derivative. The electromagnetic field tensor is an exact form, as it is the exterior derivative of the potential and therefore its exterior derivative must equal zero.

10.5 The Action of the Electromagnetic Field and the Second Pair of Maxwell's Equations

The action in Equation (10.10), which gave us the equation of motion of a charged particle moving through an electromagnetic field, assumed the fields to be given and varied only the path of the particle. To find the field equations the particles, their charges and their motion are assumed to be given and only the potentials (and their first derivatives) are varied in order to solve the minimisation problem.

In order to account for the properties of the field itself a term needs to be added to the action, which depends on the fields alone. The dual of the electromagnetic field $\star F$ is needed, which, if flat spacetime with the Minkowski metric is assumed and a basis of 1-forms $(\mathrm{d}t, \mathrm{d}x, \mathrm{d}y, \mathrm{d}z)$ is chosen, can be written explicitly as

$$\star F_{\mu\nu} = \begin{pmatrix} 0 & \mathrm{B}_x & \mathrm{B}_y & \mathrm{B}_z \\ -\mathrm{B}_x & 0 & \mathrm{E}_z & -\mathrm{E}_y \\ -\mathrm{B}_y & -\mathrm{E}_z & 0 & \mathrm{E}_x \\ -\mathrm{B}_z & \mathrm{E}_y & -\mathrm{E}_x & 0 \end{pmatrix}, \tag{10.44}$$

where $\star$ is the *Hodge star operator*, defined in Definition B.33 as taking a form to its dual. On a 4 dimensional manifold it takes a 2-form to another 2-form.

The correct addition to the action to account for the field properties is given by [64]

$$\mathcal{S}_f = \frac{1}{2}\int \star F \wedge F. \tag{10.45}$$

All charges need to be taken into account, so that a summation must be introduced into Equation (10.10). The total action then becomes

$$\mathcal{S} = -\Sigma \int m\mathrm{d}s - \Sigma \int eA + \frac{1}{2}\int \star F \wedge F. \tag{10.46}$$

As the potentials are not in the first part of the action they will not change during the

variation, so the first term of the action can be dropped and only

$$\mathcal{S} = -\Sigma \int eA + \frac{1}{2}\int \star F \wedge F \tag{10.47}$$

needs to be considered.

Consider the *charge density*

$$\rho = \Sigma_i e_i \delta\left(\mathbf{r} - \mathbf{r}_a\right), \tag{10.48}$$

where $\delta(x)$ is the Dirac delta function, which is a continuous function that sums over all the charges. The total charge contained in a volume $\mathrm{d}V$ is then given by $\int \rho \mathrm{d}V$ and is an invariant quantity. We can replace the summation over the charges in the first term of Equation (10.47) with the integral over the whole volume $\rho \mathrm{d}V$ to find that

$$\begin{aligned}
\mathcal{S} &= -\int \rho \mathrm{d}V \wedge A + \frac{1}{2}\int \star F \wedge F \\
&= -\int \rho A_\mu \mathrm{d}V \wedge \mathrm{d}x^\mu + \frac{1}{2}\int \star F \wedge F \\
&= -\int \rho \frac{\mathrm{d}x^\mu}{\mathrm{d}t} A_\mu \mathrm{d}V \wedge \mathrm{d}t + \frac{1}{2}\int \star F \wedge F.
\end{aligned} \tag{10.49}$$

Defining the 1-form J as

$$\begin{aligned}
J &= \rho \frac{\mathrm{d}x_i}{\mathrm{d}t}\mathrm{d}x^i - \rho \mathrm{d}t \\
&= \mathrm{J}_i \mathrm{d}x^i - \rho \mathrm{d}t
\end{aligned} \tag{10.50}$$

where J_i are the components of the dual of the *current density vector* $\mathbf{J} = \rho\mathbf{v}$, we can take the Hodge dual of J to create a 3-form and use it to write the action as

$$\begin{aligned}
\mathcal{S} &= -\int \rho \frac{\mathrm{d}x^\mu}{\mathrm{d}t} A_\mu \mathrm{d}V \wedge \mathrm{d}t + \frac{1}{2}\int \star F \wedge F \\
&= \int \rho \frac{\mathrm{d}x^\mu}{\mathrm{d}t} A_\mu \mathrm{d}t \wedge \mathrm{d}V + \frac{1}{2}\int \star F \wedge F \\
&= \int \left[\star J\right]_{\alpha\beta\gamma} A_\mu \mathrm{d}x^\alpha \wedge \mathrm{d}x^\beta \wedge \mathrm{d}x^\gamma \wedge \mathrm{d}x^\mu + \frac{1}{2}\int \star F \wedge F \\
&= \int \left[\star J \wedge A + \frac{1}{2} \star F \wedge F\right].
\end{aligned} \tag{10.51}$$

The principle of least action can now be applied in order to compute Maxwell's equations in terms of differential forms. The author is not aware of a coordinate free representation of this result. Both $\star J \wedge A$ and $\frac{1}{2} \star F \wedge F$ are 4-forms, so they form a suitable Lagrangian

$$L = \star J \wedge A + \frac{1}{2} \star F \wedge F. \tag{10.52}$$

According to the principle of least action $\delta \mathcal{S} = \int \delta L = 0$, where we vary with respect to A and its derivatives only.

$$\begin{aligned}
\int \delta L &= \int \star J \wedge \delta A + \frac{1}{2} \delta \left(\star F \wedge F \right) \\
&= \int \star J \wedge \delta A + \frac{1}{2} \left(\star F \wedge \delta F + \delta \left(\star F \right) \wedge F \right) \\
&= \int \star J \wedge \delta A + \frac{1}{2} \left(\star F \wedge \delta F + \star \delta F \wedge F \right) \\
&= \int \star J \wedge \delta A + \frac{1}{2} \left(- \left[\langle F, \delta F \rangle + \langle \delta F, F \rangle \right] \mathrm{vol} \right) \\
&= \int \star J \wedge \delta A + \frac{1}{2} \left(-2 \langle F, \delta F \rangle \, \mathrm{vol} \right) \\
&= \int \star J \wedge \delta A + \star F \wedge \delta F \\
&= \int \star J \wedge \delta A + \star F \wedge \delta \mathrm{d} A \\
&= \int \star J \wedge \delta A + \star F \wedge \mathrm{d} \delta A,
\end{aligned} \tag{10.53}$$

where we use the facts that δ and $\star$ commute, the wedge product is antisymmetric, the inner product is symmetric, the definition of the Hodge star operator B.33 and that δ and d commute.

Integrating the second term by parts we can write

$$\begin{aligned}
\delta \mathcal{S} &= \int \star J \wedge \delta A + \star F \wedge \mathrm{d} \delta A \\
&= \int \left(\star J \wedge \delta A - \mathrm{d} \star F \wedge \delta A \right) + \left[\star F \wedge \delta A \right]_a^b \\
&= \int \left(\star J - \mathrm{d} \star F \right) \wedge \delta A = 0,
\end{aligned} \tag{10.54}$$

where we use the fact that δA is fixed at the limits of the integration.

In order for Equation (10.54) to hold we must have

$$\star J = \mathrm{d} \star F, \tag{10.55}$$

as the variation in A is arbitrary. We can apply the Hodge dual $\star$ to both sides of Equation (10.55) and use the fact that [63]

$$\star^2 = (-1)^{p(4-p)+1} \tag{10.56}$$

where the Hodge dual is operating on a p-form to rewrite Equation (10.55) as

$$\star \, \mathrm{d} \star F = \star^2 J = J, \tag{10.57}$$

which is the equation incorporating the second pair of Maxwell's equations.

To see this more clearly one writes out $\star F$ in differential form notation as

$$\begin{aligned} \star F &= \star (B + E \wedge \mathrm{d}t) \\ &= \star B + \star (E \wedge \mathrm{d}t) \\ &= -B_i \mathrm{d}x^i \wedge \mathrm{d}t + \frac{1}{2} \epsilon_{ijk} E_i \mathrm{d}x^j \wedge \mathrm{d}x^k \\ &= \star_S E - (\star_S B) \wedge \mathrm{d}t, \end{aligned} \tag{10.58}$$

where we make use of the spatial Hodge dual $\star_s$, which operates on the spatial submanifold only [63]. For clarity the two terms in Equation (10.58) are presented explicitly:

$$\star_S E = E_x \mathrm{d}y \wedge \mathrm{d}z + E_y \mathrm{d}z \wedge \mathrm{d}x + E_x \mathrm{d}x \wedge \mathrm{d}y, \tag{10.59}$$

$$\star_S B = B_x \mathrm{d}x + B_y \mathrm{d}y + B_z \mathrm{d}z. \tag{10.60}$$

$\mathrm{d} \star F$ can then be written as

$$\begin{aligned} \mathrm{d} \star F &= \mathrm{d} \star_S E - \mathrm{d} (\star_S B \wedge \mathrm{d}t) \\ &= \mathrm{d}t \wedge \partial_t \star_S E + \mathrm{d}_S \star_S E - \mathrm{d}_S (\star_S B \wedge \mathrm{d}t) . \end{aligned} \tag{10.61}$$

Finally,

$$\begin{aligned} \star \mathrm{d} \star F &= \star \left[\mathrm{d}t \wedge \partial_t \star_S E + \mathrm{d}_S \star_S E - \mathrm{d}_S \left(\star_S B \wedge \mathrm{d}t \right) \right] \\ &= -\partial_t E - \left[\star_S \mathrm{d}_S \star_S E \right] \mathrm{d}t + \star_S \mathrm{d}_S \star_S B. \end{aligned} \tag{10.62}$$

We therefore have that [63]

$$-\partial_t E - \left[\star_S \mathrm{d}_S \star_S E \right] \mathrm{d}t + \star_S \mathrm{d}_S \star_S B = J \tag{10.63}$$

and by equating like terms we find that

$$\left[\star_S \mathrm{d} \star_S E \right] = \rho, \tag{10.64}$$

$$\star_S \mathrm{d}_S \star_S B - \partial_t E = \mathbf{J}. \tag{10.65}$$

Remembering that the exterior derivative is a generalisation of the divergence, gradient and curl we can interpret Equations (10.64) and (10.65) as the second pair of Maxwell's vacuum equations:

$$\star_S \mathrm{d} \star_S E = \rho \quad \leftrightarrow \quad \nabla \cdot \mathbf{E} = \rho, \tag{10.66}$$

$$\star_S \mathrm{d}_S \star_S B - \partial_t E = \mathbf{J} \quad \leftrightarrow \quad \nabla \times \mathbf{B} - \frac{\partial \mathbf{E}}{\partial t} = \mathbf{J}. \tag{10.67}$$

10.6 The Excitation Tensor

In order to incorporate matter into Maxwell's equations we now define the 1-form H, the 2-form D and the 2-form G as

$$H = H_x \mathrm{d}x + H_y \mathrm{d}y + H_z \mathrm{d}z, \tag{10.68}$$

$$D = D_x \mathrm{d}y \wedge \mathrm{d}z + D_y \mathrm{d}z \wedge \mathrm{d}x + D_z \mathrm{d}x \wedge \mathrm{d}y, \tag{10.69}$$

$$G = D - H \wedge \mathrm{d}t, \tag{10.70}$$

where $\mathbf{D} = (D_x, D_y, D_z)$ is known as the *displacement field*, $\mathbf{H} = (H_x, H_y, H_z)$ is known as the *magnetising field* and G is known as the *excitation tensor*. If we assume flat spacetime with the Minkowski metric (again choosing $(\mathrm{d}t, \mathrm{d}x, \mathrm{d}y, \mathrm{d}z)$ to be a basis of 1-forms) we can write

$$G = \begin{pmatrix} 0 & \mathrm{H}_x & \mathrm{H}_y & \mathrm{H}_z \\ -\mathrm{H}_x & 0 & \mathrm{D}_z & -\mathrm{D}_y \\ -\mathrm{H}_y & -\mathrm{D}_z & 0 & \mathrm{D}_x \\ -\mathrm{H}_z & \mathrm{D}_y & -\mathrm{D}_x & 0 \end{pmatrix}. \tag{10.71}$$

In vacuum we set

$$\star F = G, \tag{10.72}$$

thereby introducing a linear map from $\star F$ to G. The map equates $H_\mu = B_\mu$ and $D_\mu = E_\mu$, which satisfies the vacuum constitutive relations, which we shall encounter in Chapter 11.

We then find that Equation (10.57) becomes

$$\star\, \mathrm{d}G = J. \tag{10.73}$$

By requiring Equation (10.73) to hold when matter is introduced we have derived the second pair of Maxwell's equations in matter.

The left hand side of (10.73) can be rewritten as

$$\begin{aligned} \mathrm{d}G &= \mathrm{d}D - \mathrm{d}\left(H \wedge \mathrm{d}t\right), \\ &= \mathrm{d}_S D + (\partial_t D - \mathrm{d}_S H) \wedge \mathrm{d}t, \qquad (10.74) \\ \star\mathrm{d}G &= \star\mathrm{d}_S D + \star\left[(\partial_t D - \mathrm{d}_S H) \wedge \mathrm{d}t\right] \\ &= \star\mathrm{d}_S D + \star\left[\partial_t D \wedge \mathrm{d}t\right] - \star\left[\mathrm{d}_S H \wedge \mathrm{d}t\right] \\ &= \partial_i D_i \mathrm{d}t - \partial_t D_i \mathrm{d}x^i + \star_S \mathrm{d}_S H \\ &= \left[\star_S \mathrm{d}_S D\right] \mathrm{d}t - \partial_t\left(\star_S D\right) + \star_S \mathrm{d}_S H. \qquad (10.75) \end{aligned}$$

Using the expansion calculated for the left hand side of Equation (10.73) to equate like terms the conventional form of the second pair of Maxwell's equations in matter can be

extracted:

$$\star_S \mathrm{d}_S D = \rho \quad \leftrightarrow \quad \nabla \cdot \mathbf{D} = \rho, \tag{10.76}$$

$$-\partial_t \left(\star_S D\right) + \star_S \mathrm{d}_S H = \mathbf{J} \quad \leftrightarrow \quad -\frac{\partial \mathbf{D}}{\partial t} + \nabla \times \mathbf{H} = \mathbf{J}. \tag{10.77}$$

This completes the use of the principle of least action to derive Maxwell's equations for vacuum and matter in covariant notation, where we have shown the results to be equal to the conventional presentation of Maxwell's equations.

Chapter 11

The Constitutive Equations

For transformation optics we would like to derive the necessary permittivity and permeability matrices to achieve a desired deformation of electromagnetic waves. In order to do so we need to understand the constitutive equations. Whereas in Chapter 3 we presented a simplified version of the constitutive equations, here we present the fully general linear case, taking magnetoelectric coupling into account. Nonlinear choices for the constitutive equations are possible [60], but not considered here.

The constitutive equations state that $\mathbf{D}$ and $\mathbf{H}$ are related to $\mathbf{E}$ and $\mathbf{B}$ through

$$\mathbf{D} = \varepsilon_0 \mathbf{E} + \mathbf{P} = \mathbf{E} + \mathbf{P}, \tag{11.1}$$

$$\mathbf{H} = \mu_0^{-1} \mathbf{B} - \mathbf{M} = \mathbf{B} - \mathbf{M}, \tag{11.2}$$

where ε_0 and μ_0 are the free-space permittivity and permeability, respectively and $\mathbf{P}$ and $\mathbf{M}$ are the *polarisation per unit volume* and *magnetisation per unit volume* vectors, respectively. As stated previously, we have chosen our units such that $\varepsilon_0 = \mu_0 = 1$ so that both terms can be omitted in Equations (11.1) and (11.2).

If we now assume that our medium is linear, that the polarisation is proportional to the electric field strength and that the magnetisation is proportional to the magnetic field

strength, then we can write for conventional non magnetoelectric media

$$\mathbf{P} = \underline{\eta_e}\mathbf{E}, \tag{11.3}$$

$$\mathbf{M} = \underline{\eta_h}\mathbf{H}, \tag{11.4}$$

where $\underline{\eta_e}$ and $\underline{\eta_h}$ are matrices, so that

$$\mathbf{D} = \left(\mathbb{I} + \underline{\eta_e}\right)\mathbf{E} = \underline{\varepsilon}\mathbf{E}, \tag{11.5}$$

$$\mathbf{H} = \left(\mathbb{I} + \underline{\eta_h}\right)^{-1}\mathbf{B} = \underline{\mu}^{-1}\mathbf{B}, \tag{11.6}$$

where $\underline{\eta_e}$ and $\underline{\eta_h}$ encode the polarisation $\mathbf{P}$ and the magnetisation $\mathbf{M}$, and $\mathbb{I}$ is the identity matrix. Finally, we include the possibility of magnetoelectric coupling, which leads to the generalised constitutive equations

$$\mathbf{D} = \underline{\varepsilon}\mathbf{E} + \underline{\gamma_h}\mathbf{H}, \tag{11.7}$$

$$\mathbf{B} = \underline{\mu}\mathbf{H} + \underline{\gamma_e}\mathbf{E}, \tag{11.8}$$

where $\underline{\gamma_h}$ and $\underline{\gamma_e}$ are the matrices allowing for magnetoelectric coupling. Equations (11.7) and (11.8) represent the most general linear constitutive equations.

Note that to derive Equations (11.7) and (11.8) we assumed no dispersion (i.e. an instantaneous medium response), a linear dependence, that the polarisation and magnetisation are proportional to the electric and magnetic field strengths respectively and we allowed for magnetoelectric coupling. There are many different assumptions that can be made about the medium, which have consequences for the constitutive equations. If we consider a nonconducting medium, then the main characteristics to consider are linearity, dissipation, isotropy, reciprocity, uniformity and dispersion [60]. In transformation optics we are normally interested in a map from Minkowski free-space, which is linear, non-dissipative, isotropic, reciprocal and non-dispersive. We will therefore ignore the effect of the more complicated cases.

The constitutive equations can be reformulated in covariant notation as the constitutive

map

$$\Gamma : \Lambda^2(M) \to \Lambda^2(M), \tag{11.9}$$

which maps the applied electromagnetic field F_{applied} to the net electromagnetic field in the medium F_{net}. In a similar vein to the discussion leading to Equations (11.5) and (11.6) we define

$$F_{\text{net}} = F_{\text{applied}} + \Pi, \tag{11.10}$$

where Π is the polarisation-magnetisation 2-form [65]. Assuming that Π depends linearly on F_{applied} we can write that $\Pi = \pi(F_{\text{applied}})$ and write

$$F_{\text{net}} = (\mathit{1} + \pi_{em}) F_{\text{applied}} = \Gamma(F_{\text{applied}}), \tag{11.11}$$

where *1*, π_{em} and Γ are linear maps. Γ can also be viewed as a mixed tensor, so that

$$(F_{\text{net}})_{\mu\nu} = \Gamma_{\mu\nu}{}^{\eta\gamma} (F_{\text{applied}})_{\eta\gamma}. \tag{11.12}$$

As in the vector case, we assume that there is a linear relation between G and F similar to Equation (10.72), which would give us the required information about the fields to solve Maxwell's equations. This linear relation can be expressed in covariant notation as a map $\mathcal{X}$, so that

$$\mathcal{X}(F) = G. \tag{11.13}$$

$\mathcal{X}$ is given by

$$G = \star\Gamma F, \tag{11.14}$$

so that

$$\mathcal{X} = \star \circ \Gamma : \Lambda^2(M) \to \Lambda^2(M) \tag{11.15}$$

is the constitutive equation in covariant notation. This definition is reasonable, as it implies that in order to take the medium into account we simply replace F in Equation (10.72) by the net force F_{net}.

We would like to understand the constitutive equation $\mathcal{X}$ better. In order to do this we

note that when $\mathcal{X}$ operates on F it sends a 2-form to another 2-form. We can derive the tensor χ from the map $\mathcal{X}$ by defining

$$G_{\mu\nu} = \chi_{\mu\nu}{}^{\eta\gamma} F_{\eta\gamma}. \tag{11.16}$$

As F and G are alternating 2-forms,

$$\chi_{\mu\nu}{}^{\eta\gamma} = -\chi_{\nu\mu}{}^{\eta\gamma} = \chi_{\nu\mu}{}^{\gamma\eta}. \tag{11.17}$$

Further, considerations of the alternating components of χ as well as the Lagrangian (see [60]), in conjunction with Equation (11.17), imply that

$$\gamma_h = \gamma_e^* = \gamma \tag{11.18}$$

in Equations (11.7) and (11.8), where the asterisk denotes the Hermitian conjugate. These conditions imply that χ can only have 20 independent elements.

We can identify the independent components of χ with a 6×6 matrix in Cartesian coordinates as follows:

$$\begin{array}{c} \chi_{\mu\nu}{}^{\eta\gamma} \\ \chi_{01}{}^{**} \\ \chi_{02}{}^{**} \\ \chi_{03}{}^{**} \\ \chi_{23}{}^{**} \\ \chi_{31}{}^{**} \\ \chi_{12}{}^{**} \end{array} \begin{array}{c} \begin{array}{cccccc} \chi_{**}{}^{01} & \chi_{**}{}^{02} & \chi_{**}{}^{03} & \chi_{**}{}^{23} & \chi_{**}{}^{31} & \chi_{**}{}^{12} \end{array} \\ \begin{pmatrix} -\alpha_{11} & -\alpha_{12} & -\alpha_{13} & \beta_{11} & \beta_{12} & \beta_{13} \\ -\alpha_{12}^* & -\alpha_{22} & -\alpha_{23} & \beta_{21} & \beta_{22} & \beta_{23} \\ -\alpha_{13}^* & -\alpha_{23}^* & -\alpha_{33} & \beta_{31} & \beta_{32} & \beta_{33} \\ \beta_{11}^* & \beta_{12}^* & \beta_{13}^* & \mu_{11}^{-1} & \mu_{12}^{-1} & \mu_{13}^{-1} \\ \beta_{21}^* & \beta_{22}^* & \beta_{23}^* & (\mu_{12}^{-1})^* & \mu_{22}^{-1} & \mu_{23}^{-1} \\ \beta_{31}^* & \beta_{32}^* & \beta_{33}^* & (\mu_{13}^{-1})^* & (\mu_{23}^{-1})^* & \mu_{33}^{-1} \end{pmatrix} \end{array}. \tag{11.19}$$

Going down the rows of Matrix (11.19) the covariant indices of χ are varied, while going along the columns the contravariant indices of χ are varied. The asterisk superscript represents the Hermitian of the matrix. Notice that the matrix can be divided into four

3×3 submatrices as

$$\begin{pmatrix} -\underline{\alpha} & \underline{\beta} \\ \underline{\beta}^* & \underline{\mu}^{-1} \end{pmatrix}. \tag{11.20}$$

We can now write the constitutive relation as a 6×6 matrix equation

$$\begin{pmatrix} \mathbf{D} \\ \mathbf{H} \end{pmatrix} = \begin{pmatrix} -\underline{\alpha} & \underline{\beta} \\ \underline{\beta}^* & \underline{\mu}^{-1} \end{pmatrix} \begin{pmatrix} -\mathbf{E} \\ \mathbf{B} \end{pmatrix}. \tag{11.21}$$

Notice that we have the matrix $\underline{\mu}$ in (11.20), but not $\underline{\varepsilon}$ or $\underline{\gamma}$. In order to find $\underline{\varepsilon}$ and $\underline{\gamma}$ in terms of $\underline{\alpha}$, $\underline{\mu}$ and $\underline{\beta}$ we rearrange Equation (11.21) and find that

$$\underline{\varepsilon} = \underline{\alpha} + \underline{\beta\mu\beta^*}, \tag{11.22}$$

$$\underline{\gamma} = \underline{\beta\mu}, \tag{11.23}$$

so that the constitutive equations are restored:

$$\mathbf{D} = \varepsilon\mathbf{E} + \gamma\mathbf{H}, \tag{11.24}$$

$$\mathbf{B} = \mu\mathbf{H} + \gamma^*\mathbf{E}. \tag{11.25}$$

(We consider only real $\underline{\varepsilon}$ and $\underline{\mu}$, so that the Hermitian conjugate in (11.19) on the coefficients of $\underline{\alpha}$ and $\underline{\mu}$ can be ignored.)

Using the constitutive relation we can write

$$\begin{aligned} G &= \chi F \\ &= \chi\left(\mathrm{d}A\right), \end{aligned} \tag{11.26}$$

so that from the second pair of Maxwell's equations we have

$$\star\, J = \mathrm{d}\chi\left(\mathrm{d}A\right). \tag{11.27}$$

Equation (11.27) represents 4 second order partial differential equations for A, which form

the covariant wave equation in matter.

In transformation optics we most commonly transform from vacuum Minkowski spacetime. It is useful to note that we then have from Equations (11.14) and (10.72) that

$$\begin{aligned} G &= \chi_0 F \\ &= \star\Gamma_0 F \\ &= \star F, \end{aligned} \tag{11.28}$$

so that $\chi_0 = \star$ and Γ_0 is the identity. By definition the Hodge dual for 2-forms in tensor notation is given by

$$\star_{\mu\nu}{}^{\alpha\beta} = \chi_{\mu\nu}{}^{\alpha\beta} = \frac{1}{2}\sqrt{|g|}\epsilon_{\mu\nu\eta\gamma}g^{\eta\alpha}g^{\gamma\beta}. \tag{11.29}$$

Chapter 12

Transformation Optics

In Chapters 10 and 11 we established how fields propagate in arbitrary media in a covariant way. We developed Maxwell's equations and examined the effect of the medium on the propagation of the fields. We would now like to use the accumulated knowledge in order to understand the reverse procedure. Rather than having a medium and trying to understand how the fields propagate through it, we are interested in beginning with a certain choice of fields and deriving what the medium must be in order for the chosen field configuration to exist. In essence, this is the aim of transformation optics.

Transformation optics is approached in its most general form by using transformations of manifolds. It is for this reason that we developed Maxwell's equations and the constitutive equation in covariant notation; forms can be pulled back using transformations and Maxwell's equations remain unaltered in their covariant form on a manifold. Physically, the manifold is vacuum spacetime and the transformations induce changes to the permittivity and permeability that can be mimicked using metamaterials.

12.1 Theory of Transformation Optics

Let us therefore begin our examination with an initial configuration of spacetime, given by the set

$$(M, g, F, G, \Gamma, J)\,. \tag{12.1}$$

This set represents a choice of Manifold M, a metric g, two 2-forms F and G, a map Γ and a 1-form J. We restrict our set by requiring the following equations to hold true:

$$\begin{aligned} \mathrm{d}F &= 0, && (12.2)\\ \mathrm{d}G &= J, && (12.3)\\ G &= \star\Gamma F. && (12.4) \end{aligned}$$

This ensures that on M Maxwell's equations and the constitutive equations hold.

We introduce a transformation

$$\tau : M \to \tilde{M} \subseteq M, \tag{12.5}$$

which maps our manifold to a subset of itself. We would like to use τ to map the remaining elements of the set to $\tilde{M}$, but as forms can only be pulled back, not pushed forward, we can only use τ to map forms from $\tilde{M}$ to M. To circumvent this problem we introduce the map

$$T : \tilde{M} \subseteq M \to M, \tag{12.6}$$

chosen so that

$$T \circ \tau = \mathrm{Id}|_M \tag{12.7}$$

is the identity map restricted to M. We can then define a new set

$$\left(\tilde{M}, \tilde{g}, \tilde{F}, \tilde{G}, \tilde{\Gamma}, \tilde{J}\right), \tag{12.8}$$

for which

$$\begin{aligned} \mathrm{d}\tilde{F} &= 0, && (12.9)\\ \mathrm{d}\tilde{G} &= \tilde{J}, && (12.10)\\ \tilde{G} &= \tilde{\star}\tilde{\Gamma}\tilde{F} && (12.11) \end{aligned}$$

must necessarily hold. Explicitly, we have that

$$\tau(M) = \tilde{M}, \tag{12.12}$$

$$T^*(g) = \tilde{g}, \tag{12.13}$$

$$T^*(F) = \tilde{F}, \tag{12.14}$$

$$T^*(G) = \tilde{G}, \tag{12.15}$$

$$T^*(J) = \tilde{J}, \tag{12.16}$$

where T^* is the *pull-back* and $\tilde{\star}$ is the Hodge dual as defined on $\tilde{M}$ using $\tilde{g}$. As Γ is not a form we can't pull it back.

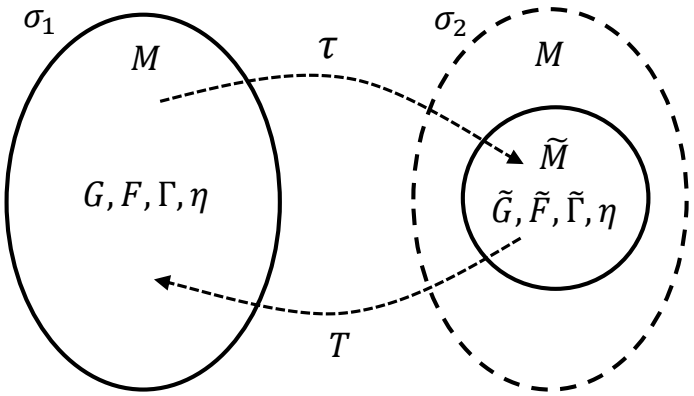

Figure 12.1: Manifolds and the maps between them used in transformation optics.

Let us use the theory presented above to construct transformation optics precisely. Consider Figure 12.1 where we begin with a Manifold M, which in our case is flat vacuum spacetime. Starting in curved space time [82] or from a non vacuum medium [83] has been considered elsewhere, but the majority of the work conducted in transformation optics assumes flat vacuum spacetime and for the work presented here we make the same assumption. Choose a smooth map τ from M into a subset of M and label this subset $\tilde{M}$. This map should be chosen so as to bend the electromagnetic waves in a desired way. The easiest way to choose τ is by considering its actions on geodesics in M. The construction we establish here will distort the light rays, which follow geodesics in M, so that they follow the perturbed paths in $\tilde{M}$ prescribed by the deformation τ. Exactly how this feat

is accomplished shall become clear momentarily.

Now find the smooth map which sends $\tilde{M}$ back to M and label it T, so that

$$T \circ \tau = \mathrm{Id}|_M. \tag{12.17}$$

It may be that the range of T cannot be all of M, as $\tilde{M}$ is not simply connected. In such a scenario it is acceptable to map from $\tilde{M}$ to M with a point (or many points) removed. The only necessity is that Equation (12.17) holds [65].

In transformation optics, M is (almost always, and certainly in our research) flat vacuum spacetime. We have the metric $g = \eta$, $J = 0$, the forms F and G and the map $\Gamma = \mathrm{Id}$. Our parameter space is therefore the set

$$\sigma_1 = (M, g = \eta, F, G, \Gamma = \mathrm{id}, J = 0) \tag{12.18}$$

where the equations

$$\mathrm{d}F = 0, \tag{12.19}$$

$$\mathrm{d}G = 0, \tag{12.20}$$

$$G = \star F, \tag{12.21}$$

hold.

We now apply the deformation τ, but *only* to M, F, G, J and Γ. The metric g and by extension the Hodge dual $\star$ are purposefully kept the same. We can do this, as $\tilde{M} \subseteq M$, so g (or a restricted version of g) will be a metric on $\tilde{M}$. Our new parameter space therefore becomes the set

$$\sigma_2 = \left(\tilde{M}, g = \eta, \tilde{F}, \tilde{G}, \tilde{\Gamma}, \tilde{J} = 0\right). \tag{12.22}$$

We leave the metric untouched in order to ensure a physical change in the fields. The metric measures distance, so keeping the original metric while transforming the fields

changes the distance between points. Light rays as defined by $\tilde{F}$ and $\tilde{G}$ on $\tilde{M} \subseteq M$ with the metric g will therefore no longer follow geodesics and no longer preserve Fermat's principle.

If we used the pullback of T to also transform the metric we would simply have a coordinate transformation with no physical change. The light rays would obey Fermat's principle and follow geodesics. This parameter set

$$\sigma_{\text{virtual}} = \left(\tilde{M}, \tilde{g}, \tilde{F}, \tilde{G}, \tilde{\Gamma}, \tilde{J}\right) \tag{12.23}$$

is known as the virtual space (see [84]).

On σ_2 we have

$$\begin{aligned}
\tilde{M} &= \tau(M), && (12.24)\\
\tilde{F} &= T^*(F), && (12.25)\\
\tilde{G} &= T^*(G), && (12.26)\\
\mathrm{d}\tilde{F} &= 0, && (12.27)\\
\mathrm{d}\tilde{G} &= 0, && (12.28)\\
\tilde{G} &= \star\tilde{\Gamma}\tilde{F}. && (12.29)
\end{aligned}$$

The crux of transformation optics now lies in finding what $\tilde{\Gamma}$ is in order to find $\tilde{\chi} = \star\tilde{\Gamma}$. We can then use Matrix (11.19) to identify the permeability and permittivity needed by the material in order to simulate the deformation of G and F induced by τ.

12.2 Calculating the Deformation of the Constitutive Equations

In order to find the permittivity and the permeability we want to calculate $\tilde{\Gamma}$, from which we can then derive $\tilde{\chi}$. We begin with an elegant calculation using differential forms. We

have that

$$\begin{aligned} \mathrm{d}\tilde{G} &= \mathrm{d}T^{*}G \\ &= \mathrm{d}T^{*} \star F \\ &= \mathrm{d}T^{*} \star (T^{*})^{-1}\,\tilde{F}, \end{aligned} \tag{12.30}$$

where we use the fact that $\Gamma = \mathrm{Id}$.

Hence,

$$\begin{aligned} \tilde{G} &= T^{*} \star (T^{*})^{-1}\,\tilde{F} \\ &= \star\star^{-1}\,T^{*} \star (T^{*})^{-1}\,\tilde{F}, \end{aligned} \tag{12.31}$$

so that

$$\tilde{\Gamma} = \star^{-1} T^{*} \star (T^{*})^{-1}\,. \tag{12.32}$$

We have thus demonstrated the core of transformation optics in a few simple steps. As far as the author is aware this concise, elegant proof has not been published in existing literature.

Whilst extremely elegant, the presentation above is of less utility for practical calculations. We therefore present a component based calculation following Thompson's work for completeness [65]. We have that

$$\begin{aligned} \tilde{G}_{\tau(x)} &= T^{*}\left(G_{x}\right) \\ &= T^{*}\left(\star_{x}\Gamma_{x}F_{x}\right) \\ &= T^{*}\left(\star_{x}F_{x}\right) \end{aligned} \tag{12.33}$$

as well as

$$\begin{aligned} \tilde{G}_{\tau(x)} &= \star_{\tau(x)}\tilde{\Gamma}_{\tau(x)}\tilde{F}_{\tau(x)} \\ &= \star_{\tau(x)}\tilde{\Gamma}_{\tau(x)}T^{*}\left(F_{x}\right) \end{aligned} \tag{12.34}$$

where the subscript stands for the point at which the element is being evaluated and we use the fact that in our case $\star = \tilde{\star}$.

In order to find $\tilde{\Gamma}$ we consider the action of $\tilde{G}$ as a 2-form on a bivector $\tilde{\mathbf{v}}_{\tau(x)} \in T^2_{\tau(x)}\left(\tilde{M}\right)$ to find that we can use Equation (12.33) to write

$$\begin{aligned} \tilde{G}_{\tau(x)}\left(\tilde{\mathbf{v}}_{\tau(x)}\right) &= T^*\left(\star_x F_x\right)\left(\tilde{\mathbf{v}}_{\tau(x)}\right) \\ &= \star_x F_x\left[\mathrm{d}T_{\tau(x)}\left(\tilde{\mathbf{v}}_{\tau(x)}\right)\right]. \end{aligned} \tag{12.35}$$

Here we use the fact that

$$T^* G\left(\tilde{\mathbf{v}}_{\tau(x)}\right) = G\left[\mathrm{d}T_{\tau(x)}\left(\tilde{\mathbf{v}}_{\tau(x)}\right)\right] \tag{12.36}$$

and that the *push-forward* of $\tilde{\mathbf{v}}_{\tau(x)}$ is defined at the point $\tau(x)$. We can now equate Equation (12.35) to Equation (12.34) to find that

$$\star_{\tau(x)} \tilde{\Gamma}_{\tau(x)} T^*\left(F_x\right)\left(\tilde{\mathbf{v}}_{\tau(x)}\right) = \star_x F_x\left[\mathrm{d}T_{\tau(x)}\left(\tilde{\mathbf{v}}_{\tau(x)}\right)\right]. \tag{12.37}$$

We can represent the pushforward $\mathrm{d}T_{\tau(x)}$ as the Jacobian matrix of T at x and denote it $\Lambda^{\mu}{}_{\nu}$. We can then rewrite Equation (12.37) as a tensor equation:

$$\star_{\alpha\beta}{}^{\gamma\delta}\Big|_{\tau(x)} \tilde{\Gamma}_{\gamma\delta}{}^{\mu\nu}\Big|_{\tau(x)} F_{\sigma\omega}|_x \Lambda^{\sigma}{}_{\eta}\Big|_{\tau(x)} \Lambda^{\omega}{}_{\xi}\Big|_{\tau(x)} V^{\alpha\zeta}\Big|_x = \star_{\pi\rho}{}^{\psi\kappa}\Big|_x F_{\sigma\omega}|_x \Lambda^{\pi}{}_{\alpha}|_{\tau(x)} \Lambda^{\rho}{}_{\zeta}\Big|_{\tau(x)} V^{\alpha\zeta}\Big|_x. \tag{12.38}$$

As V was chosen arbitrarily and the equation needs to hold for any F we find that

$$\star_{\alpha\beta}{}^{\gamma\delta}\Big|_{\tau(x)} \tilde{\Gamma}_{\gamma\delta}{}^{\mu\nu}\Big|_{\tau(x)} \Lambda^{\sigma}{}_{\eta}\Big|_{\tau(x)} \Lambda^{\omega}{}_{\xi}\Big|_{\tau(x)} = \Lambda^{\pi}{}_{\alpha}|_{\tau(x)} \Lambda^{\rho}{}_{\zeta}\Big|_{\tau(x)} \star_{\pi\rho}{}^{\psi\kappa}\Big|_x. \tag{12.39}$$

We isolate $\tilde{\Gamma}$ by multiplying by the inverse Jacobian matrix twice and by the Hodge dual, remembering that $\star^2 F = F$ for any 2-form F, to find that

$$\tilde{\Gamma}_{\gamma\delta}{}^{\mu\nu}\Big|_{\tau(x)} = -\star_{\gamma\delta}{}^{\lambda\kappa}\Big|_{\tau(x)} \Lambda^{\alpha}{}_{\lambda}|_{\tau(x)} \Lambda^{\beta}{}_{\kappa}\Big|_{\tau(x)} \star_{\alpha\beta}{}^{\psi\xi}\Big|_x \left(\Lambda^{-1}\right)^{\mu}{}_{\psi}\Big|_{\tau(x)} \left(\Lambda^{-1}\right)^{\nu}{}_{\xi}\Big|_{\tau(x)}. \tag{12.40}$$

Equation (12.40) encodes the essence of transformation optics. Given a transformation τ,

you find its inverse T and then use its Jacobian and the Hodge dual to calculate $\tilde{\Gamma}$. You then use

$$\tilde{\chi} \quad = \quad \star\tilde{\Gamma}, \tag{12.41}$$

to find the values of the permittivity $\underline{\varepsilon}$, the permeability $\underline{\mu}$ and the matrix $\underline{\gamma}$ for a particular choice of coordinates and attempt to build a structure which has these values. Most often this requires ingenuity, inventive trickery (see the reduced parameter approach in [33]) and perseverance.

Comparing Equations (12.32) and (12.40) we see that they are essentially the same. However the necessary information to actually calculate the permittivity and the permeability are more easily accessible in Equation (12.40).

Although the invariance of Maxwell's equations has been known since relativity theory was developed, transformation optics gives us a practical tool to make use of the invariance. Before transformation optics there were few analytic non plane-wave solutions to Maxwell's equations. Indeed, the author is only aware of the the Oseen transformation, presented in Section 3.4. The transformation theory presented in this chapter provides an effectively unlimited number of analytic solutions to Maxwell's equations. The trick lies in finding a diffeomorphism from flat vacuum spacetime that replicates a medium one is interested in. One should note that starting with a medium and hoping that a diffeomorphism from flat vacuum spacetime exists is unlikely to work, as for many media such a transformation will not exist.

Chapter 13

The Refractive Index of Reciprocal Electromagnetic Media

13.1 Introduction

After having established transformation optics rigorously from first principles the following chapter applies the prescription to an interesting problem. An analysis into the refractive index induced by a transformation is conducted in order to see what information is encoded in the refractive index and how the information can be used to better understand transformations or even develop new transformations not previously imagined. The motivation behind the work stems from a consideration of spatial transformation optics, which has been employed in a variety of contexts, most notably to propose [31, 32, 85] and then implement [33] an electromagnetic cloak, in which linear rays are distorted in such a way as to avoid a certain region of space, rather like water flowing around an obstruction in a river.

The electromagnetic medium arising from applying the transformation optics algorithm discussed in Chapter 12 is one in which the relative permittivity and permeability matrices are equal, i.e. $\underline{\underline{\varepsilon}} = \underline{\underline{\mu}}$. This is true because transformation optics mimics the deformation of vacuum, so in order for the transformed medium to respond to electric and magnetic

fields in the same proportion as for vacuum, inevitably we have that

$$\underline{\varepsilon} = \underline{\mu} \equiv \underline{\kappa}, \tag{13.1}$$

say. We refer to such a medium as being electromagnetically reciprocal or a '$\underline{\kappa}$' medium. The spatial deformation in general changes $\underline{\kappa}$ from $\underline{\kappa_0} = \mathrm{Id}$, its value in flat vacuum, to $\underline{\tilde{\kappa}}$, a matrix that is both inhomogeneous and anisotropic. In the ideal case $\underline{\tilde{\kappa}}$ will be real-valued, just like $\underline{\kappa_0}$ is real for vacuum, though a perfectly lossless medium can only be approximated in practice.

The required complexity can in principle be accessed through metamaterials technology, which precisely seeks to engineer the appropriate anisotropy and inhomogeneity via effective medium parameter values that are not found in nature. However, for most demonstrations of transformation optics to date some level of approximation has been invoked to bring the desired functionality within reach of current technology. A common approach is the reduced parameter scheme, in which the precise medium values are replaced with ones which at least yield the desired refractive index distribution. Rays are then refracted appropriately, although light is also scattered due to impedance changes. In the first demonstration of the electromagnetic cloak, for example, the reduced parameter scheme was used to eliminate the spatial dependence of one of the permeability components, and the geometry restricted to TE polarization [33].

Despite these compromises, the transformation medium defined by $\underline{\tilde{\kappa}}$ is of intrinsic interest since, from a technological viewpoint, the rapid advance of metamaterials technology brings 'perfect' transformation optics media closer to reality. More generally, a $\underline{\kappa}$-medium can mimic gravitational curvature without the need for the enormous mass densities required to actually distort space [86]. A curious feature of electromagnetic media described by the single matrix $\underline{\kappa}$ is that even if its principal values are all distinct, it is not birefringent [87].

Section 13.2 shows that media described by $\underline{\kappa}$ can be completely characterized by a refractive index function $n(\mathbf{r}, \hat{\mathbf{s}})$, which depends on position $\mathbf{r}$ and propagation direction $\hat{\mathbf{s}}$ (where the hat denotes a unit vector), but is independent of polarization. The index

is obtained from a simple ellipsoid construction, distinct from the usual constant energy index ellipsoid associated with birefringent media. Thereby a *geometrical optics* approach to spatial transformation optics is developed. To illustrate the approach, in Section 13.3 the index along the rays of the traditional electromagnetic cloak is calculated, and then, in Section 13.4, for a novel structurally chiral medium induced by a twist deformation. For the twisted medium it is integral lines of the Poynting vector that are modified by the deformation, the integral lines of the wave vector being unaffected.

Section 13.5 concludes by addressing the problem of impedance matching in spatial transformation optics. A simple example is used to demonstrate that although spatial dilations of vacuum can be successfully mimicked by the polarization-independent index $n(\mathbf{r}, \hat{\mathbf{s}})$, in general it is *not* possible to preserve the polarization independence of the impedance. This has intriguing implications for transformation optics, as impedance mismatch is usually connected to reflections, which would preclude perfect cloaking.

13.2 Calculating the Generalised Refractive Index

The calculation begins by developing the refractive index $n(\mathbf{r}, \hat{\mathbf{s}})$ as a function of $\underline{\kappa}$. Even though the previous discussion has been coordinate independent, when calculating $n(\mathbf{r}, \hat{\mathbf{s}})$ it is most convenient to use Cartesian coordinates. Consider a plane wave propagating in a medium characterized by $\underline{\kappa}$. The idea of a plane wave propagating through an inhomogeneous medium is an approximation that is useful when the wavelength is much greater than the scale of the inhomogeneity of $\underline{\kappa}$. Since any change in $\underline{\kappa}$ induced by a deformation is inevitably inhomogeneous (as $\underline{\kappa}$ consists of elements of χ, which transforms inhomogeneously) the results are only strictly valid in the geometric optics limit. However, solving for the local Eigenmodes in a geometrical optics approximation is valid for a sufficiently slowly varying inhomogeneity. Moreover plane waves provide a basis for more complicated field distributions.

Here Maxwell's equations are manipulated in order to derive the local refractive index seen by a local plane wave in a $\underline{\kappa}$-medium. The aim of the calculation is to project the fields

into the plane perpendicular to $\mathbf{k}$ and use the orthogonality relations thereby created to reduce the degrees of freedom of the problem and solve for the refractive index. Rotations are then used to find the refractive index for plane waves travelling in all directions.

We have that

$$\mathbf{E}(\mathbf{r},t) = \int \mathbf{E}(\mathbf{k},\omega)\exp\left[i\mathbf{k}\cdot\mathbf{r}-\omega t\right]\mathrm{d}^3k\mathrm{d}\omega, \tag{13.2}$$

$$\mathbf{H}(\mathbf{r},t) = \int \mathbf{H}(\mathbf{k},\omega)\exp\left[i\mathbf{k}\cdot\mathbf{r}-\omega t\right]\mathrm{d}^3k\mathrm{d}\omega. \tag{13.3}$$

Now take a local wave vector $\mathbf{k}$, and write Maxwell's equations in the frequency domain as

$$\mathbf{k}\times\mathbf{E}(\mathbf{k},\omega) = \omega\mu_0\underline{\kappa}\mathbf{H}(\mathbf{k},\omega), \tag{13.4}$$

$$\mathbf{k}\times\mathbf{H}(\mathbf{k},\omega) = -\omega\varepsilon_0\underline{\kappa}\mathbf{E}(\mathbf{k},\omega), \tag{13.5}$$

where ω is the frequency and μ_0 and ε_0 are included explicitly, as in most practical calculations they are not simply set to 1. For the remainder of the chapter the frequency dependency of $\mathbf{H}$ and $\mathbf{E}$ are omitted. The vectors in the coming analysis are illustrated in Figure 13.1.

Momentarily, let the propagation direction be set parallel to the z-axis i.e. $\mathbf{k} = k\hat{\mathbf{z}}$ and consider Equation (13.5). As

$$\mathbf{k}\times\mathbf{H} = -\omega\varepsilon_0\underline{\kappa}\mathbf{E} = -\omega\varepsilon_0\mathbf{D} \tag{13.6}$$

and $[\mathbf{k}\times\mathbf{H}]_z = 0$ when $\mathbf{k} = k\hat{\mathbf{z}}$, it is clear that $\mathbf{D}_z = 0$. As the transformation chosen is a diffeomorphism and therefore reversible, $\underline{\kappa}$ is invertible and therefore $\underline{\kappa}^{-1}\mathbf{D} = \mathbf{E}$.

Using $\mathbf{D}_z = 0$ by inspection

$$\left[\underline{\kappa}^{-1}\mathbf{D}\right]_\perp = \left(\underline{\kappa}^{-1}\right)_\perp \mathbf{D}_\perp. \tag{13.7}$$

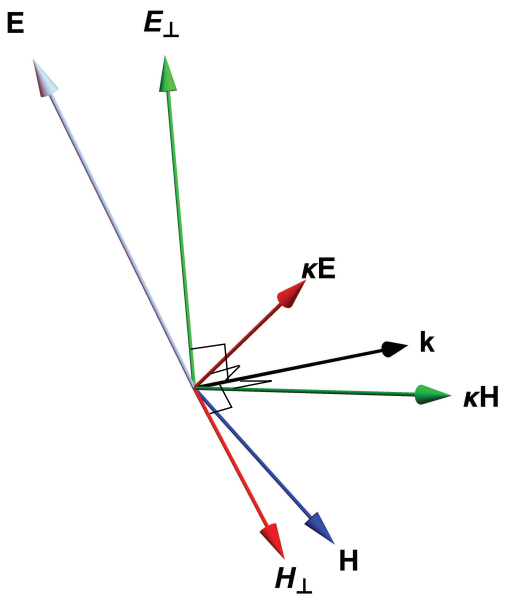

Figure 13.1: Disposition of vectors $\mathbf{k}$, $\mathbf{E}$, $\mathbf{E}_\perp$, $\mathbf{H}$, $\mathbf{H}_\perp$, $\underline{\kappa}\mathbf{E}$ and $\underline{\kappa}\mathbf{H}$. Note: (a) $\mathbf{k}$ is perpendicular to $\underline{\kappa}\mathbf{E}$, $\underline{\kappa}\mathbf{H}$, $\mathbf{E}_\perp$ and $\mathbf{H}_\perp$, (b) $\mathbf{E}_\perp$, $\underline{\kappa}\mathbf{H}$ and $\mathbf{k}$ form an orthogonal set, (c) $\mathbf{H}_\perp$, $\underline{\kappa}\mathbf{E}$ and $\mathbf{k}$ form an orthogonal set and (d) $\underline{\kappa}\mathbf{E}$, $\underline{\kappa}\mathbf{H}$, $\mathbf{E}_\perp$ and $\mathbf{H}_\perp$ are in the plane perpendicular to $\mathbf{k}$. Reproduced with permission from [4].

It therefore follows that

$$\begin{aligned}
& \mathbf{D} = \bar{\kappa}\mathbf{E} \\
\Longrightarrow \quad & \underline{\kappa}^{-1}\mathbf{D} = \mathbf{E} \\
\Longrightarrow \quad & \left[\underline{\kappa}^{-1}\mathbf{D}\right]_\perp = \mathbf{E}_\perp \\
\Longrightarrow \quad & \left(\underline{\kappa}^{-1}\right)_\perp \mathbf{D}_\perp = \mathbf{E}_\perp \\
\Longrightarrow \quad & \mathbf{D}_\perp = \left[\left(\underline{\kappa}^{-1}\right)_\perp\right]^{-1} \mathbf{E}_\perp. \qquad (13.8)
\end{aligned}$$

Equation (13.6) can be reduced to two dimensions in order to utilise Equation (13.8):

$$\begin{aligned}
\left[\mathbf{k} \times \mathbf{H}\right]_\perp &= k\mathbf{x}\mathbf{H}_\perp \\
&= -\omega\varepsilon_0 \mathbf{D}_\perp \\
&= -\omega\varepsilon_0 \left[\left(\underline{\kappa}^{-1}\right)_\perp\right]^{-1} \mathbf{E}_\perp, \qquad (13.9)
\end{aligned}$$

where $k \in \mathbb{R}$ is the z component of $\mathbf{k}$ defined previously and $\mathbf{x} = \begin{pmatrix} 0 & -1 \\ 1 & 0 \end{pmatrix}$.

In a simillar manner Equation (13.4) can be reduced to two dimensions and one arrives at the following pair of equations:

$$k\mathbf{x}\mathbf{E}_\perp = \omega\mu_0 \left[\left(\underline{\kappa}^{-1}\right)_\perp\right]^{-1} \mathbf{H}_\perp, \tag{13.10}$$

$$k\mathbf{x}\mathbf{H}_\perp = -\omega\varepsilon_0 \left[\left(\underline{\kappa}^{-1}\right)_\perp\right]^{-1} \mathbf{E}_\perp. \tag{13.11}$$

Equations (13.10) and (13.11) can be combined into an Eigen-equation in $\mathbf{E}_\perp$. One rewrites Equation (13.11) as

$$\mathbf{H}_\perp = -\omega k^{-1}\varepsilon_0 \mathbf{x}^{-1} \left[\left(\underline{\kappa}^{-1}\right)_\perp\right]^{-1} \mathbf{E}_\perp \tag{13.12}$$

and inserts the result into Equation (13.10) to find that

$$\begin{aligned} & k\mathbf{x}\mathbf{E}_\perp = \omega\mu_0 \left[\left(\underline{\kappa}^{-1}\right)_\perp\right]^{-1} \left\{-\omega k^{-1}\varepsilon_0 \mathbf{x}^{-1} \left[\left(\underline{\kappa}^{-1}\right)_\perp\right]^{-1} \mathbf{E}_\perp\right\} \\ \Longrightarrow \quad & \mathbf{E}_\perp = -\omega^2 k^{-2}\mu_0\varepsilon_0 \left\{\mathbf{x}^{-1} \left[\left(\underline{\kappa}^{-1}\right)_\perp\right]^{-1}\right\}^2 \mathbf{E}_\perp \\ \Longrightarrow \quad & \left[\left(\underline{\kappa}^{-1}\right)_\perp \mathbf{x}\right]^2 \mathbf{E}_\perp = -n^{-2}\mathbf{E}_\perp. \end{aligned} \tag{13.13}$$

In the calculation the fact that $\mathbf{x}^{-1} = -\mathbf{x}$ was used and n is defined as $n = k/\omega\sqrt{\epsilon_0\mu_0}$.

Equation (13.13) is an Eigenvector equation, which can now be solved for n. $\underline{\kappa}$ is symmetric, as it is Hermitian and we ignore absorption, which means it is real. We can therefore write

$$\begin{aligned} \left[\left(\underline{\kappa}^{-1}\right)_\perp \mathbf{x}\right]^2 &= \left[\begin{pmatrix} a & b \\ b & c \end{pmatrix} \begin{pmatrix} 0 & -1 \\ 1 & 0 \end{pmatrix}\right]^2 \\ &= \begin{pmatrix} b & -a \\ c & -b \end{pmatrix}^2 \\ &= \left(b^2 - ac\right) \begin{pmatrix} 1 & 0 \\ 0 & 1 \end{pmatrix} \\ &= -\det\left(\underline{\kappa}^{-1}\right)_\perp \mathbb{I}, \end{aligned} \tag{13.14}$$

where $\mathbb{I}$ is the 2×2 identity. We therefore have from Equation (13.13) that the refractive index n associated with the wave vector $\mathbf{k}$ is given by

$$n = \left[\det\left(\underline{\kappa}^{-1}\right)_{\perp}\right]^{-1/2}. \tag{13.15}$$

Although this key result has been calculated in Cartesian coordinates, it is valid in any orthonormal basis. It relates the refractive index for light propagating in a particular direction in a transformation medium to the deformation τ, as discussed in Chapter 12. Equation (13.15) is also valid for a complex $\underline{\kappa}$-medium, in which case the imaginary part of the permittivity and permeability correspond to absorption.

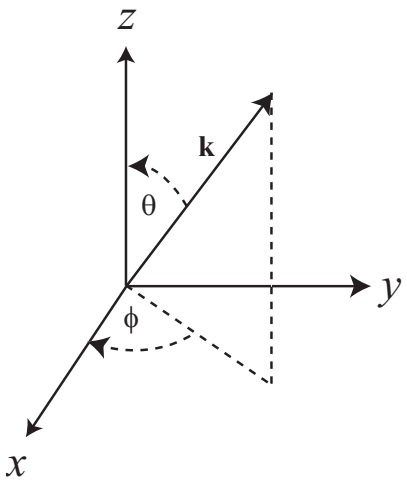

Figure 13.2: Rotation of $\mathbf{k}$ through angles ϕ and then θ to align it with the z-axis. Reproduced with permission from [4].

Remembering that for the presented calculations $\mathbf{k}$ was assumed to be aligned along the z-axis. Aligning $\mathbf{k}$ along the z-axis requires generally two rotations, ϕ followed by θ, say, (see Figure 13.2), so that

$$\underline{\kappa} = \underline{\mathcal{R}}_y(\theta)\,\underline{\mathcal{R}}_z(\phi)\,\underline{\kappa}_c\underline{\mathcal{R}}_z(-\phi)\,\underline{\mathcal{R}}_y(-\theta), \tag{13.16}$$

where $\underline{\kappa_c}$ denotes the pre-rotated representation of $\underline{\kappa}$ and

$$\underline{\mathcal{R}}_z(\phi) = \begin{pmatrix} \cos\phi & \sin\phi & 0 \\ -\sin\phi & \cos\phi & 0 \\ 0 & 0 & 1 \end{pmatrix}, \tag{13.17}$$

$$\underline{\mathcal{R}}_y(\theta) = \begin{pmatrix} \cos\theta & 0 & -\sin\theta \\ 0 & 1 & 0 \\ \sin\theta & 0 & \cos\theta \end{pmatrix}. \tag{13.18}$$

Since $\underline{\kappa_c}$ is symmetric it will be diagonal in an appropriately oriented Cartesian system. If we choose the local Cartesian axes to be along the principal axes of $\underline{\kappa_c} = \mathrm{diag}(\kappa_1, \kappa_2, \kappa_3)$, then setting $C_\theta = \cos\theta$ etc., $(\underline{\kappa}^{-1})_\perp$ is straightforwardly calculated to be

$$(\underline{\kappa}^{-1})_\perp = \begin{pmatrix} \kappa_1^{-1}C_\theta^2C_\phi^2 + \kappa_2^{-1}C_\theta^2S_\phi^2 + \kappa_3^{-1}S_\theta^2 & C_\theta S_\phi C_\phi\left(\kappa_2^{-1} - \kappa_1^{-1}\right) \\ C_\theta S_\phi C_\phi\left(\kappa_2^{-1} - \kappa_1^{-1}\right) & \kappa_1^{-1}S_\phi^2 + \kappa_2^{-1}C_\phi^2 \end{pmatrix}. \tag{13.19}$$

From Equation (13.15) it is then found that

$$n(\theta,\phi) = \left[\kappa_1^{-1}\kappa_2^{-1}C_\theta^2 + \kappa_3^{-1}S_\theta^2\left(\kappa_1^{-1}S_\phi^2 + \kappa_2^{-1}C_\phi^2\right)\right]^{-1/2}. \tag{13.20}$$

Setting $n_x = nS_\theta C_\phi, n_y = nS_\theta S_\phi, n_z = nC_\theta$ the above equation can be rewritten as:

$$\frac{n_x^2}{n_1^2} + \frac{n_y^2}{n_2^2} + \frac{n_z^2}{n_3^2} = 1, \tag{13.21}$$

where

$$n_1^2 = \kappa_2\kappa_3, n_2^2 = \kappa_3\kappa_1, n_3^2 = \kappa_1\kappa_2. \tag{13.22}$$

For the lossless case where all the principal values are real, Equation (13.21) becomes an ellipsoid, as illustrated in Figure 13.3. This ellipsoid represents the phase surface, and the refractive index, for *arbitrary* polarization, is equal to the radius vector to the surface of the ellipsoid.

Note that electromagnetically $n(\mathbf{r}, \hat{\mathbf{s}})$ *completely* describes the medium. Given the function

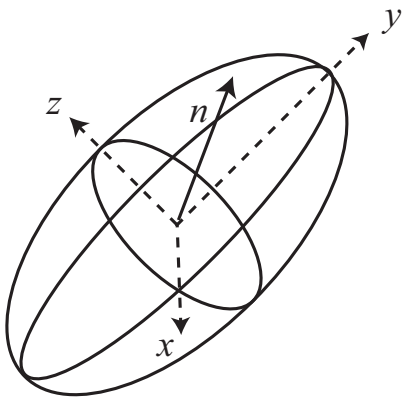

Figure 13.3: Index ellipsoid described by Equation (13.21). The lengths of the axes of the ellipse are $2n_1 = 2\left(\kappa_2\kappa_3\right)^{1/2}$, $2n_2 = 2\left(\kappa_3\kappa_1\right)^{1/2}$ and $2n_3 = 2\left(\kappa_1\kappa_2\right)^{1/2}$. The length of the radius vector extending from the origin to the surface of the ellipsoid represents the refractive index experienced by light travelling in that direction. Reproduced with permission from [4].

$n\left(\mathbf{r}, \hat{\mathbf{s}}\right) : M \times \mathcal{S}^2 \to \mathbb{R}$ where $\mathcal{S}^2$ is the unit 2-sphere the electromagnetic medium can be reconstructed by finding its three maximal radii (n_1, n_2, n_3), each of which occurs along a principal axis, and then calculating the principal constitutive parameters as

$$\kappa_1 = \frac{n_2 n_3}{n_1}, \ \kappa_2 = \frac{n_3 n_1}{n_2}, \ \kappa_3 = \frac{n_1 n_2}{n_3}. \tag{13.23}$$

An interesting question is whether the deformation τ can be reconstructed from a knowledge of the above local principal values $(\kappa_1(\mathbf{r}), \kappa_2(\mathbf{r}), \kappa_3(\mathbf{r}))$, together with the three parameters that specify the orientation at $\mathbf{r}$ of the local principal axes $(\Phi(\mathbf{r}), \Theta(\mathbf{r}), \Psi(\mathbf{r})$, say). Since $\underline{\kappa}$ is symmetric, the specification of $\underline{\kappa}$ results in six differential equations in terms of the six known quantities $[\kappa_1(\mathbf{r}), \kappa_2(\mathbf{r}), \kappa_3(\mathbf{r}), \Theta(\mathbf{r}), \Phi(\mathbf{r}), \Psi(\mathbf{r})]$. Solving these throughout M reconstructs a coordinate representation of τ up to some constant function on M. Hence, up to a constant, knowledge of the refractive index function $n\left(\mathbf{r}, \hat{\mathbf{s}}\right)$ is equivalent to knowledge of the deformation τ.

13.3 Generalised Refractive Index of the Cylindrical Cloak

Now that the refractive index has been developed as a function of the deformation of $\underline{\kappa}$ the theory can be applied to a well known transformation optics device such as an invisibility cloak. In this section the cylindrical cloak is analysed [33], which expands the origin to a

circle of radius a, compressing the disc of radius b into an annulus of inner radius a and outer radius b. In cylindrical polar coordinates the deformation τ is described via

$$\tilde{t} = t,\ \tilde{r} = \left(1 - \frac{a}{b}\right) r + a,\ \tilde{\theta} = \theta,\ \tilde{z} = z. \tag{13.24}$$

Transforming the Cartesian representation of $\underline{\kappa}$ (i.e. $\kappa^{ij} = \delta^{ij}$) to cylindrical polar coordinates one obtains $\underline{\kappa} = \mathrm{diag}(r, r^{-1}, r)$. We find the inverse transformation T and recall that in cylindrical coordinates the Minkowski metric is

$$\mathrm{d}s^2 = -\mathrm{d}t^2 + \mathrm{d}r^2 + r^2\mathrm{d}\theta^2 + \mathrm{d}z^2 \tag{13.25}$$

to calculate the Hodge dual and the Jacobian of T and find that

$$\tilde{\kappa}^{rr} = \tilde{r}\left(1 - \frac{a}{\tilde{r}}\right), \tag{13.26}$$

$$\tilde{\kappa}^{\theta\theta} = \tilde{r}^{-1}\left(1 - \frac{a}{\tilde{r}}\right)^{-1}, \tag{13.27}$$

$$\tilde{\kappa}^{zz} = \tilde{r}\left(1 - \frac{a}{\tilde{r}}\right)\left(1 - \frac{a}{b}\right)^{-2}. \tag{13.28}$$

We would like to translate our result to an *orthonormal basis* in order to ensure length preservation. In polar coordinates the orthonormal basis is $\{\partial_r, r^{-1}\partial_\theta, \partial_z\}$. We therefore find that

$$\tilde{\kappa}^{\hat{r}\hat{r}} = \left(1 - \frac{a}{r}\right) \equiv \kappa_r, \tag{13.29}$$

$$\tilde{\kappa}^{\hat{\theta}\hat{\theta}} = \left(1 - \frac{a}{r}\right)^{-1} \equiv \kappa_\theta, \tag{13.30}$$

$$\tilde{\kappa}^{\hat{z}\hat{z}} = \left(1 - \frac{a}{r}\right)\left(1 - \frac{a}{b}\right)^{-2} \equiv \kappa_z, \tag{13.31}$$

where, for notational simplicity, $\tilde{r}$ has been replaced by r. These principal values yield the

principal indices according to Equation (13.22) as

$$n_r = (\kappa_z \kappa_\theta)^{1/2} = \left(1 - \frac{a}{b}\right)^{-1}, \tag{13.32}$$

$$n_\theta = (\kappa_r \kappa_z)^{1/2} = \left(1 - \frac{a}{r}\right)\left(1 - \frac{a}{b}\right)^{-1}, \tag{13.33}$$

$$n_z = (\kappa_r \kappa_\theta)^{1/2} = 1. \tag{13.34}$$

The only refractive index component that varies in space inside the cloak is n_θ, which depends only on r. Choosing $a = 1$ and $b = 2$ and restricting to the $x - y$ plane, the index ellipses at different points inside the cloak are illustrated in Figure 13.4.

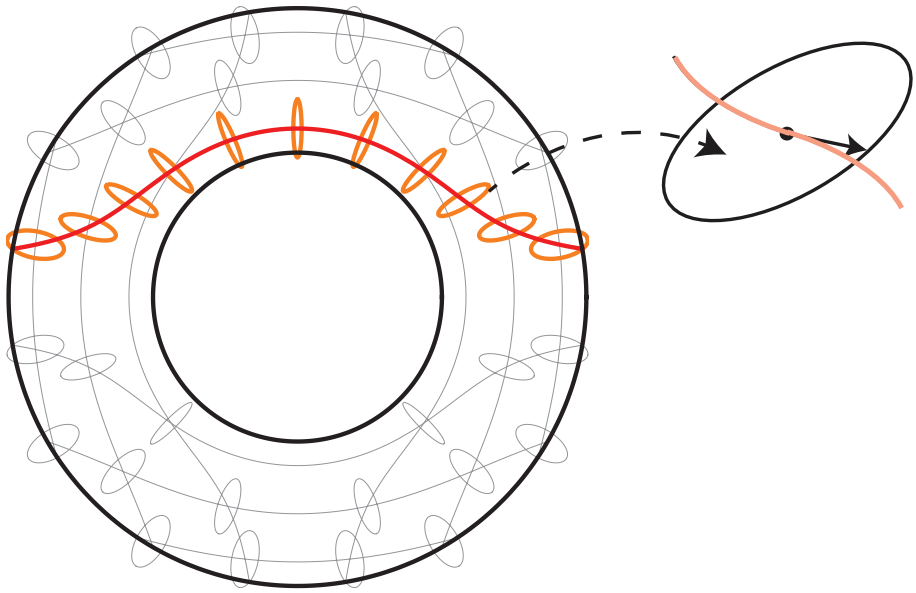

Figure 13.4: Refractive index ellipses and light rays for the cylindrical cloak. The inlay shows a close-up of the refractive index ellipse at a given point in the cloak, with the length of the arrow being equal to the refractive index at that point. Reproduced with permission from [4].

Each light ray is a geodesic that minimises the optical path length. However, it does not follow that the refractive index seen by the ray at a given point is the smallest possible at that point. This is clear when examining two separate light rays passing through the same point. Clearly they are not both experiencing the smallest refractive index value of the ellipse. Instead, each ray sees a single refractive index given by the radius to the ellipse in the direction of the ray as seen in the inlay in Figure 13.5.

The refractive index experienced along the highlighted ray of Figure 13.4 is shown in Figure 13.5. As expected, we find that the optical path length along the ray is equal to

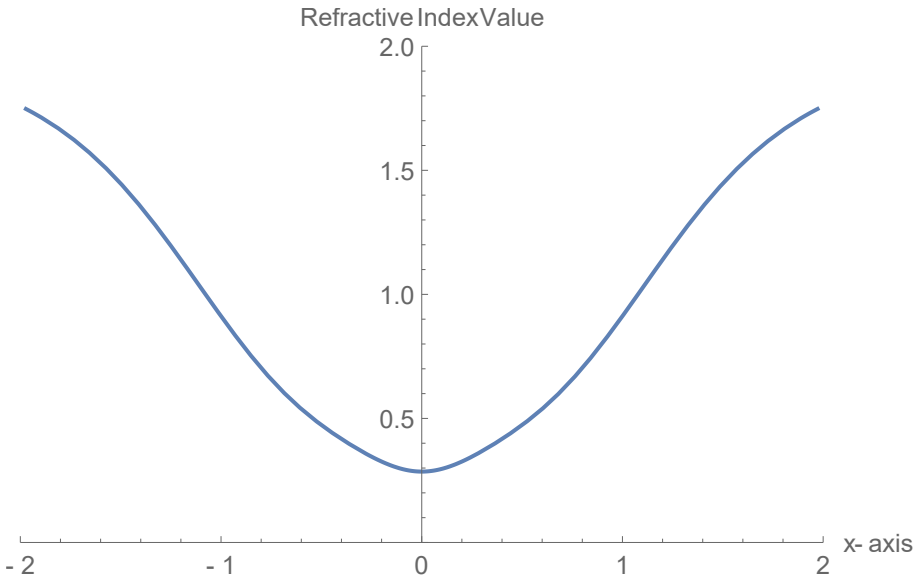

Figure 13.5: Refractive index value experienced by the highlighted light ray in Figure 13.4 as it travels through the cloak. Reproduced with permission from [4].

the undeformed (vacuum) path length:

$$\int_{x_1}^{x_2} n \mathrm{d}s = \int_{x_1}^{x_2} \mathrm{d}x \tag{13.35}$$

where $ds = (dx^2 + dy^2)^{1/2}$. The inclusion of isotropic absorption simply results in an exponential decay in the field intensity that is the same along any given geodesic.

13.4 Generalised Refractive Index of a Twisted Medium

In this section a structurally chiral medium is analysed, for which rays parallel to the z-axis starting at the plane $z = 0$ are twisted so that they form helices about the z-axis for $z > 0$. Consider the following transformation, expressed in Cartesian coordinates as:

$$\begin{pmatrix} \tilde{x} \\ \tilde{y} \\ \tilde{z} \end{pmatrix} = \underline{\mathcal{R}}_z(Kz) \begin{pmatrix} x \\ y \\ z \end{pmatrix} = \begin{pmatrix} \cos Kz & \sin Kz & 0 \\ -\sin Kz & \cos Kz & 0 \\ 0 & 0 & 1 \end{pmatrix} \begin{pmatrix} x \\ y \\ z \end{pmatrix}, \tag{13.36}$$

where K is a constant. Still in Cartesians, the $\underline{\kappa}$-medium can be calculated to be

$$\underline{\tilde{\kappa}} = \begin{pmatrix} 1+a^2 & ab & a \\ ab & 1+b^2 & b \\ a & b & 1 \end{pmatrix}, \tag{13.37}$$

where $a = -K(x\sin Kz - y\cos Kz)$ and $b = -K(x\cos Kz + y\sin Kz)$. The eigenvalues and corresponding eigen-indices are

$$\begin{aligned} &\kappa_1 = 1, \quad \kappa_2 = \beta + \left(\beta^2-1\right)^{1/2}, \qquad \kappa_3 = \beta - \left(\beta^2-1\right)^{1/2}, \\ &n_1 = 1, \quad n_2 = \left[\beta - \left(\beta^2-1\right)^{1/2}\right]^{1/2}, \quad n_3 = \left[\beta + \left(\beta^2-1\right)^{1/2}\right]^{1/2}, \end{aligned} \tag{13.38}$$

where $\beta = 1+K^2(x^2+y^2)/2$. Note that all indices throughout the medium are independent of z. However, the principal axes of the ellipsoid vary, both within the $x-y$ plane, and with z. The fact that $n_1n_2n_3 = 1$ indicates that the map of Equation (13.36) is volume preserving.

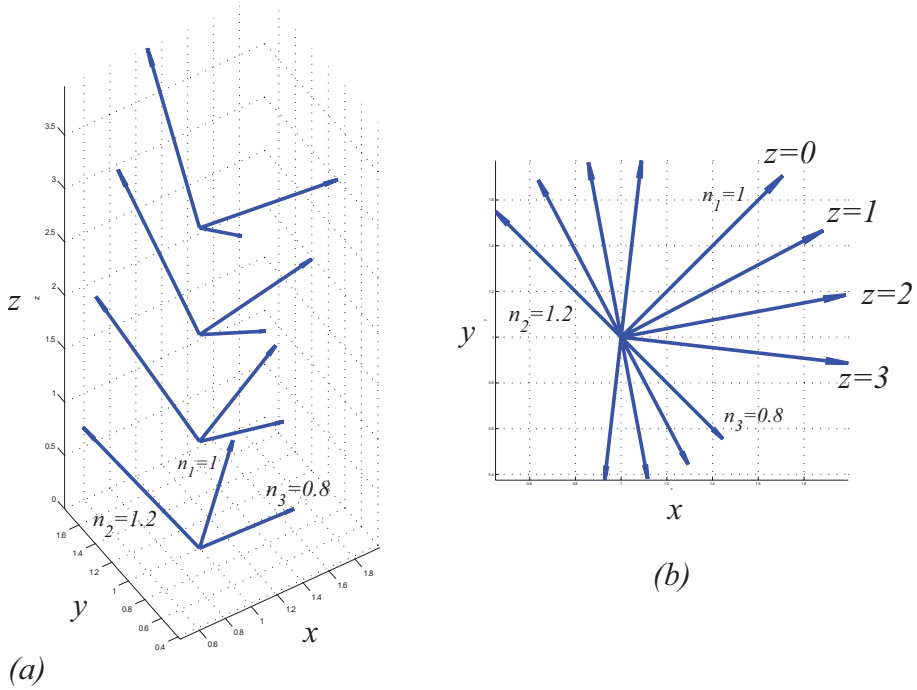

Figure 13.6: Evolution of the eigen-directions at $(x, y) = (1, 1)$ along z. To each eigen-direction an arrow is drawn proportional to the refractive index for propagation in that direction. Vectors associated with $n_1 = 1$ always lie in the $x-y$ plane. The right figure is a plan view looking down along $-z$. The eigen-directions associated with $n_{2,3}$ are foreshortened by projection ($K = 0.3$). Reproduced with permission from [4].

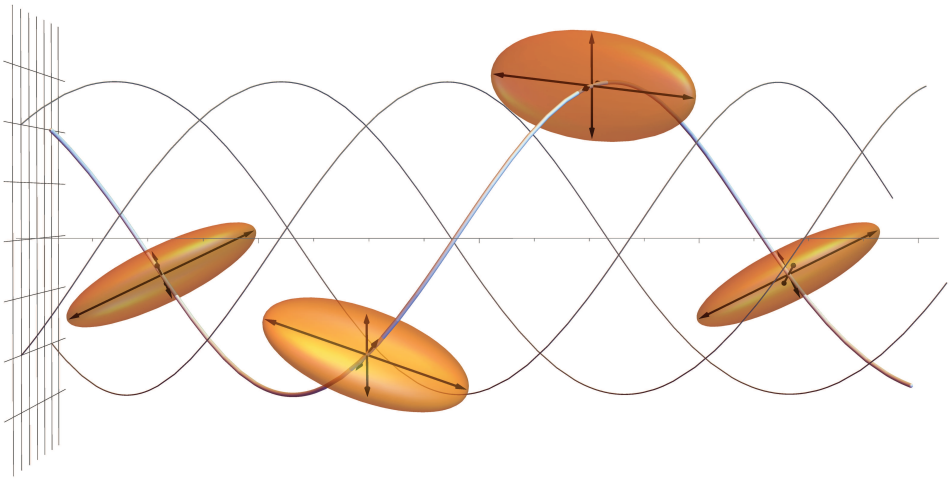

Figure 13.7: Integral lines of the Eigenvector associated with $n_2 = \left[\beta - \left(\beta^2 - 1\right)^{1/2}\right]^{1/2}$ (see Equation (13.38)). As shown in the text these lines are also the morphing of the lines (x_0, y_0, z) under Equation (13.36) and are, moreover, integral lines of the Poynting vector for a plane wave incident from the left along the axis. We superimpose the index ellipsoids at choice points on the integral lines. Reproduced with permission from [4].

Figure 13.6 shows the evolution of the eigen-directions of $\underline{\tilde{\kappa}}$ at $(x, y) = (1, 1)$ for $K = 0.3$. The principal directions associated with $\underline{\tilde{\kappa}}$ are calculated, and to each principal direction an arrow of length equal to the corresponding refractive index is plotted. The direction associated with the index $n_1 = 1$ is always radial in the x-y plane. The other two directions are associated with an index that is < 1 (respectively > 1), which points in the same (contra-) direction to the twist, though out of the x-y plane. Together the three directions are mutually orthogonal. The triad at other points the same distance from the axis can be adduced by rotation.

Figure 13.7 shows the evolution of light propagating along an Eigenvector. For this particular choice of light rays (rays travelling parallel to the z-axis for $z < 0$) the refractive index is the smallest of any of the possible refractive indeces available in the ellipsoid. The trajectories shown result from the local propagation direction in the plane $z = 0$ lying along the eigen-direction associated with $n = 0.8$. The resulting trajectories are helical and the figure shows the tumbling evolution of the index ellipsoid as it travels along one of these trajectories.

As well as the radial direction in the $x - y$ plane, there is another direction in which $n = 1$.

From Equation (13.37) we have that

$$\underline{\tilde{\kappa}}^{-1} = \begin{pmatrix} 1 & 0 & -a \\ 0 & 1 & -b \\ -a & -b & 1+a^2+b^2 \end{pmatrix}. \tag{13.39}$$

For propagation along the axis of the twist (i.e. along the z-axis) we see that

$$\underline{\tilde{\kappa}}_{\perp}^{-1} = \begin{pmatrix} 1 & 0 \\ 0 & 1 \end{pmatrix}, \tag{13.40}$$

from which $n = 1$ follows from Equation (13.15).

An axial monochromatic plane wave incident from vacuum to the medium occupying the half-space $z > 0$ has an electric and magnetic field for $z < 0$ given by

$$\mathbf{E} = \begin{pmatrix} E_{x0} \\ E_{y0} \\ 0 \end{pmatrix} e^{ik_0 z}, \ \mathbf{B} = c^{-1} \begin{pmatrix} -E_{y0} \\ E_{x0} \\ 0 \end{pmatrix} e^{ik_0 z}, \tag{13.41}$$

where $c = (\epsilon_0 \mu_0)^{-1/2}$ and the time dependence is implicit. To calculate the electric and magnetic fields for $z > 0$ we consider the deformation of the electromagnetic tensor:

$$\tilde{F}_{\mu\nu} = \frac{\partial x^\alpha}{\partial \tilde{x}^\mu} \frac{\partial x^\beta}{\partial \tilde{x}^\nu} F_{\alpha\beta}. \tag{13.42}$$

We find that

$$\frac{\partial x^\alpha}{\partial \tilde{x}^\mu} = \begin{pmatrix} 1 & 0 & 0 & 0 \\ 0 & \cos K\tilde{z} & -\sin K\tilde{z} & \tilde{d} \\ 0 & \sin K\tilde{z} & \cos K\tilde{z} & \tilde{f} \\ 0 & 0 & 0 & 1 \end{pmatrix}, \tag{13.43}$$

where $\tilde{d} = -K(\tilde{x}\sin K\tilde{z} + \tilde{y}\cos K\tilde{z})$ and $\tilde{f} = K(\tilde{x}\cos K\tilde{z} - \tilde{y}\sin K\tilde{z})$.

We can therefore calculate, using Equations (10.33), (13.42) and (13.43), that

$$\mathbf{E} = \begin{pmatrix} \cos K\tilde{z} & \sin K\tilde{z} & 0 \\ -\sin K\tilde{z} & \cos K\tilde{z} & 0 \\ \tilde{d} & \tilde{f} & 1 \end{pmatrix} \begin{pmatrix} E_{x0} \\ E_{y0} \\ 0 \end{pmatrix} e^{ik_0\tilde{z}}, \tag{13.44}$$

$$\mathbf{B} = c^{-1} \begin{pmatrix} \cos K\tilde{z} & \sin K\tilde{z} & 0 \\ -\sin K\tilde{z} & \cos K\tilde{z} & 0 \\ 0 & 0 & 1 \end{pmatrix} \begin{pmatrix} -E_{y0} \\ E_{x0} \\ 0 \end{pmatrix} e^{ik_0\tilde{z}}. \tag{13.45}$$

Similar argumentation can be used for finding $\mathbf{D}$ and $\mathbf{H}$, where we use Equation (10.71) and the inverse of Equation (13.43) along with the transformation rule

$$G^{\mu\nu} = \frac{\partial\tilde{x}^\mu}{\partial x^\alpha}\frac{\partial\tilde{x}^\nu}{\partial x^\beta}G^{\alpha\beta} \tag{13.46}$$

to find that

$$\mathbf{D} = \varepsilon_0 \begin{pmatrix} \cos K\tilde{z} & \sin K\tilde{z} & 0 \\ -\sin K\tilde{z} & \cos K\tilde{z} & 0 \\ 0 & 0 & 1 \end{pmatrix} \begin{pmatrix} E_{x0} \\ E_{y0} \\ 0 \end{pmatrix} e^{ik_0\tilde{z}}, \tag{13.47}$$

$$\mathbf{H} = (c\mu_0)^{-1} \begin{pmatrix} \cos K\tilde{z} & \sin K\tilde{z} & 0 \\ -\sin K\tilde{z} & \cos K\tilde{z} & 0 \\ \tilde{d} & \tilde{f} & 1 \end{pmatrix} \begin{pmatrix} -E_{y0} \\ E_{x0} \\ 0 \end{pmatrix} e^{ik_0\tilde{z}}. \tag{13.48}$$

The Poynting vector inside the medium, defined as $\mathbf{S} = \frac{1}{2}\mathrm{Re}\,(\mathbf{E}\times\mathbf{H}^*)$, is then calculated as

$$\mathbf{S}(z>0) = \frac{K}{2\mu_0 c}\begin{pmatrix} \tilde{y} \\ -\tilde{x} \\ 1 \end{pmatrix}|E|^2 = \frac{\partial_z}{2\mu_0 c}\begin{pmatrix} \cos Kz & \sin Kz & 0 \\ -\sin Kz & \cos Kz & 0 \\ 0 & 0 & 1 \end{pmatrix}\begin{pmatrix} x_0 \\ y_0 \\ z \end{pmatrix}. \tag{13.49}$$

In other words the Poynting vector is tangent to the helical curve resulting from the morphing of a straight line parallel to the z-axis. These are the helical curves shown in Figure 13.7.

It is important to emphasise the distinction between the medium discussed here and structurally chiral media discussed in Part I. The structurally chiral medium studied in the work presented in Part I have a dielectric tensor expressed as $\underline{\mathcal{R}}_z(Kz)\underline{\varepsilon}\underline{\mathcal{R}}_z(-Kz)$ where $\underline{\varepsilon}$ has distinct principal values. The progressive rotation of the principal axes of a birefringent medium produces a Bragg grating that for axial propagation reflects one circular polarization while transmitting the other. Plane waves, whether transmitted or reflected, follow linear paths.

However, for the case of the structurally chiral medium considered here, the pre-transformed medium is vacuum and there is no birefringence. Anisotropy is induced as a result of the helical transformation. The energy flow associated with axial propagation follows a *helical* path as shown in Figure 13.7, while the integral lines of the wave-vector are straight lines parallel to the z-axis. The medium described here is also distinct from the "field rotator" implemented by Chen et al. [88], and from an optically active medium.

Although difficult to manufacture, the medium discussed here would have interesting properties. Since the transformation transports the electromagnetic field, an image input to a slab of the proposed medium would emerge rotated, but with the polarization preserved. This is in contrast to standard methods of optically rotating an image (e.g. a dove prism [89]), which do not preserve polarization in general.

13.5 The Impossibility of Impedance Matching

The impedance is the ratio of the transverse components of the electric and magnetic fields. This section considers whether the constraint $\underline{\varepsilon} = \underline{\mu}$ implies that all plane waves propagating in the $\underline{\kappa}-$medium experience the same impedance as vacuum. A simple example is given, which shows that this is not the case.

Consider the trivial morphism that dilates one spatial direction:

$$(\tilde{x}, \tilde{y}, \tilde{z}) = (x, y, \lambda z). \tag{13.50}$$

The resulting constitutive tensor is then

$$\underline{\tilde{\kappa}} = \mathrm{diag}(\lambda^{-1}, \lambda^{-1}, \lambda). \tag{13.51}$$

Consider an off-axis ray or plane wave propagating in the above $\underline{\kappa}$-medium with $\mathbf{s} = (\sin\theta, 0, \cos\theta)$. Rotating so that the z-direction becomes the temporary propagation direction we have that

$$\tilde{\kappa} = \begin{pmatrix} C_\theta & 0 & S_\theta \\ 0 & 1 & 0 \\ -C_\theta & 0 & S_\theta \end{pmatrix} \begin{pmatrix} \lambda^{-1} & 0 & 0 \\ 0 & \lambda^{-1} & 0 \\ 0 & 0 & \lambda \end{pmatrix} \begin{pmatrix} C_\theta & 0 & -S_\theta \\ 0 & 1 & 0 \\ S_\theta & 0 & C_\theta \end{pmatrix}. \tag{13.52}$$

Hence the transverse medium properties are given by

$$\left(\tilde{\kappa}^{-1}\right)_\perp = \begin{pmatrix} C_\theta^2\lambda + S_\theta^2\lambda^{-1} & 0 \\ 0 & \lambda \end{pmatrix}, \tag{13.53}$$

and the index seen by the ray along θ (irrespective of polarization) is given by

$$n(\theta) = \left[\det\left(\tilde{\kappa}^{-1}\right)_\perp\right]^{-1/2} = \left(\lambda^2\cos^2\theta + \sin^2\theta\right)^{1/2}. \tag{13.54}$$

This index behaviour is largely unremarkable; along the direction of dilation ($\theta = 0$) it is just λ, and orthogonal to this direction ($\theta = \pi/2$) the vacuum value $n = 1$ is maintained.

However, despite the fact that $\underline{\varepsilon} = \underline{\mu}$, the impedance behaviour of the medium is in general polarization dependent. For a field propagating along the z-direction, the impedance is independent of polarization and equal to its vacuum value $\eta_0 = (\mu_0/\epsilon_0)^{1/2}$, but for a field propagating along the x-direction we have according to Equation (13.10) that

$$k_0 \begin{pmatrix} 0 & -1 \\ 1 & 0 \end{pmatrix} \begin{pmatrix} E_y \\ E_z \end{pmatrix} = \omega\mu_0 \begin{pmatrix} \lambda^{-1} & 0 \\ 0 & \lambda \end{pmatrix} \begin{pmatrix} H_y \\ H_z \end{pmatrix}, \tag{13.55}$$

which can be written as

$$\begin{pmatrix} E_y \\ E_z \end{pmatrix} = \eta_0 \begin{pmatrix} 0 & \lambda \\ -\lambda^{-1} & 0 \end{pmatrix} \begin{pmatrix} H_y \\ H_z \end{pmatrix}. \tag{13.56}$$

Therefore, if the electric field points along y the impedance is λ times its vacuum value, while if the field points along z, the impedance is λ^{-1} times its vacuum value.

It is worth noting that this polarization dependence of the impedance is intrinsic to any transformation optics design, and cannot be fixed by reduced parameter scaling or any other method. Since every transformation optics device is built out of similar spatial compressions/expansions that vary in degree at each point, no transformation device can preserve the impedance properties of vacuum.

Chapter 14

Research Conclusions

In Part II the theory of transformation optics was succinctly and rigorously set up. The theory was used to conduct a rigorous analysis of electromagnetically reciprocal media for which $\underline{\varepsilon} = \underline{\mu} \equiv \underline{\kappa}$. It was shown that the electromagnetics of a $\underline{\kappa}$-medium can be described in terms of a refractive index function $n(\mathbf{r}, \hat{\mathbf{s}})$, which can be represented by an ellipsoidal phase surface. A plane wave propagating in the $\hat{\mathbf{s}}$ direction sees just one refractive index, independent of polarization. If the $\underline{\kappa}$-medium is inhomogeneous, then the index at $\mathbf{r}$ is interpreted as that seen by a local plane wave under a geometrical optics approximation.

When applied to the original cylindrical cloak, the index along the morphed rays was calculated. The calculations allow an insight not only into the overall effect of the cloak, but also into exactly what happens inside the cloak through a highly intuitive, pictorial depiction, which could allow the internal physics of a transformation optics device to be examined for undesired effects or unforeseen problems. In the cylindrical cloak for instance it becomes immediately apparent that near the inner radius a the refractive index ellipse becomes infinitely thin in the θ direction, which suggest light must travel infinitely fast. Other effects that could be observed would be points of high intensity inside devices, which could lead to overheating or areas of rapid expansion or contraction of the refractive index ellipsoid, which could be difficult to manufacture.

A new kind of structurally chiral medium resulted when a $\underline{\kappa}$-medium was designed by morphing space with a progressive twist along the z-axis. It was found that the wave

vector of an axially incident plane wave to such a medium is undeviated, while the Poynting vector morphs exactly as prescribed by the deformation. By suggesting this medium and discussing its properties we demonstrate how simple it is to develop a new transformation and analyse its effects. Further work could go into analysing other deformations with an eye towards practical uses and ease of construction. Finally, we showed that whatever the deformation, preserving the impedance properties of vacuum is not generally possible, which raises doubts about the feasibility of perfect cloaking.

The hope is that the presented research will help researchers in transformation optics and metamaterials gain insight into transformation optics devices they have built or may be thinking of building. In the future, a refractive index ellipsoid analysis could form part of the repertoire with which a transformation optics device is analysed, optimised, and finally built.

Chapter 15

Further Study

The research touched on many aspects of transformation optics and transformation theory. In Part II the work leading up to and culminating in the refractive index ellipsoid was presented. As is to be expected, many other branches of research, both big and small, have presented themselves along the way and were studied to greater or lesser extent. This chapter presents some of the most interesting research areas that were touched upon, but not developed sufficiently for a publication or a self contained section within the thesis. These areas present excellent research opportunities, some of which will be pursued in the years to come.

One mystery that proved interesting early on during the research was the interplay between the metric induced covariant derivative ∇ and the constitutive tensor χ. A detailed understanding of how the elements in differential geometry interact is extremely beneficial while studying transformation optics, as they represent physical elements. One particular area of interest is the (torsion free) covariant derivative, which can be determined from the metric, and how it restricts the material properties determined by χ. Research into the interplay of these objects will aid in understanding how the distortion of lengths which occur in any transformation distort the permittivity and permeability.

Another area of particular interest was the link between geometric optics, transformation optics and Newtonian mechanics. Solving for the geodesics followed by light-rays by

minimising the action as discussed in the presented research can readily be compared to the minimisation problem that needs to be solved in order to determine the path followed by falling objects due to gravity. Analysing the similarities and differences between the two physical problems should prove interesting. Depending on what is discovered, any links drawn between the two may provide new insights into transformation optics that are well established in Newtonian mechanics or vice versa.

A research area on which some progress has been made considers the scalar wave equation and its applications to acoustics. We presented the covariant wave equation of matter in Equation (11.27), which is a very important equation in transformation optics, as it can potentially extend transformation optics methodology beyond electromagnetism.

Following unpublished research by Kinsler and McCall [90] we reformulate the scalar wave equation in a more conventional manner as

$$\nabla^2\psi - \frac{1}{v^2}\partial_t^2\psi = 0. \tag{15.1}$$

A deformation τ can be applied to the metric only, so that the wave equation becomes

$$\nabla_m \tau_i^m g^{ij} \tau_j^n \nabla_n \psi - \partial_t^2 \psi = 0. \tag{15.2}$$

If can be shown that for acoustics the longitudinal disturbance in the medium created by the deformation is given in Cartesian coordinates by

$$\frac{B}{\rho}\nabla_m \tau_i^m \delta^{ij} \tau_j^n \nabla_n \psi - \partial_t^2 \psi = 0, \tag{15.3}$$

where B is the bulk modulus and ρ is the density.

Equation (15.3) demonstrates how the covariant scalar wave equation may be adapted to acoustics. Further research can be conducted into this result in order to better understand the link between transformation optics and acoustics in the hope of aiding the development of transformation acoustics.

It should be possible to take the result even further by developing a covariant wave equation

for any given physical theory that can be expressed as a scalar wave equation. Obviously most of these theories are not covariant, so an analysis of the restrictions and limitations of the results could prove illuminating.

Finally the biggest and most interesting research project left is the development of further refractive indices for other physical theories. This goes in line with the development of a general theory of transformation media that can be applied to physical areas such as acoustics, thermodynamics, diffusion or Schrödinger's equations. The hope is that the research presented can be used to develop similar ellipsoids in other physical fields.

It should be noted that the final research interest may prove difficult, as there is certainly a unique position held by electromagnetism. transformation optics is exact because Maxwell's equations are naturally invariant under diffeomorphisms. They can be expressed as differential forms and therefore manipulated using differential geometry while remaining analytic. In order to apply a similar analysis to other physical theories they may need to be distorted or approximated. The hope is that approximations can be found that remain accurate enough to allow for interesting conclusions to be drawn.

Appendix A

Light Paths Inside a Structurally Chiral Medium

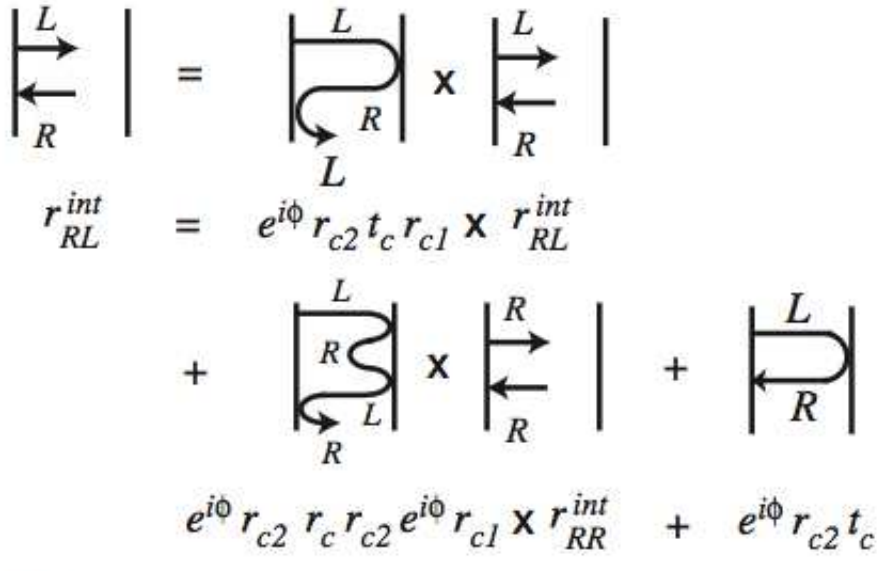

Figure A.1: Light ray equation for r_{RL}^{int}. Reproduced with permission from [2].

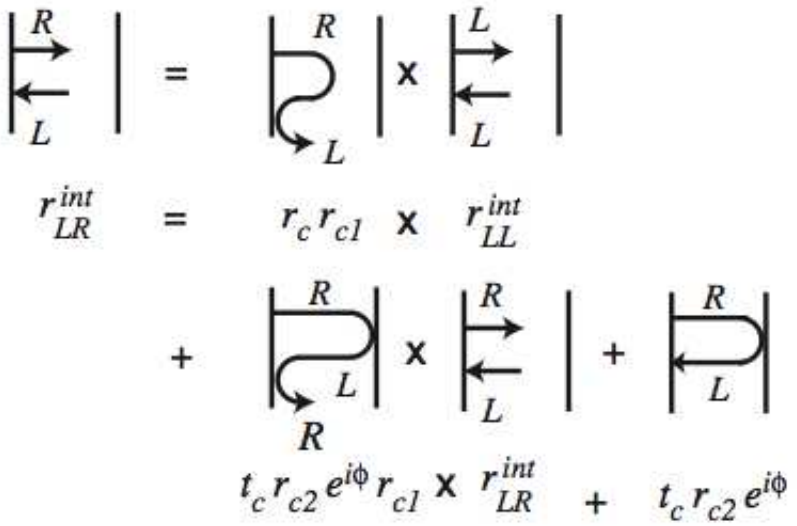

Figure A.2: Light ray equation for r_{LR}^{int}. Reproduced with permission from [2].

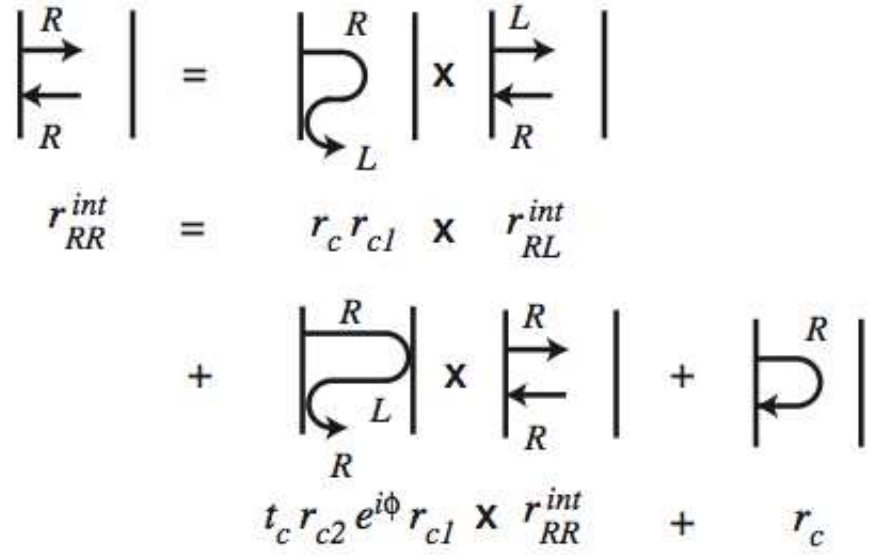

Figure A.3: Light ray equation for r_{RR}^{int}. Reproduced with permission from [2].

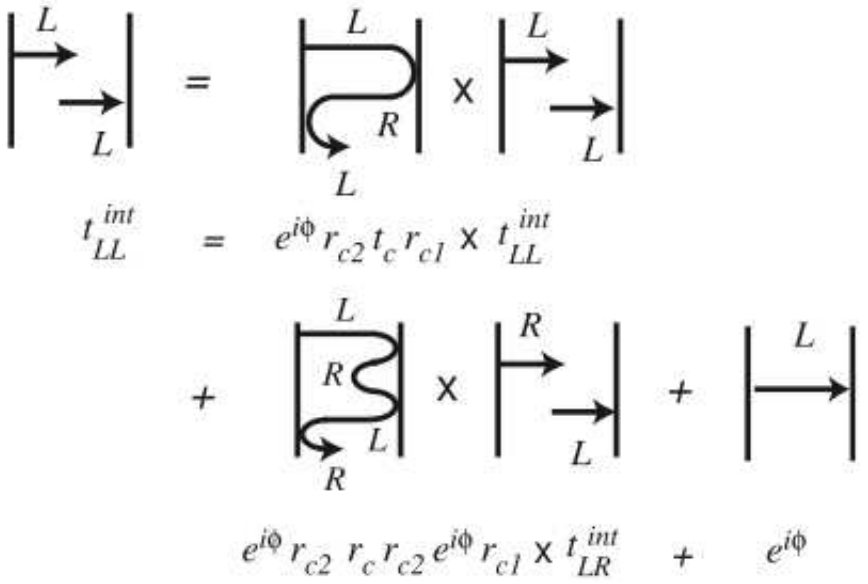

Figure A.4: Light ray equation for t_{LL}^{int}. Reproduced with permission from [2].

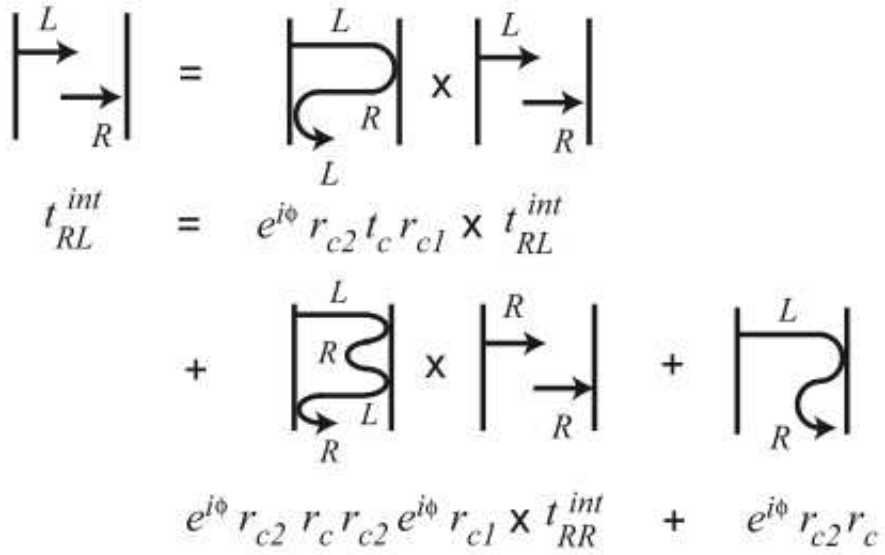

Figure A.5: Light ray equation for t_{RL}^{int}. Reproduced with permission from [2].

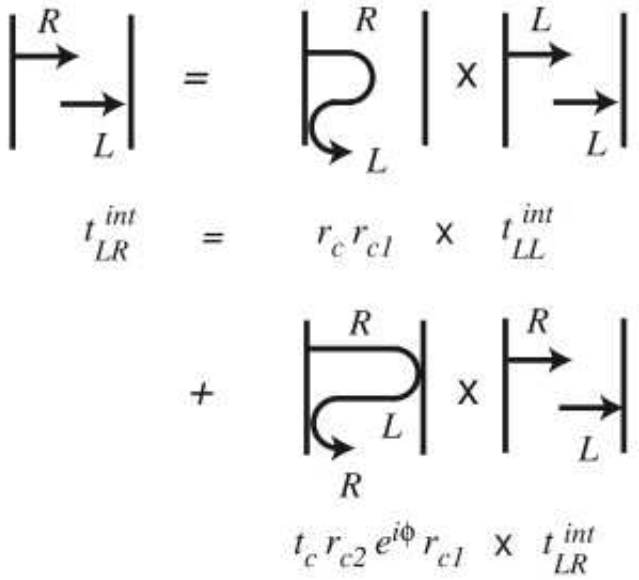

Figure A.6: Light ray equation for t_{LR}^{int}. Reproduced with permission from [2].

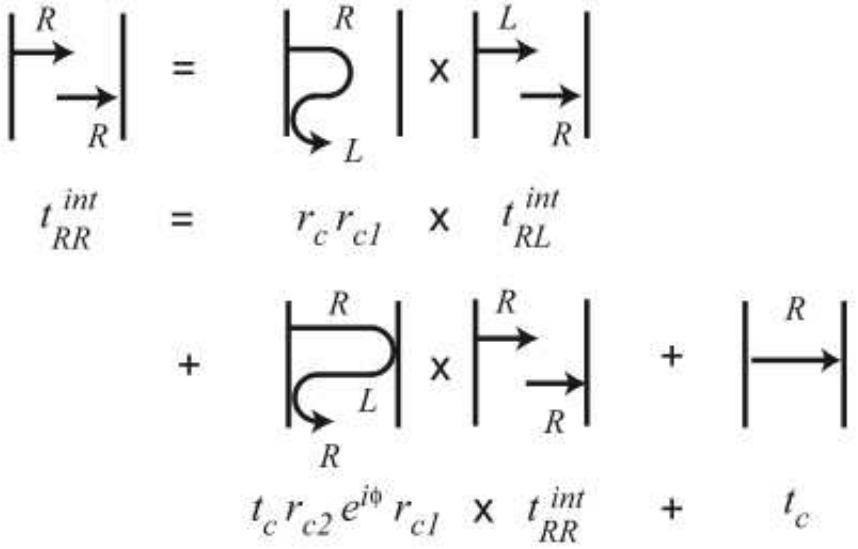

Figure A.7: Light ray equation for t_{RR}^{int}. Reproduced with permission from [2].

Appendix B

Key Concepts in Differential Geometry

In order to set up the theory behind transformation optics a thorough understanding of the mathematical tools used is needed. In this chapter these are introduced in a concise fashion, with the definitions often taken verbatim from Thompson's exposition in "Transformation Optics" [65], Tu's "An Introduction to Manifolds" [79] and Baez and Muniam's "Gauge Fields, Knots and Gravity" [63].

The chapter begins with an introduction to Exterior algebra in Section B.1, where preliminary concepts are defined. It continuous by defining smooth manifolds in Section B.2 and the tangent spaces on such smooth manifolds in Section B.3. It finally ends by defining differential forms and their operators is Section B.4, which includes the mathematical objects used in Part II and ends the excursion into theoretical mathematics. For further information on the topic the three sources mentioned above are suggested, as well as Sattinger and Helgason's works [91, 92].

B.1 Exterior Algebra

Definition B.1. The *dual space* V^* of a real vector space V is the vector space of all linear maps $f : V \to \mathbb{R}$. Its elements are called *covectors*.

Theorem B.1. *The functions* $\alpha^i : V \to \mathbb{R}$ *that send* $v = \sum v^i e_i \mapsto v^i$ *form a basis of* V^* *known as the* dual basis *of* V.

Definition B.2. A function $f : V^k = V \times ... \times V \to \mathbb{R}$ is *k-linear* if it is linear in each argument

$$f(..., av + bw, ...) = af(..., v...) + bf(..., w, ...) \tag{B.1}$$

and is known as a *k-tensor*.

Definition B.3. The vector space of all k-tensors on V is $L_k(V)$.

Definition B.4. Let f be a k-linear map and g be a l-linear map on a vector space V. Their *tensor product* is the $(k+l)$-linear map $f \otimes g$ given by

$$f \otimes g(v_1, ..., v_{k+l}) = f(v_1, ..., v_k) g(v_{k+1}, ..., v_{k+l}). \tag{B.2}$$

Definition B.5. An *alternating k-tensor* or *k-covector* is a k-linear function f such that for $\sigma \in S_k$

$$f\left(v_{\sigma(1)}, ..., v_{\sigma(k)}\right) = sgn(\sigma) f(v_1, ..., v_k) \tag{B.3}$$

and the *space of alternating k-linear functions* is $A_k(V)$.

Definition B.6. The *wedge product* or *exterior product* of two alternating multilinear functions f and g is the *alternating* multilinear function $f \wedge g$ given by

$$\begin{aligned} f \wedge g &= \frac{1}{k!l!} A(f \otimes g) \\ &= \frac{1}{k!l!} \sum_{\sigma \in S_{k+l}} sgn(\sigma) f\left(v_{\sigma(1)}, ..., v_{\sigma(k)}\right) g\left(v_{\sigma(k+1)}, ..., v_{\sigma(k+l)}\right). \end{aligned} \tag{B.4}$$

The wedge product therefore literally takes the tensor product, applies the alternating operator and rescales it appropriately.

Theorem B.2. *The wedge product is* anticommutative*:* $f \wedge g = (-1)^{kl} g \wedge f$*. The wedge product is* associative*:* $(f \wedge g) \wedge h = f \wedge (g \wedge h)$.

Theorem B.3. *The alternating k-linear functions* $\alpha^I = \alpha^{i_1} \wedge ... \wedge \alpha^{i_k}$, $i_1 < ... < i_k$ *form a basis of the* alternating space $A_k(V)$ *of dimension* $\begin{pmatrix} n \\ k \end{pmatrix}$.

B.2 Smooth Manifolds

We now define what a *smooth manifold* is, for which we need a number of preliminary definitions:

Definition B.7. A function $f : U \to \mathbb{R}$ is C^∞ at p if its partial derivatives

$$\frac{\partial^j f}{\partial x^{i_1} ... \partial x^{i_k}} \tag{B.5}$$

exist and are continuous at p for all $j \geq 0$. A function $f : U \to \mathbb{R}$ is C^∞ if it is C^∞ at $p \forall p \in U$.

Definition B.8. A *topology* on a set S is a collection $\mathcal{T}$ of subsets containing both the empty set and the set S such that $\mathcal{T}$ is closed under arbitrary unions and finite intersections. The elements of $\mathcal{T}$ are *open sets* ($A \subset S$ is *open in* S iff for every $p \in A$ there exists an open set V s.t. $p \in V \subset A$) and the pair $(S, \mathcal{T})$ is a *topological space*. A subcollection $\mathcal{B}$ of $\mathcal{T}$ is a *basis for the topology* $\mathcal{T}$ if given any U and $p \in U$, there is an open set $B \in \mathcal{B}$ such that $p \in B \subset U$.

Definition B.9. A topological space S is *second countable* if it has a countable basis. It is *Hausdorff* if given any two distinct points $x, y \in S$ there exist disjoint open set $U, V \subset S$ such that $x \in U$ and $y \in V$.

Definition B.10. A topological space M is *locally Euclidean of dimension* n if every point $p \in M$ has a neighbourhood U such that there is a homeomorphism ϕ from U onto an open subset in $\mathbb{R}^n$. The pair $(U, \phi : U \to \mathbb{R}^n)$ is a *chart* with U being the *coordinate neighbourhood* and ϕ being the *coordinate map*.

Definition B.11. A *topological manifold* is a Hausdorff, second countable, locally Euclidean topological space.

Definition B.12. Two charts (U, ϕ), (V, ψ) of a topological manifold are C^∞*-compatible* if the *transition functions*

$$\phi \circ \psi^{-1} : \psi(U \cap V) \to \phi(U \cap V), \ \psi \circ \phi^{-1} : \phi(U \cap V) \to \psi(U \cap V) \tag{B.6}$$

are C^∞.

Definition B.13. A C^∞ *atlas* on a locally Euclidean space M is a collection $\mathfrak{U} = \{(U_\alpha, \phi_\alpha)\}$ of pairwise C^∞-compatible charts that cover M. It is *maximal* if it is not contained in a larger atlas. A maximal atlas is also called a *differentiable structure* on M.

Definition B.14. A *smooth manifold* is a topological manifold M together with a maximal atlas.

We don't need to find a maximal atlas in order to ensure that a topological manifold M is a smooth manifold. The existence of *any* atlas on M will do.

Definition B.15. $C_p^\infty(M)$ is the set of all C^∞ functions from $p \in M$ to $\mathbb{R}$.

B.3 The Tangent Space

Definition B.16. A *point-derivation* of $C_p^\infty(M)$ is a linear map $D : C_p^\infty(M) \to \mathbb{R}$, such that $D(fg) = (Df)\, g(p) + f(p)\, Dg$. A *tangent vector* at a point $p \in M$ is a derivation at p. The tangent vectors at p form a vector space T_pM known as the *tangent space*.

Proposition B.1. *If $(U, x^1, ..., x^n)$ is a chart containing p, then the tangent space T_pM has basis*

$$\left\{ \left. \frac{\partial}{\partial x^i} \right|_p \right\} = \left\{ \partial_{x^i}|_p \right\}. \tag{B.7}$$

Definition B.17. Let $F : N \to M$, then at each $p \in N$ F induces a linear map of tangent spaces called its *differential at p,*

$$F_* : T_pN \to T_{F(p)}M \tag{B.8}$$

as follows. If $X_p \in T_pN$, then

$$(F_* (X_p)) f = X_p (f \circ F) \in \mathbb{R} \text{ for } f \in C^\infty_{F(p)} (M) . \tag{B.9}$$

The differential maps each function f that $F_* (X_p) \in T_{F(p)}M$ should act on from M to N by pulling f back onto N. It then acts on the pullback of f by X_p.

Applying the differential to $F : \mathbb{R}^n \to \mathbb{R}^m$ we find that $F_* = \left[\partial F^i / \partial x^j (p)\right]$, the Jacobian matrix of the derivative of F at p. Thus, the differential of a map between manifolds generalizes the derivative of a map between Euclidean spaces.

Corollary B.1. *If $F : N \to M$ is a diffeomorphism, then $F_* : T_pN \to T_{F(p)}M$ is an isomorphism of vector spaces ($T_pN \cong T_{F(p)}M$).*

B.3.1 The Tangent Bundle and Vector Fields

Definition B.18. The *tangent bundle* is the union of all the tangent spaces of M:

$$TM = \bigcup_{p \in M} T_pM. \tag{B.10}$$

Definition B.19. A *vector field* X on a manifold M is a function that assigns a tangent vector $X_p \in T_pM$ to each point $p \in M$.

Proposition B.2. *Given a local chart $(U, \{x^i\})$ the collection of vector fields*

$$\left\{ \frac{\partial}{\partial x^i} \right\} \tag{B.11}$$

is a basis of the tangent bundle TU.

Proposition B.3. *The tangent bundle is a smooth manifold.*

The electric field of a charge is a vector field. Definition B.19 suggests that we define a vector field as *smooth* if it is smooth as a map from M to TM.

Proposition B.4. *Let $(U, \phi) = \left(U, x^1, ..., x^n\right)$ be a chart on a manifold M. A vector field $X = \sum a^i \partial/\partial x^i$ on U is smooth iff the coefficient functions a^i are all smooth on U.*

A vector field X on M induces a linear map on the algebra $C^\infty(M)$ by sending $f \mapsto Xf$, where $Xf(p) = X_p f \in \mathbb{R}$. A vector field therefore acts as an operator on C^∞ functions.

Proposition B.5. *A vector field X on M is smooth iff for every smooth function f on M, the function Xf is smooth on M.*

We have now demonstrated that we can think of vector fields as operators on $C^\infty(M)$ functions (in fact, they are derivations on the algebra $C^\infty(M)$ of C^∞ functions).

Given a smooth map $F : N \to M$, we have previously defined its differential at $p \in N$ $F_* : T_pN \to T_{F(p)}M$. If $X_p \in T_pN$, then we defined $F_*(X_p) : C^\infty(M) \to C^\infty(M)$ by $F_*(X_p)\, g = X_p(g \circ F)$.

Definition B.20. We call $F_*(X_p)$ the *pushforward* of the vector X_p at p.

This notion does not extend to vector fields, as it is possible for F to map to distinct points $p, q \in N$ to the same point $z \in M$: $F(p) = F(q) = z$. However, it is possible that for a given vector field $X \in \mathfrak{X}(N)$, $F_*(X_p) \neq F_*(X_q)$. However, when F is a diffeomorphism, then it is surjective and $F(p) \neq F(q)$ if $p \neq q$, so the ambiguity does not arise. Further, since F is surjective F_*X is defined everywhere on M, so the pushforward of X will be unique.

B.4 Differential Forms and their Operators

We can now use the definition of manifolds, tangent spaces and vector fields to define the differential forms and their operators, which form the elements used in the calculations conducted in Part II.

Definition B.21. The *cotangent space to M at p, $T_p^*(M)$,* is the dual space of the tangent space.

Definition B.22. A *covector field* or a *(differential) 1-form* on an open subset $U \in M$ is a function ω that assigns a covector $\omega_p \in T_p^*(M)$ to each point $p \in U$:

$$\begin{aligned} \omega : U &\rightarrow \bigcup_{p \in U} T_p^*(\mathbb{R}^n) \\ p &\mapsto \omega_p \in T_p^*(\mathbb{R}^n). \end{aligned} \tag{B.12}$$

A covector field is the dual of a vector field, as it specifies a 1-form for every point $p \in U$, just like a vector field specifies a vector for each point $p \in U$.

Definition B.23. The *differential* of a function f is the 1-form df s.t.

$$(df)_p(X_p) = X_p f(p) \in \mathbb{R}. \tag{B.13}$$

Theorem B.4. $\left\{(dx^1)_p, ..., (dx^n)_p\right\}$ *is the basis of the cotangent space $T_p^*(M)$ dual to the basis $\{\partial/\partial x^1|_p, ..., \partial/\partial x^n|_p\}$ of the tangent space $T_p(M)$.*

Definition B.24. A *differential form ω of degree k* or a *differential k-form* on an open subset $U \in M$ is a function that assigns to each point $p \in U$ an alternating k-linear function $\omega_p \in A_k(T_p(M))$ on the tangent space $T_p(M)$. We can write

$$\omega = \sum a_I dx^I = \sum a_I dx^{i_1} \wedge ... \wedge dx^{i_k} \tag{B.14}$$

where $a_I : U \rightarrow \mathbb{R}$ and ω is C^∞ iff a_I are C^∞, as always. $\Omega^k(U)$ is the *vector space of C^∞ k-forms on U.*

Notice that a 0-form on U is a function on U, so $\Omega^0(U) = C^\infty(U)$.

Definition B.25. The *wedge product of two forms* $\wedge : \Omega^k(U) \times \Omega^l(U) \rightarrow \Omega^{k+l}(U)$ is

$$(\omega \wedge \tau)_p = \omega_p \wedge \tau_p \forall p \in U. \tag{B.15}$$

Definition B.26. The *exterior derivative* of a k-form $\omega = \sum a_I dx^I$ is

$$d\omega = \sum da_I \wedge dx^I = \sum_I \left(\sum_j \frac{\partial a_I}{dx^j} dx_j \right) \wedge dx^I \in \Omega^{k+l}(U). \tag{B.16}$$

Theorem B.5. *Exterior differentiation* $d{:}\Omega^*(U) \to \Omega^*(U)$ *is an* antiderivation of degree 1*:*

$$d(\omega \wedge \tau) = (d\omega) \wedge \tau + (-1)^{\deg \omega} \omega \wedge d\tau. \tag{B.17}$$

Further, $d^2 = 0$

and if $f \in C^\infty(U)$ *and* $X \in \mathfrak{X}(U)$*, then* $(df)X = Xf$*.*

Definition B.27. A k-form ω is *closed* if $d\omega = 0$. It is *exact* if there exists a (k-1)-form τ s.t. $\omega = d\tau$.

The exterior derivative is needed for integration on a manifold, as it defines the differentiation operator used in integration. No additional structure is needed to define the exterior derivative. It acts on differential forms and increases their order by 1.

Definition B.28. A *semi-Riemannian metric* on a vector space V is a map

$$g : V \times V \to \mathbb{R}, \tag{B.18}$$

that is *bilinear, symmetric* and *nondegenerate.*

Definition B.29. The *Minkowski metric* η, defined on a 4-dimensional vector space V, is given by

$$\eta(v, w) = -v_0 w_0 + v_1 w_1 + v_2 w_2 + v_3 w_3, \tag{B.19}$$

where $v, w \in V$.

Definition B.30. An *orthonormal basis* for a vector space V is a basis $\{e_1\}$ such that

$$g(e_i, e_j) = \delta_{ij} \tag{B.20}$$

where δ_{ij} is the Kronecker delta, which equal 1 when $i = j$ and 0 otherwise.

Definition B.31. The *inner product* of two 1-forms ω and μ $\langle \omega, \mu \rangle$ is given by

$$\langle \omega, \mu \rangle = g^{\alpha\beta} \omega_\alpha \mu_\beta, \tag{B.21}$$

where $g^{\alpha\beta}$ is the inverse of $g_{\alpha\beta} = g\left(e_\alpha, e_\beta\right)$.

The inner product of p-forms is bilinear, so it is enough to express the inner product of wedge products of 1-forms:

$$\left\langle e^1 \wedge ... \wedge e^p, f^1 \wedge ... \wedge f^p \right\rangle = \det \left[g\left(e^i, f^j\right) \right]. \tag{B.22}$$

Definition B.32. For an n-dimensional manifold M take a basis $\{\partial_\alpha\}$ and set $g_{\alpha\beta} = g\left(\partial_\alpha, \partial_\beta\right)$, define

$$\text{vol} = \sqrt{|\det g_{\alpha\beta}|} \mathrm{d}x^1 \wedge ... \wedge \mathrm{d}x^n. \tag{B.23}$$

The inner product and the volume form vol can now be used to define the Hodge star operator.

Definition B.33. The *Hodge star operator*

$$\star : \Omega^p\left(M\right) \to \Omega^{n-p}\left(M\right) \tag{B.24}$$

is the unique linear map from p-forms to $(n-p)$-forms such that for all $\omega, \mu \in \Omega^p\left(M\right)$,

$$\omega \wedge \star\mu = \langle \omega, \mu \rangle \, \text{vol}. \tag{B.25}$$

The Hodge star operator concludes the list of mathematical elements used in Part II. For further reading and more in-depth explanations the following references are suggested: [61–63, 65, 92].

Bibliography

[1] Martin W. McCall René D. M. Topf. Modes of structurally chiral lasers. *Physical Review A*, 90:053824, 2014.

[2] Martin McCall. Simplified theory of axial propagation through structurally chiral media. *Journal of Optics A*, 2009.

[3] C. V. Shank H. Kogelnik. Coupled wave theory of distributed feedback lasers. *Journal of Applied Physics*, 43:2327, 1972.

[4] René D. M. Topf Martin W. McCall, Paul Kinsler. The refractive index of reciprocal electromagnetic media. *Journal of Optics*, 2016.

[5] L. S. Goldberg and J. M. Schnur. Tunable internal-feedback liquid crystal-dye laser. *United States Patent*, 1973.

[6] N. V. Kukhtarev. Cholesteric liquid crystal laser with distributed feedback. *Sov. J. Quantum Electron.*, pages 774–776, June 1978.

[7] I. P. Ilchishin, E. A. Tikhonov, V. G. Tishchenko, and M. T. Shpak. Generation of a tunable radiation by impurity cholesteric liquid crystals. *JETP Lett.*, 32:24–27, 1980.

[8] Bara Fintel, Athena T. Samaras, and Edson Carias. The thalidomide tragedy: Lessons for drug safety and regulation. *HELIX*, 2009.

[9] J. P. Dowling, M. Scalora, M. J. Bloemer, and C. M. Bowden. The photonic band edge laser: a new approach to gain enhancement. *Journal of Applied Physics*, 75:1896–1899, 1994.

[10] Victor I. Kopp, B. Fan, H. K. M. Vithana, and Azriel Z. Genack. Low-threshold lasing at the edge of a photonic stop band in cholesteric liquid crystals. *Optics Letters*, 23:1707–1709, 1998.

[11] Andro Chanishvili, Guram Chilaya, Gia Petriashvili, Riccardo Barberi, Maria P. De Santo, Mario A. Matranga, and Federica Ciuchi. Lasing in an intermediate twisted phase between cholesteric and smectic a phase. *Applied Physics Letters*, 88:101105, 2006.

[12] Juergen Schmidtke, Werner Stille, Heino Finkelmann, and Sung Tae Kim. Laser emission in a dye doped cholesteric polymer network. *Advanced Materials*, 14:746–749, 2002.

[13] P. V. Shibaev, V. Kopp, A. Genack, and E. Hanelt. Lasing from chiral photonic band gap materials based on cholesteric glass. *Liquid Crystals*, 30:1391–1400, 2003.

[14] Andro Chanishvili, Guram Chilaya, Gia Petriashvili, Riccardo Barberi, Roberto Bartolino, Gabriella Cipparrone, Alfredo Mazzulla, Raquel Gimenez, Luis Oriol, and Milagros Pinol. Widely tunable ultraviolet-visible liquid crystal laser. *Applied Physics Letters*, 86:051107, 2005.

[15] Young-Chol Yang, Chul-Sik Kee, Jae-Eun Kim, Hae Yong Park, Jong-Cheon Lee, and Young-Jae Jeon. Photonic defect modes of cholesteric liquid crystals. *Physical Review E*, 60:6852–6854, 1999.

[16] Azriel Z. Genack Victor I. Kopp. Twist defect in chiral photonic structures. *Physical Review Letters*, 89:033901, 2002.

[17] Juergen Schmidtke, Werner Stille, and Heino Finkelmann. Defect mode emission of a dye doped cholesteric polymer network. *Physical Review Letters*, 90:083902, 2003.

[18] Stephen M. Morris, Philip J. W. Hands, Sonja Findeisen-Tandel, Robert H. Cole, Timothy D. Wilkinson, and Harry J. Coles. Polychromatic liquid crystal laser arrays towards display applications. *Optics Express*, 16:18827, 2008.

[19] Damian J. Gardiner, Stephen M. Morris, Philip J. W. Hands, Carrie Mowatt, Rupert Rutledge, Timothy D. Wilkinson, and Harry J. Coles. Paintable band-edge liquid crystal lasers. *Optics Express*, 19:2432, 2011.

[20] M. Humar and I. Musevic. 3d microlasers from self-assembled cholesteric liquid-crystal microdroplets. *Optics Express*, 18:26995, 2010.

[21] Karthik Peddireddy, V. S. R. Jampani, Shashi Thutupalli, Stephan Herminghaus, Christian Bahr, and Igor Musevic. Lasing and waveguiding in smectic a liquid crystal optical fibers. *Optics Express*, 21:30233, 2013.

[22] Iay E. Stockley, Gary D. Sharp, and Kristina M. Johnson. Fabry-perot etalon with polymer cholesteric liquid-crystal mirrors. *Optics Letters*, 24:55–57, 1999.

[23] M. H. Song et al. Defect mode lasing with lowered threshold in a three-layered hetero-cholesteric liquid-crystal structure. *Advanced Materials*, 18:193–197, 2006.

[24] S. Legoubin, M. Douay, P. Bernage, P. Niay, S. Boj, and E. Delevaque. Free spectral range variations of grating based fabry perot filters photowritten in optical fibers. *J. Opt. Soc. Am. A*, 12:1687–1694, 1995.

[25] Stephen Morris Harry Coles. Liquid-crystal lasers. *Nature Photonics*, 184:676–685, 2010.

[26] V. G. Veselago. The electrodynamics of substances with simultaneously negative values of ϵ and μ. *Soviet Physics Uspekhi*, 10:509–514, 1968.

[27] L. D. Landau and E. M. Lifshitz. *Electrodynamics of Continuous Media.* Pergamon Press, 1960.

[28] Sir John Pendry. Negative refraction makes a perfect lens. *Physical Review Letters*, 85:3967–3969, 2000.

[29] John Michael Williams. Some problems with negative refraction. *Physical Review Letters*, 87:249703, 2001.

[30] G. W. t Hooft. Comment on negative refraction makes a perfect lens. *Physical Review Letters*, 87:249701, 2001.

[31] U. Leonhardt. Optical conformal mapping. *Science*, 312:1777–1780, 2006.

[32] J. B. Pendry, D. Schurig, and D. R. Smith. Controlling electromagnetic fields. *Science*, 312:1780–1782, 2006.

[33] D. Shurig, J. J. Mock, B. J. Justice, S. A. Cummer, J. B. Pendry, A. F. Starr, and D. R. Smith. Metamaterial electromagnetic cloak at microwave frequencies. *Science*, 314:977–980, 2006.

[34] Jensen Li and J. B. Pendry. Hiding under the carpet: A new strategy for claoking. *Physical Review Letters*, 101:203901, 2008.

[35] r. Liu, C. Ji, J.J. Mock, J. Y. Chin, T. J. Cui, and D. R. Smith. Broadband groundplane cloak. *Science*, 323:366–369, 2009.

[36] L. H. Gabrielli, J. Cardenas, C. B. Poitras, and M. Lipson. Sillicon nanostructure cloak opearting at optical frequencies. *Nature Photonics*, 3:461–463, 2009.

[37] L. Zigoneanu, B. Popa, and S. A. Cummer. Three-dimensional broadband omnidirectional acoustic ground cloak. *Nature Materials*, 13:352–355, 2014.

[38] S. Brule, E. H. Javelaud, S. Enoch, and S. Guenneau. Experiments on seismit metamaterials: Molding surface waves. *Physical Review Letters*, 112:133901, 2014.

[39] Ulf Leonhardt and Tomas Tyc. Broadband invisibility by non-euclidian cloaking. *Science*, 323:110–112, 2009.

[40] Martin W McCall, Alberto Favaro, Paul Kinsler, and Allan Boardman. A spacetime cloak, or a history editor. *Journal of Optics*, 75:1134–40, 2010.

[41] M. Fridman, A. Farsi, Y. Okawachi, and A. L. Gaeta. Demonstration of temporal cloaking. *Nature*, 481:62–65, 2012.

[42] A. Greenleaf, Y. Kurylev, M. Lassas, and G. Uhlmann. Electromagnetic wormholes and virtual magnetic monopoles from metamaterials. *Physical Review Letters*, 99:183901, 2007.

[43] O. Quevedo-Teruel S. A. R. Horsley Y. Hao R. C. Mitchell-Thomas, T. M. McManus. Perfect surface wave cloaks. *Physical Review Letters*, 111:213901, 2013.

[44] Rene David Martin Topf. Chral lasers, möbius transformations and transformation media. Master's thesis, Imperial College London, 2013.

[45] M.W. McCall and A. Lakhtakia. Polarization-dependent narrowband spectral filtering by chiral sculptured thin films. *Journal of Modern Optics*, 47:743–755, 2000.

[46] M.W. McCall and A. Lakhtakia. Development and assessment of coupled wave theory of axial propagation in thin film helicoidal bi-anisotropic mediums. part 1: Reflectances and transmittances. *Journal of Modern Optics*, 47:963–991, 2000.

[47] M.W. McCall and A. Lakhtakia. Development and assessment of coupled wave theory of axial propagation in thin film helicoidal bi-anisotropic mediums. part 2: Dichroisms, ellipticity transformation and optical rotation. *Journal of Modern Optics*, 48:143–158, 2000.

[48] M.W. McCall. Axial electromagnetic wave propagation in inhomogeneous dielectrics. *Mathematical and Computer Modelling*, 34:1483–1497, 2001.

[49] M.W. McCall and A. Lakhtakia. Integrated optical polarization filtration via sculptured-thin-film technology. *Journal of Modern Optics*, 48:2179–2184, 2001.

[50] M.W. McCall and A. Lakhtakia. Coupling of a surface grating to a structurally chiral volume grating. *Electromagnetics*, 23:1–26, 2003.

[51] Akhlesh Lakhtakia Martin McCall. Explicit expressions for spectral remittances of axially excited chiral sculptured thin films. *Journal of Modern Optics*, 2004.

[52] M.W. McCall and A. Lakhtakia. Analysis of plane wave light normally incident to an axially excited structurally chrial half-space. *JMO*, 52:541–550, 2005.

[53] Martin McCall. Selected topics in plasmonics and metamaterials. 2012.

[54] A. Lakhtakia and M.W. McCall. Response of chiral sculptured thin films to dipolar sources. *AEU Int. J. Electron. Comm.*, 55:1–9, 2001.

[55] A. Lakhtakia and M.W. McCall. Simple expressions for bragg reflection from axially excited chiral sculptured thin films. *Journal of Modern Optics*, 49:Journal of Modern Optics, 2002.

[56] *Sculptured Thin Films - Nanoengineered Morphology and Optics*. Spie Press, 2005.

[57] A. Lakhtakia and M.W. McCall. Circular polarization filters. *Enyclopedia of Optical Engineering*, September 2003.

[58] Martin McCall Akhlesh Lakhtakia. Simple expressions for bragg reflection from axially excited chiral sculptured thin films. *Journal of Modern Optics*, 2002.

[59] Martin McCall. Special topics lecture notes. 2012.

[60] E. J. Post. *Formal Structure of Electromagnetic: General Covariance and Electromagnetics*. Dover Publications, 1997.

[61] Friedrich W. Hehl and Yuri N. Obukhov. *Foundations of Classical Electrodynamics*. Birkh$^{\acute{}}$auser, 2003.

[62] L. D. Landau and E. M. Lifschifz. *The Classical Theory of Fields*. Pergamon Press, 1975.

[63] John Baez and Javier P. Muniain. *Gauge Fields, Knots and Gravity*. World Scientific, 1994.

[64] Thomas A. Garrity. *Electricity and Magnetism for Mathematicians: A Guided Path from Maxwells Equations to Yang Mills*. Cambridge University Press, 2015.

[65] R. T. Thompson and S. A. Cummer. Transformation optics. *Advances in Imaging and Electron Physics*, 171, 2012.

[66] I. E. Carter, K. Weir, M. W. McCall, and A. R. Parker. Variation in the circularly polarised light reflection of lomaptera (scarabaeidae) beetles. *J. R. Soc. Interface*, 13, 20160115.

[67] http://www.chiralphotonics.com/Web/default.html. Chiral photonics webpage, March 2013.

[68] Eugene Hecht. *Optics*. Addison-Wesley, 2001.

[69] Martin McCall and Paul Stavrinou. Photonic structures. January 2013.

[70] C. W. Oseen. The theory of liquid crystals. *Transactions of the Faraday Society*, 1933.

[71] Amnon Yariv. *Quantum Electronics*. Wiley, 1989.

[72] Paul Kinsler and Martin W. McCall. The futures of transformations and metamaterials. *Photonics and Nanostructures*, 15:1–23, June 2015.

[73] Hakan Urey, Sven Holmstrom, and Utku Baran. Mems laser scanners: a review. *Journal of Microelectromechanical Systems*, 23:259–275, 2014.

[74] Stephen Morris. Informal discussions.

[75] Th. K. Mavrogordatos, S. M. Morris, F. Castles, P. J. W. Hands, A. D. Ford, H. J. Coles, and T. D. Wilkinson. Density of photon states in dye-doped chiral nematic liquid crystal cells in the presence of losses and gain. *Physical Review E*, 86:011705, 2012.

[76] S. M. Jeong et al. Defect mode lasing from a double-layered dye-doped polymeric cholesteric liquid crystal films with a thin rubbed defect layer. *Applied Physics Letters*, 90:261108, 2007.

[77] David Cardinal. Why movies like the hobbit are moving from 24 to 48 fps, December 2013.

[78] Stephen M. Morris, Philip J. W. Hands, Sonja Findeisen-Tandel, , Robert H. Cole, Timothy D. Wilkinson, and Harry J. Coles. Polychromatic liquid crystal laser arrays towards display applications. *Optics Express*, 2008.

[79] Loring W. Tu. *An Introduction to Manifolds*. Springer, 2010.

[80] Hendrik Lorenz. Electromagnetic phenomena in a system moving with any velocity smaller than that of light. *Proceedings of the Royal Netherlands Academy of Arts and Sciences*, 6:809–831, 1904.

[81] Albert Einstein. Zur elektrodynamik bewegter körper. *Annalen der Physik*, 17(891), 1905.

[82] R. T. Thompson. General relativistic contributions in transformation optics. *Journald of Optics*, 15(015102), 2012.

[83] R. T. Thompson. Trnasformation optics in nonvacuum initial dielectric media. *Physical Review A*, 82(053801), 2010.

[84] Thomas Philbin Ulf Leonhardt. *The Science of Invisibility*. Dover Publications Inc., 2010.

[85] U. Leonhardt and T. G. Philbin. General relativity in electrical engineering. *New Journal of Physics*, 8(247), 2006.

[86] Liu H Sheng C, Wang Y, Zhu S N, and Genov D A. Trapping light by mimicking gravitational lensing. *Nature Photonics*, 7:902–906, 2013.

[87] Alberto Favaro and Luzi Bergamin. The non birefringent limit of all linear, skewonless media and its unique lightcone structure. *Annalen der Physik*, 523:383–401, 2011.

[88] X. Chen, Y. Luo, J. Zhang, K. Jiang, J.B. Pendry, and S. Zhang. Macrocopic invisibility cloaking of visible light. *Nature Communications*, 2:176, 2011.

[89] Max Born and Emil Wolf. *Principles of Optics*. Cambridge University Press, 7th edition edition, 1999.

[90] M. W. McCall and P. Kinsler. Generalized scalar wave equation and "speed matrix". Research submitted for publication.

[91] O.L. Weaver D.H. Sattinger. *Lie Groups and algebras with Applications to Physics, Geometry, and Mechanics*. Springer Verlag, 1986.

[92] Sigmund Helgason. *Differential Geometry, Lie Groups, and Symmetric Spaces*. New York Academic Press, 1978.